

1-1-2011

Reconstruction Resolution Of Coherent Point Sources With Helmholtz Equation Least Squares

Richard Edward Dziklinski
Wayne State University

Follow this and additional works at: http://digitalcommons.wayne.edu/oa_dissertations

 Part of the [Acoustics, Dynamics, and Controls Commons](#)

Recommended Citation

Dziklinski, Richard Edward, "Reconstruction Resolution Of Coherent Point Sources With Helmholtz Equation Least Squares" (2011). *Wayne State University Dissertations*. Paper 211.

This Open Access Dissertation is brought to you for free and open access by DigitalCommons@WayneState. It has been accepted for inclusion in Wayne State University Dissertations by an authorized administrator of DigitalCommons@WayneState.

**RECONSTRUCTION RESOLUTION OF COHERENT POINT SOURCES WITH
HELMHOLTZ EQUATION LEAST SQUARES**

by

RICHARD E. DZIKLINSKI III

DISSERTATION

Submitted to the Graduate School

of Wayne State University,

Detroit, Michigan

in partial fulfillment of the requirements

for the degree of

DOCTOR OF PHILOSOPHY

2011

MAJOR: MECHANICAL ENGINEERING

Approved by:

Advisor

Date

© COPYRIGHT BY
RICHARD E. DZIKLINSKI III
2011
ALL RIGHTS RESERVED

DEDICATION

This dissertation is dedicated with great affection to my parents,

Tina and Richard Dziklinski Jr.

and to my siblings

for their unwavering love and support

ACKNOWLEDGMENTS

Every Ph.D. dissertation is the summation of many long hours of hard work and perseverance. However, if the student is lucky enough, the difficulty of a Ph.D. is significantly reduced by the people that are part of their lives. I deeply believe without my relationships with the following individuals, my ability to complete my Ph.D. studies would not have been feasible.

I have heard from numerous people that the success of a Ph.D student is dependent on the quality of the advisor, not only from an academic point of view, but also as a person. I first met my advisor, Dr. Sean Wu, in my undergraduate vibrations course at Wayne State University. From day one, his enthusiasm and care for his students was evident. As I progressed through my studies, his personal concern for how I balanced school and work always made going home and studying one more hour easier to do. Also, not being on campus most of the time would have made most advisor/student relationships difficult. However, Dr. Wu always found time before or after his normal working hours to make sure I received the help I need. I cannot imagine having an advisor better suited for me professionally or personally.

The other half of the work/school equation deals with my manager in my professional career, Joseph Starr. Similar to Dr. Wu, he shares the same traits of leadership and personal care for his workers. Through the years, he has helped guide me through the stress of work, school and personal life beyond the scope of a normal managerial role. Without his mentorship, most of this journey would not have been possible.

I leave the last words for the most important people in my life. My parents have been without a question the most loving and supportive individuals I know. They have sacrificed a lot over the years to ensure that my siblings and I lived happy and become successful. I have

always told people, that a Ph.D. is about perseverance over all else. I believe that this embodies the personalities of my parents. For every hour I've worked, I know they have worked longer and harder, while not having the same satisfaction of enjoying their job or studies that I do. For these reasons and for so many more, I thank them.

TABLE OF CONTENTS

DEDICATION	ii
ACKNOWLEDGMENTS	iii
LIST OF TABLES	vii
LIST OF FIGURES	viii
CHAPTER 1: INTRODUCTION	1
CHAPTER 2: LITERATURE REVIEW	5
Fourier Acoustics	5
Helmholtz Integral Equation	9
Helmholtz Equation Least Squares	11
Sub-Nyquist sampling theory	12
CHAPTER 3: THEORETICAL BACKGROUND	14
Planar Fourier Acoustics method	14
NAH resolution limits and spatial sampling theory	18
Helmholtz Equation Least Squares (HELs) method	20
Modified HELs	23
Regularization methods	24
CHAPTER 4: NUMERICAL SIMULATIONS	27
Mathematical model	29
Test setup	30
Simulation results	35
Validation of model and algorithms	36
Reconstruction accuracy when violating NAH resolution guidelines	42

Ghost source identification	66
Regularization justification	67
Modified HELS and the relationship of frequency and reconstructed source accuracy	69
Conclusions	75
CHAPTER 5: EXPERIMENTAL VALIDATIONS	77
Test setup	77
Experimental results.....	80
CHAPTER 6: CONCLUSIONS AND FUTURE WORK.....	89
REFERENCES	93
ABSTRACT	101
AUTOBIOGRAPHICAL STATEMENT.....	103

LIST OF TABLES

Table 2.1: Planar Fourier Acoustics coordinate system equations	7
Table 2.2: Cylindrical Fourier Acoustics coordinate system equations	7
Table 2.3: Spherical Fourier Acoustics coordinate system equations	8
Table 4.1: Simulation parameter ranges	35
Table 4.2: Spatial Nyquist sampling rate	35
Table 4.3: NAH spatial resolution guideline based on equation 3.10 only	35
Table 4.4: Frequencies of poor reconstruction for HELS, Modified HELS, Fourier Acoustics at 2.5 mm spacing for $\delta=10$ mm, $d=15$ mm, $\phi=\pi/2$ radians.	49
Table 5.1: Correlation of commanded and actual phase angle based on measurement.....	81

LIST OF FIGURES

Figure 2.1: Schematic of Planar Fourier Acoustics used on source with non-separable geometry	8
Figure 2.2: Schematic of conformal surface measurement possible with IBEM	11
Figure 3.1: Feasible source reconstruction locations with 6.35 mm microphones spaced at minimal measurement spacing	20
Figure 4.1: Real-world point-like source examples – a) hydraulic check valve common in hydraulic systems; b) refrigerator compressor relay; c) computer motherboard	29
Figure 4.2: Measurement and source planes	31
Figure 4.3: Theoretical plane characteristic dimension and reconstruction plane	32
Figure 4.4: Source locations reconstructed in simulation for $\delta=10$ mm. Reconstruction scenarios are indicated by the number in left hand corner. Source locations are indicated by black dots surrounded by white circles.	34
Figure 4.5: a) Measurement plane with 12.5 mm spacing, $\delta=15$ mm, $d=5$ mm, $\phi=\pi$ radians, $f=100\text{Hz}$; b) Fourier Acoustics reconstruction surface with 12.5 mm measurement spacing; c) Standard HELS reconstruction surface; d) Modified HELS reconstruction surface; e) Measurement surface plane with 2.5 mm spacing; f) Fourier Acoustics reconstruction surface with 2.5 mm measurement spacing; g) Measurement plane with 12.5 mm spacing, $\delta=15$ mm, $d=5$ mm, $\phi=\pi$ radians, $f=20\text{kHz}$; h) Fourier Acoustics reconstruction surface with 12.5 mm measurement spacing; i) Standard HELS reconstruction surface; j) Modified HELS reconstruction surface; e) Measurement surface plane with 2.5 mm spacing; k) Fourier Acoustics reconstruction surface with 2.5 mm measurement spacing	37
Figure 4.6: a) Measurement plane with 12.5 mm spacing, $\delta=15$ mm, $d=5$ mm, $\phi=\pi/2$ radians, $f=100\text{Hz}$; b) Standard HELS reconstruction surface; c) Modified HELS reconstruction surface; d) Measurement surface plane with 2.5 mm spacing; e) Fourier Acoustics reconstruction surface with 2.5 mm measurement spacing; f) Measurement plane with 15 mm spacing, $\delta=10$ mm, $d=5$ mm, $\phi=\pi/2$ radians, $f=20\text{kHz}$; g) Standard HELS reconstruction surface; h) Modified HELS reconstruction surface; i) Measurement surface plane with 2.5 mm spacing; j) Fourier Acoustics reconstruction surface with 2.5 mm measurement spacing	39
Figure 4.7: a) Measurement plane with 12.5 mm spacing, $\delta=15$ mm, $d=5$ mm, $\phi=0$ radians, $f=100\text{Hz}$; b) Standard HELS reconstruction surface; c) Modified HELS	

reconstruction surface; d) Measurement surface plane with 2.5 mm spacing; e) Fourier Acoustics reconstruction surface with 2.5 mm measurement spacing; f) Measurement plane with 12.5 mm spacing, $\delta=15$ mm, $d=5$ mm, $\phi=0$ radians, $f=20$ kHz; g) Standard HELS reconstruction surface; h) Modified HELS reconstruction surface; i) Measurement surface plane with 2.5 mm spacing; j) Fourier Acoustics reconstruction surface with 2.5 mm measurement spacing40

Figure 4.8: a) Measurement plane with 5 mm spacing, $\delta=15$ mm, $d=5$ mm, $\phi=\pi$ radians, $f=100$ Hz; b) Standard HELS reconstruction surface; c) Modified HELS reconstruction surface; d) Measurement plane with 5 mm spacing, $\delta=15$ mm, $d=5$ mm, $\phi=\pi/2$ radians, $f=100$ Hz; e) Standard HELS reconstruction surface; f) Modified HELS reconstruction surface; g) Measurement plane with 5 mm spacing, $\delta=15$ mm, $d=5$ mm, $\phi=\pi/2$ radians, $f=100$ Hz; h) Standard HELS reconstruction surface; i) Modified HELS reconstruction surface;.....41

Figure 4.9: Illustration of location error calculation 43

Figure 4.10: a) Measurement surface with 12.5 mm spacing, $\delta=10$ mm, $d=15$ mm, $\phi=\pi$ radians, $f=5$ kHz; b) Standard HELS reconstruction surface with 1.25 mm spacing; c) Modified HELS reconstruction surface with 1.25 mm spacing; d) Measurement surface with 2.5 mm spacing, $\delta=10$ mm, $d=15$ mm, $\phi=\pi$ radians, $f=5$ kHz; e) Fourier Acoustics reconstruction surface with 2.5 mm spacing; f) Fourier Acoustics reconstruction surface with 2.5 mm measurement spacing (inner 50% of surface)44

Figure 4.11: a) Measurement surface with 12.5 mm spacing, $\delta=10$ mm, $d=15$ mm, $\phi=\pi$ radians, $f=20$ kHz, $SNR=\infty$ dB; b) Measurement surface with 12.5 mm spacing, $\delta=10$ mm, $d=15$ mm, $\phi=\pi$ radians, $f=20$ kHz, $SNR=10$ dB; c) Angular spectrum at $SNR=\infty$ dB; d) Angular spectrum at $SNR=10$ dB46

Figure 4.12: Examples of reconstructions not producing two distinguishable sources with $\delta=10$ mm, $d=15$ mm, $\phi=\pi/2$ radians: a) Standard HELS, location 1 at 14 kHz; b) Modified HELS, location 2 at 17 kHz; c) Fourier Acoustics reconstruction at 2.5 mm spacing, location 2 at 13 kHz; d) Fourier Acoustics reconstruction at 2.5 mm spacing, location 2 at 13 kHz (zoomed-in);.....50

Figure 4.13: Reconstruction at 19 kHz with $\delta=10$ mm, $d=15$ mm, $\phi=0$ radians - a)12.5 mm spacing measurement surface b) Standard HELS; c) Modified HELS; d) 2.5 mm spacing measurement surface e) Fourier Acoustics at 2.5 mm spacing52

Figure 4.14: Determination of false sources – a) original measurement surface; b) original reconstructions surface with reconstructed sources near actual locations and an assumed false source at origin; c) shifted measurement surface; d)

reconstruction of shifted measurement surface illustrating source reconstruction was not consistent following measurement shift	53
Figure 4.15: Relative error analysis of LHS source for $\delta=15$ mm, $d=15$ mm, $\phi=\pi$ radians – a) location 1; b) location 2; c) location 3; d) location 4; e) location 5	54
Figure 4.16: Relative error analysis of RHS source for $\delta=15$ mm, $d=15$ mm, $\phi=\pi$ radians – a) location 1; b) location 2; c) location 3; d) location 4; e) location 5	55
Figure 4.17: Relative error analysis of LHS source for $\delta=15$ mm, $d=15$ mm, $\phi=\pi/2$ radians – a) location 1; b) location 2; c) location 3; d) location 4; e) location 5	56
Figure 4.18: Relative error analysis of RHS source for $\delta=15$ mm, $d=15$ mm, $\phi=\pi/2$ radians – a) location 1; b) location 2; c) location 3; d) location 4; e) location 5	57
Figure 4.19: Relative error analysis of LHS source for $\delta=15$ mm, $d=15$ mm, $\phi=0$ radians – a) location 1; b) location 2; c) location 3; d) location 4; e) location 5	58
Figure 4.20: Relative error analysis of RHS source for $\delta=15$ mm, $d=15$ mm, $\phi=0$ radians – a) location 1; b) location 2; c) location 3; d) location 4; e) location 5	59
Figure 4.21: Relative error analysis of LHS source for $\delta=10$ mm, $d=15$ mm, $\phi=\pi$ radians – a) location 1; b) location 2; c) location 3; d) location 4; e) location 5	60
Figure 4.22: Relative error analysis of RHS source for $\delta=10$ mm, $d=15$ mm, $\phi=\pi$ radians – a) location 1; b) location 2; c) location 3; d) location 4; e) location 5	61
Figure 4.23: Relative error analysis of LHS source for $\delta=10$ mm, $d=15$ mm, $\phi=\pi/2$ radians – a) location 1; b) location 2; c) location 3; d) location 4; e) location 5	62
Figure 4.24: Relative error analysis of LHS source for $\delta=10$ mm, $d=15$ mm, $\phi=\pi/2$ radians – a) location 1; b) location 2; c) location 3; d) location 4; e) location 5	63
Figure 4.25: Relative error analysis of LHS source for $\delta=5$ mm, $d=15$ mm, $\phi=\pi$ radians – a) location 1; b) location 2; c) location 3; d) location 4; e) location 5	64
Figure 4.26: Relative error analysis of LHS source for $\delta=5$ mm, $d=15$ mm, $\phi=\pi$ radians – a) location 1; b) location 2; c) location 3; d) location 4; e) location 5	65

Figure 4.27: Reconstruction from a shifted measurement location to identify ghost sources – a) original measurement surface; b) original reconstruction surface with ghost sources located in lower right hand corner; c) shifted measurement surface; d) shifted reconstruction surface with shifted ghost source with reduced amplitude. ...	67
Figure 4.28: Comparison of singular values at 100 Hz and 13 kHz. The 100 Hz case is characterized by a group of large and small singular values, whereas the 13 kHz case only has small singular values	68
Figure 4.29: a) Reconstruction of location scenario 4 at 13 kHz, $\delta=10\text{mm}$ and $\phi=\pi/2$ with TSVD; b) Reconstruction of location scenario 4 at 13 kHz, $\delta=10\text{mm}$ and $\phi=\pi/$ 2 with TR	68
Figure 4.30: a) Reconstruction of location scenario 4 at 12 kHz, $\delta=10\text{mm}$ and $\phi=\pi$ with β chosen via GCV; b) Reconstruction of location scenario 4 at 13 kHz, $\delta=10\text{mm}$ and $\phi=\pi$ β chosen manually	69
Figure 4.31: Wavefronts of two coherent sources on a line demonstrating the relationship between spherical spreading and interference at the measurement plane – a) $f=100$ Hz, $\phi=0$; b) $f=100$ Hz, $\phi=\pi/2$; c) $f=100$ Hz, $\phi=\pi$; d) $f=20$ kHz, $\phi=0$; e) $f=20$ kHz, $\phi=\pi/2$; f) $f=20$ kHz, $\phi=\pi$	71
Figure 4.32: Comparison of non-weighted and weighted wavefronts of two coherent sources on a line demonstrating the effects on interference at the measurement plane – a) $f=14$ kHz, $\phi=0$; b) $f=14$ kHz, $\phi=\pi/2$; c) $f=14$ kHz, $\phi=\pi$; d) $f=20$ kHz, $\phi=0$; e) $f=20$ kHz, $\phi=\pi/2$; f) $f=20$ kHz, $\phi=\pi$	73
Figure 4.33: Comparison of non-weighted and weighted wavefront magnitudes of two coherent sources on a line demonstrating the effects on interference at the measurement plane – a) $f=14$ kHz, $\phi=\pi/2$; b) $f=20$ kHz, $\phi=\pi/2$	74
Figure 5.1: a) Test setup; b) 12.5 mm spacing microphone array; c) point source approximated by orifices separated by approximately 10 mm	79
Figure 5.2: Experimental results of baseline test at $\delta=10$ mm, $d=15$ mm at source location scenario 3 (incoherent sources) – a) 15 kHz measurement surface; b) 16 kHz measurement surface c) reconstructed surfaces at 15 and 16 kHz overlaid	82
Figure 5.3: Measurement surfaces with $\delta=10$ mm, $d=15$ mm, $f=14$ kHz and varying phase angle at source location scenario 3 – a) reconstruction surface of incoherent sources (baseline); b) measurement surface with $\phi = 0$; c) measurement surface with $\phi = \pi/4$; d) measurement surface with $\phi = \pi/2$; e) measurement surface with $\phi = 3\pi/4$; f) measurement surface with $\phi = \pi$	83

Figure 5.4: Reconstruction surfaces with $\delta=10$ mm, $d=15$ mm, $f=14$ kHz and varying phase angle at source location scenario 3 – a) reconstruction surface of incoherent sources (baseline); b) Standard HELS reconstruction surface with $\phi = 0$; c) Standard HELS reconstruction surface with $\phi = \pi/4$; d) Standard HELS reconstruction surface with $\phi = \pi/2$; e) Standard HELS reconstruction surface with $\phi = 3\pi/4$; f) Standard HELS reconstruction surface with $\phi = \pi$ 84

Figure 5.5: Reconstruction surfaces with $\delta=10$ mm, $d=15$ mm, $f=14$ kHz and varying phase angle at source location scenario 3 – a) reconstruction surface of incoherent sources (baseline); b) Modified HELS reconstruction surface with $\phi = 0$; c) Modified HELS reconstruction surface with $\phi = \pi/4$; d) Modified HELS reconstruction surface with $\phi = \pi/2$; e) Modified HELS reconstruction surface with $\phi = 3\pi/4$; f) Modified HELS reconstruction surface with $\phi = \pi$ 85

Figure 5.6: Measurement surfaces with $\delta=10$ mm, $d=15$ mm, $f=15$ kHz and varying phase angle at source location scenario 3 – a) reconstruction surface of incoherent sources (baseline); b) measurement surface with $\phi = 0$; c) measurement surface with $\phi = \pi/4$; d) measurement surface with $\phi = \pi/2$; e) measurement surface with $\phi = 3\pi/4$; f) measurement surface with $\phi = \pi$ 86

Figure 5.7: Reconstruction surfaces with $\delta=10$ mm, $d=15$ mm, $f=15$ kHz and varying phase angle at source location scenario 3 – a) reconstruction surface of incoherent sources (baseline); b) Standard HELS reconstruction surface with $\phi = 0$; c) Standard HELS reconstruction surface with $\phi = \pi/4$; d) Standard HELS reconstruction surface with $\phi = \pi/2$; e) Standard HELS reconstruction surface with $\phi = 3\pi/4$; f) Standard HELS reconstruction surface with $\phi = \pi$ 87

Figure 5.8: Reconstruction surfaces with $\delta=10$ mm, $d=15$ mm, $f=15$ kHz and varying phase angle at source location scenario 3 – a) reconstruction surface of incoherent sources (baseline); b) Modified HELS reconstruction surface with $\phi = 0$; c) Modified HELS reconstruction surface with $\phi = \pi/4$; d) Modified HELS reconstruction surface with $\phi = \pi/2$; e) Modified HELS reconstruction surface with $\phi = 3\pi/4$; f) Modified HELS reconstruction surface with $\phi = \pi$ 88

CHAPTER 1: INTRODUCTION

Nearfield Acoustical Holography (NAH) has become an important tool in the diagnosis and evaluation of noise and vibration in many industries and fields. Since its introduction by Maynard and Williams¹⁻³ in the early 1980s, NAH's ability to determine the propagation and reconstruction of sound radiation has helped engineers understand the fundamental acoustical properties of NVH (noise, vibration and harshness) problems. Particular interest has been paid to NAH due to its ability to determine source locations and the accompanying sound field's acoustical quantities by pressure measurements alone. The essence of NAH is the requirement to capture pressure waves in the nearfield. By doing so, information regarding evanescent waves is captured, and a better understanding of the energy transfer of the source plane to the environment can be determined.

Most, if not all of the NAH research done is with source surfaces which are significantly larger than the measurement devices (microphones). However, as technology advances, components are becoming smaller, and localization of vibration and acoustical properties are becoming more difficult without high resolution scanning of the surface. Industries ranging from computers to hydraulic control systems could use NAH to determine defects in motherboards or resonant acoustical noises within hydraulic subsystems. Unfortunately, application of NAH to these fields is somewhat limited by the resolution restrictions inherent of current methods.

All NAH methods are based on relating surface pressures or velocities to pressures measured in the radiated field. In a prediction problem, these relationships are well-posed and solutions are stable⁴. However, in NAH the inverse problem is solved, i.e. the measured field pressure is used to reconstruct the surface pressure or velocity. Inverse problems usually result in ill-posed problems that produce unstable solutions. Over the years, three factions of inverse

Fourier Acoustics have been of significant development: Fourier Acoustics, Helmholtz Integral Equation (HIE) methods and Least Squares Approximation Methods (LSAM).

Fourier Acoustics is the first generation of NAH developed by Williams and Maynard¹⁻³. This method is based on relating acoustic pressure or velocity of two parallel surfaces by the Rayleigh integral formulas. Unfortunately, the use of the Fourier Transform restricts Fourier Acoustics to separable coordinate systems, limiting real-world application of the method. Also, spatial discretization of the Fourier Transform and the parallel surfaces can require a high density of measurements to provide high resolution reconstruction.

HIE was developed from the need to reconstruct non-separable geometries and is based on solving the discrete Helmholtz Integral Equation⁵. The most popular method of solving the Helmholtz Integral Equation is by the Inverse Boundary Element Method (IBEM), first introduced by Gardner and Bernhard⁶. The major drawback of HIE is calculation time due to measurement requirements. HIE typically requires a minimum of 2π or 6 nodes per structural wavelength. For complex structures with high orders of modes, the number of discrete nodes, and consequently number of measurement points, can be quite high.

In the case of LSAM, the Helmholtz equation is directly solved by relating measured and reconstructed quantities through a matrix of basis functions, similar to the Rayleigh-Ritz method used in vibration of structures⁷. The basis functions are series expansions of eigenfunction solutions of the Helmholtz equation. LSAM holds significant advantages over Fourier Acoustics and HIE in terms of measurement and calculation time due to minimum measurement requirements. The major disadvantages of LSAM are that no single coordinate system is best for all surface geometries and the method is an approximate solution to the Helmholtz equation. Therefore, high resolution reconstruction with HIE or Fourier Acoustics provides a better

solution than LSAM with ideal test conditions. More detailed pros and cons of each methodology have been summarized by Wu⁸ as well as Magalhães and Tenenbaum⁹.

In practical applications, the resolution requirement must take into account noise in the measurement data. As stand-off distance increases, energy due to high frequency evanescent waves may become masked by noise. Williams formulated resolution requirements based on the effects of noise and stand-off distance for Fourier Acoustics⁵

$$R = \frac{20\pi(z_h - z_s)}{D \ln(10)} \quad (1.1)$$

Where $z_h - z_s$ is the stand-off distance between the measurement surface and the reconstruction surface and D is the dynamic range (encompasses SNR). Note that equation 1.1 is not dependent on the wavelength of the reconstructed excitation frequency. Therefore, as noise or stand-off distance decreases, finer spatial resolution results as long as spatial aliasing does not occur due to under-sampling. Though equation 1.1 was formulated from Fourier Acoustics, the guideline is usually applied to all NAH methods.

In cases such as a computer motherboard, the guidelines set by the spatial resolution equation may prove difficult to adhere to due to potential dense areas of coherent sources. Such requirements impose significant hardware and calculation requirements when reconstruction of high resolution and high frequency excitations are required. In the case of LSAM, significant advantages in reconstruction and prediction of the acoustic field are obtained through the representation of the field as an expansion of basis functions. By approximating the field in this way, it is possible to synthesize any point in the field provided that the basis functions are solutions to the Helmholtz equation and are good approximation of the acoustic radiation of the sources. Even in cases where the basis functions are not ideal fits to the sound radiation pattern, least-squares minimizes the L2-norm error to provide the best possible solution for the functions

used and input data. In effect, least-squares modifies the basis functions to match the field radiation pattern produced at the measurement positions. The approximation methodology of LSAM significantly reduces measurement and computation requirements over other methods.

The synthesis of field locations' acoustic properties leads to an interesting question. Since any field point can be reconstructed or predicted from a more coarse measurement array than the requested surface, do NAH's spatial resolution guidelines apply to LSAM methods? The objective of this thesis is to investigate this question in terms of the LSAM method, Helmholtz Equation Least Squares (HELs), developed by Wu¹⁰. A modified variant of HELs specifically suited for point sources is also presented. Planar Fourier Acoustics will be used for comparison of resolution and accuracy.

The dissertation will be organized as follows:

- Ch. 2 presents a literature review of NAH methods and an alternative approach to sampling of measurement data.
- Ch.3 provides theoretical background of Fourier Acoustics, HELs and sampling theory. A brief overview of regularization techniques is also given.
- Ch. 4 defines the problem statement in terms of a numerical model of two coherent point sources with varying parameters. Simulation results are presented and analyzed.
- Ch. 5 discusses results from experimental testing of approximate coherent sources in a lab environment.
- Ch. 6 draws conclusion from the numerical and experimental data. Future areas of work are also presented.

CHAPTER 2: LITERATURE REVIEW

The literature review focuses on the development of Fourier Acoustics (in particular Planar NAH), Helmholtz Integral Equations based methods and Helmholtz Equations Least Squares. In particular the pros and cons of each method with regards to reconstruction resolution are reviewed. In addition, a brief overview of Compressed Sensing is given based on its ability to violate the Nyquist sampling rate. Though compressed sensing is not an NAH method, it is being investigated in a number of imaging fields. HELS' ability to violate the Nyquist sampling rate by synthesizing field data points makes Compressed Sensing a pertinent discussion point.

Fourier Acoustics

Fourier Acoustics was introduced in 1980 by Williams and Maynard¹ as the first method of NAH. In this groundbreaking paper, Fourier Acoustics is developed based on extending reconstruction limitations that traditional holography encountered in optical imaging. In the case of optical holography, the spatial reconstruction resolution is limited to the emitted wavelength of the source. The paper explains that the limitation is not intrinsic to the problem, but rather a result of the hardware not being fast enough to detect the wave in real time. As a result, measurements are always a number of wavelengths away from the source and high frequency energy is lost prior to reaching the detector. The high frequency energy that does not reach the farfield encompasses the fine details of the wave. If the entire frequency spectrum is known, reconstruction resolution is only limited based on noise and the amount of the high frequency energy captured.

Applying this theory to acoustical imaging has significant advantages. Acoustic waves produce much larger wavelengths than optical waves, and can easily be detected. Therefore, if measurements are made very close to the source surface, high wavenumber energy that decays

prior to the farfield (evanescent waves) can be captured. The information contained within the evanescent waves removes the wavelength resolution limit of optical holography.

The method is based on Rayleigh's first and second integrals, which are a special case of the Helmholtz integral equation^{2,11}. Discussions of Fourier Acoustics normally start with Rayleigh's second integral relating pressure between two parallel surfaces. Applying Euler's equation¹² to Rayleigh's second integral equation produces Rayleigh's first integral equation relating velocity on one surface to the pressure on a parallel surface. Together, Rayleigh's first and second integrals provide information required in calculating the average normal acoustic intensity, $\vec{I}(\omega)$. Acoustic intensity provides information about the energy flow from a surface and is used in calculating acoustic power, $\Pi(\omega)$. Acoustic power is the standard metric in evaluating NVH levels in practice¹³⁻¹⁴. The average normal acoustic intensity and acoustic power equations are shown below

$$\vec{I}(\omega) = \frac{1}{2} Re(p(\omega)\vec{v}(\omega)^*) \quad (2.1)$$

$$\Pi(\omega) = \oint \vec{I}(\omega) \cdot \hat{n} dA \quad (2.2)$$

Where * indicates, the complex conjugate, *Re* the real part, and \hat{n} the outward normal vector of the surface.

Tables 1-3 summarize Fourier Acoustics for planar, cylindrical and spherical coordinate systems relating the surface and hologram surfaces (measurement surfaces, denoted by *s* and *h* subscripts, respectively):

Table 2.1: Planar Fourier Acoustics coordinate system equations

$p(x, y, z; \omega) = \mathcal{F}_x^{-1} \mathcal{F}_y^{-1} \{ \mathcal{F}_x \mathcal{F}_y [p(x, y, z_h; \omega)] G_p(k_x, k_y, z_s - z_h) \},$
 $v_n(x, y, z; \omega) = \mathcal{F}_x^{-1} \mathcal{F}_y^{-1} \{ \mathcal{F}_x \mathcal{F}_y [p(x, y, z_h; \omega)] G_v(k_x, k_y, z_s - z_h) \},$

where

$$G_p(k_x, k_y, z_s - z_h) = e^{ik_z(z_h - z_s)},$$

$$G_v(k_x, k_y, z_s - z_h) = \frac{k_z}{\rho_0 c k} e^{ik_z(z_h - z_s)},$$

and

Planar
Fourier
Acoustics

$$\mathcal{F}_x \mathcal{F}_y [\varphi] = \int_{-\infty}^{\infty} \int_{-\infty}^{\infty} \varphi e^{-ik_x x} e^{-ik_y y} dx dy,$$

$$\mathcal{F}_\theta^{-1} \mathcal{F}_\phi^{-1} [\Phi] = \frac{1}{4\pi^2} \int_{-\infty}^{\infty} \int_{-\infty}^{\infty} \Phi e^{ik_x x} e^{ik_y y} dk_x dk_y,$$

$$k_z = \sqrt{k^2 - k_x^2 - k_y^2}$$

Table 2.2: Cylindrical Fourier Acoustics coordinate system equations

$p(r_s, \phi, z; \omega) = \mathcal{F}_\phi^{-1} \mathcal{F}_z^{-1} \{ \mathcal{F}_\phi \mathcal{F}_z [p(r_h, \phi, z; \omega)] G_p(k_\phi, k_z, r_s - r_h) \},$
 $v_n(r_s, \phi, z; \omega) = \mathcal{F}_\phi^{-1} \mathcal{F}_z^{-1} \{ \mathcal{F}_\phi \mathcal{F}_z [p(r_h, \phi, z; \omega)] G_v(k_\phi, k_z, r_s - r_h) \},$

where

$$G_p(k_\phi, k_z, r_s - r_h) = \frac{H_n^{(1)}(k_r r_s)}{H_n^{(1)}(k_r r_h)},$$

$$G_v(k_\phi, k_z, r_s - r_h) = \frac{H_n'^{(1)}(k_r r_s)}{i \rho_0 c H_n^{(1)}(k_r r_h)},$$

and

Cylindrical
Fourier
Acoustics

$$\mathcal{F}_\phi \mathcal{F}_z [\varphi] = \frac{1}{2\pi} \int_0^{2\pi} \int_{-\infty}^{\infty} \varphi e^{-in\phi} e^{-ik_z z} d\phi dz,$$

$$\mathcal{F}_\theta^{-1} \mathcal{F}_\phi^{-1} [\Phi] = \sum_{n=-\infty}^{\infty} \int_{-\infty}^{\infty} \Phi e^{in\phi} e^{ik_z z} dk_z,$$

$$k_r = \sqrt{k^2 - k_z^2}$$

Table 2.3: Spherical Fourier Acoustics coordinate system equations

$$p(r_s, \theta, \phi; \omega) = \mathcal{F}_\theta^{-1} \mathcal{F}_\phi^{-1} \{ \mathcal{F}_\theta \mathcal{F}_\phi [p(r_h, \theta, \phi; \omega)] G_p(k_\theta, k_\phi, r_s - r_h) \},$$

$$v_n(r_s, \theta, \phi; \omega) = \mathcal{F}_\theta^{-1} \mathcal{F}_\phi^{-1} \{ \mathcal{F}_\theta \mathcal{F}_\phi [p(r_h, \theta, \phi; \omega)] G_v(k_\theta, k_\phi, r_s - r_h) \},$$

where

$$G_p(k_\theta, k_\phi, r_s - r_h) = \frac{h_n^{(1)}(kr_s)}{h_n^{(1)}(kr_h)},$$

$$G_v(k_\theta, k_\phi, r_s - r_h) = \frac{h_n'^{(1)}(kr_s)}{i\rho_0 c h_n^{(1)}(kr_h)},$$

Spherical
Fourier
Acoustics

and

$$\mathcal{F}_\theta \mathcal{F}_\phi [\varphi] = \int_0^{2\pi} \int_0^\pi \varphi Y_n^m(\theta, \phi) \sin\theta d\theta d\phi,$$

$$\mathcal{F}_\theta^{-1} \mathcal{F}_\phi^{-1} [\Phi] = \sum_{n=0}^{\infty} \sum_{m=-n}^n \Phi Y_n^m(\theta, \phi)^*$$

Fourier Acoustics has been studied extensively since its introduction^{2, 15-18}. However, the range of study is limited to separable geometries. Sources closely approximating a plate under forced vibration¹⁹, or sound radiation from a vibrating cylinder²⁰, can be characterized well by Fourier Acoustics. If Fourier Acoustics is applied to surfaces that do not align with separable geometries, errors in reconstruction will increase due to increased stand-off-distances at low surface height regions. Also, reconstruction is only valid to the surface variant of the applied Fourier Acoustics method.

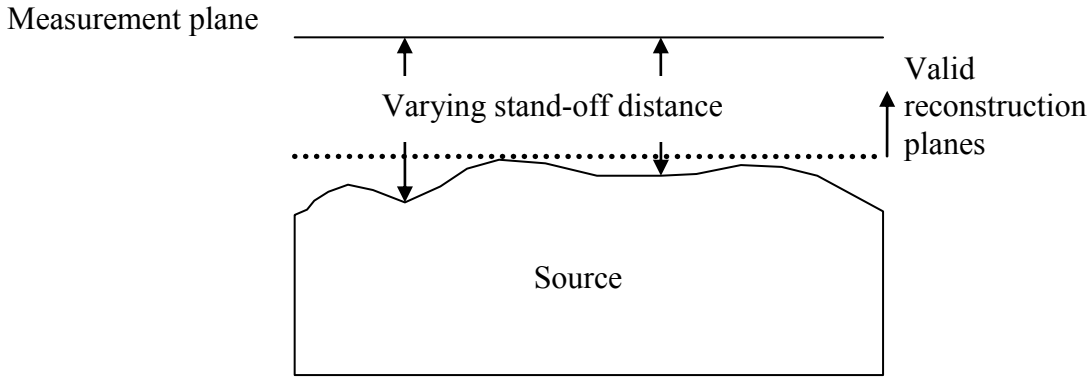


Figure 0.1: Schematic of Planar Fourier Acoustics used on source with non-separable geometry

One of the major drawbacks of Fourier Acoustics results from the use of the Discrete Fourier Transform (DFT). Discretization of the hologram (measurement) and source surface, along with the discretization of the Fourier Transform, may cause spatial aliasing, edge effects and replicated sources. Spatial aliasing can only be remedied by increased measurement resolution, which in turn increases the maximum k-space wavenumber (frequency). In cases where high reconstruction resolution is required, patch methodologies²¹ have been developed to minimize the difficulties in taking measurements in close proximity to one another or over large areas of measurements²²⁻²³. Edge effects and source replication can be remedied by wavenumber filters such as the Tukey filter²⁴, as well as methods to extend the measurement plane without taking additional data²⁵. These methods limit the steep fall-off of spatial wavenumbers that cause source replication.

Helmholtz Integral Equation

Helmholtz Integral theory¹² transforms the Helmholtz equation from a differential equation to an integral equation by applying Green's theorem²⁶. The resulting integral equation is termed Helmholtz Integral Equation (HIE) and is defined as follows²⁷

$$c(\mathbf{r})p(\mathbf{r}) = \int_{S_0} \left[p(\mathbf{r}_0) \frac{\partial G\left(\frac{\mathbf{r}}{\mathbf{r}_0}\right)}{\partial n_0} - \frac{\partial p(\mathbf{r}_0)}{\partial n_0} G\left(\frac{\mathbf{r}}{\mathbf{r}_0}\right) \right] dS \quad (2.3)$$

Where \mathbf{r}_0 is the surface pressure and $R = |\mathbf{r} - \mathbf{r}_0|$ is the distance from the field point \mathbf{r} and the surface point \mathbf{r}_0 . G is the free-space Green's function

$$G\left(\frac{\mathbf{r}}{\mathbf{r}_0}\right) = \frac{e^{-ikR}}{R} \quad (2.4)$$

* Patch methodologies are not solely attributed to Fourier Acoustics, therefore the reader will notice that some of the referenced papers are pertaining to other NAH methods

The most popular method of solving the HIE for the inverse problem is by Inverse Boundary Element Methods (IBEM). In IBEM, the HIE is represented by a set of matrix functions,

$$\begin{aligned} [D]_s \{p\}_s &= [M]_s \{v_n\}_s \\ \{p\}_f &= [D]_f \{p\}_s + [M]_f \{v_n\}_s \end{aligned} \quad (2.5, 2.6)$$

Where $[D]_s$ and $[M]_s$ are dipole and monopole matrices on the source surface, and $[D]_f$ and $[M]_f$ are the corresponding matrices of the field pressures. Accordingly, $\{p\}_f$ represents the field pressures, whereas $\{p\}_s$ and $\{v_n\}_f$ represent the surface pressure and normal surface velocity, respectively.

IBEM was first introduced by Gardner and Bernhard⁶ through numerical simulations. Formal derivations were later provided by Maynard and Veronesi²⁸ along with the implementation of Singular Value Decomposition²⁹ (SVD) to solve the acoustic pressure and normal velocity. IBEM's significant advantage over Fourier Acoustics stems from the ability to analyze arbitrary surfaces by using measurements which conform to the surface³⁰.

IBEM in conjunction with the SVD has been applied in a number of applications³¹⁻³⁸. However, due to the discretization of the source surface and Helmholtz Integral Equation, measurement requirements are often high to ensure satisfactory spatial resolution in reconstruction. Though the literature did not specify requirements for measurement spacing requirements, the rule of thumb is usually 6 or 2π nodes per wavelength⁸.

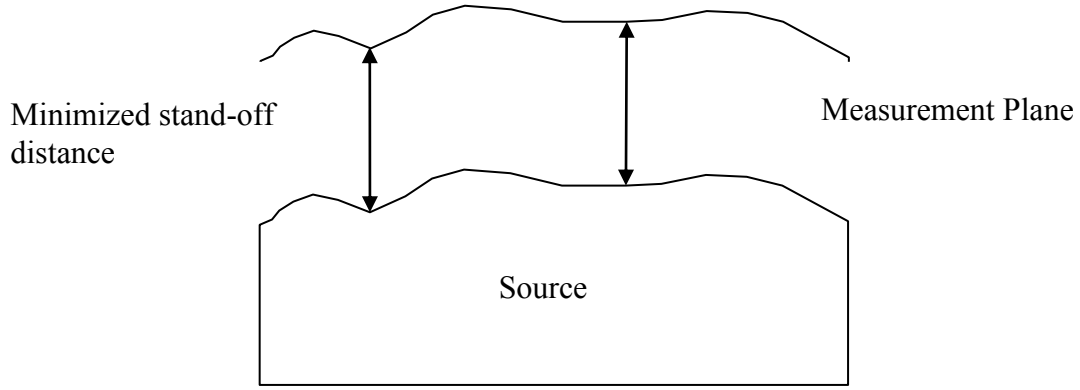


Figure 0.2: Schematic of conformal surface measurement possible with IBEM

Helmholtz Equation Least Squares

Helmholtz Equation Least Squares (HELs) was first introduced by Wang and Wu¹⁰ to reconstruct surface pressure in exterior problems. HELs directly solves the Helmholtz equation by approximating the solution with an expansion of admissible basis functions

$$\hat{p}_r(\vec{x}_r; \varpi) = G(\vec{x}_r | \vec{x}_m) \hat{p}_m(\vec{x}_m; \varpi) \quad (2.7)$$

Where the transfer function, $G(\vec{x}_r | \vec{x}_m)$ is defined as

$$G(\vec{x}_r | \vec{x}_m) = \psi_r \psi_m^\dagger \quad (2.8)$$

and the measurement and reconstruction surfaces are represented by m and r subscripts, respectively. The basis functions, ψ , are usually localized spherical expansion functions. The expansion coefficients are solved for by matching the assumed form solution to the pressures measured in the nearfield. Approximations of the coefficients are minimized through least-squares. The corresponding velocity equation is calculated by applying Euler's equation to the field pressure

$$\hat{p}_r(\vec{x}_r; \varpi) = \frac{1}{i\omega\rho_0} \vec{\nabla}(G(\vec{x}_r | \vec{x}_m) \hat{p}_m(\vec{x}_m; \varpi)) \cdot \vec{n} \quad (2.9)$$

Application of pressure reconstruction from the exterior domain has been shown for a structure similar to a vehicle front end³⁹ and a vibrating bowling ball⁴⁰. The method was further extended to vibroacoustic analysis by Lu and Wu for a vibrating plate⁴¹⁻⁴². In terms of the interior domain, Yu and Wu formulated the corresponding equations and provided numerical examples⁴³.

The significant advantage of HELS over other methods is the reduction of measurements required due to the synthesis of field points. Similar to HIE methods, HELS is capable of conformal measurement surfaces, thus non-separable geometries can be reconstructed. However, the method is not as accurate as HIE methods since it is an approximation to the solution based on expansion functions. In practical applications, truncation of the expansion functions is required and the exact solution cannot be calculated. However, in many cases, the error in reconstruction is acceptable in exchange for significant reduction in measurement and calculation time.

Sub-Nyquist sampling theory

Nyquist's definition of minimum sampling in time or space is defined as

$$f_s = \frac{f_{max}}{2} \quad (2.10)$$

Where f_s is the sampling rate and f_{max} is the maximum frequency of the signal. Violation or "sub-Nyquist" research has increased in popularity over the last decade with a technique called "Compressed Sensing"⁴⁴⁻⁴⁸. Compressed Sensing advantageously uses signal sparseness⁴⁹ and random sampling of a signal to reconstruct at sub-Nyquist sampling rates. Surprisingly, sparse, or at least compressible⁵⁰, data is evident in much of the real world. Images that do not contain a significant amount of Fourier content, i.e. images that do not contain many changes from pixel to pixel, are likely sparse. Fields where Compressed Sensing is being investigated are

telecommunications, magnetic resonance imagery, seismology, digital photography and other applications where data sizes are large.

Compressed Sensing is a method of solving a sparse linear eigenvalue problem

$$Ax = b \quad (2.11)$$

where A represents the transfer matrix from the given NAH method. In the case of an inverse problem, x is solved for by the least-squares method. Unlike classical methods, Compressed Sensing solves the problem based on random sampling of data points, and using the L1-norm instead of the L2-norm in reconstruction⁵¹. Random sampling of data points results in random sampling of the Fourier coefficients (or in the case of NAH, wavenumbers). The random sampling leads to the possibility of missing the highest amplitude coefficients. However, since compressed sensing is used on large sample sizes of data, the frequency resolution of the spectrum is high and some component of the major peaks is captured.

Cases such as MRIs and seismology normally require hundreds of thousands, if not millions of data points. Even after the random selection of measurement points, the selected data is normally in the range of 10% of the original set⁵². In NAH, and in particular the examples to be presented, the number of measurements and frequency resolution are much lower. Even if the data is sparse, the number of available Fourier coefficients is quite small. Therefore, random selection of Fourier coefficients that produce satisfactory reconstruction may not be feasible.

CHAPTER 3: THEORETICAL BACKGROUND

Chapter 3 provides theoretical background and formulations of the methodologies used to investigate the resolution guidelines of NAH. Pressure formulations of Planar Fourier Acoustic and examination of the corresponding spatial resolution guidelines are discussed, followed by pressure formulations of HELS and Modified HELS. The chapter concludes with a brief overview of regularization theory.

Planar Fourier Acoustics method

Fourier Acoustics was first introduced by Maynard and Williams¹ and is based on Rayleigh's integral formulas for planar, cylindrical and spherical coordinates. Rayleigh's first and second integral formulas define relationships between the spatial pressure at one plane and the spatial velocity or pressure at a parallel plane, respectively. In the present thesis, the planar variant of Fourier Acoustics was used due to the ease of application in real-world scenarios.

Rayleigh's second integral formula for a planar coordinate system is defined as

$$\hat{p}(x_s, y_s, z_s) = \frac{1}{4\pi^2} \iint e^{ik_x(z_s - z_h)} \left(\iint \hat{p}(x_h, y_h, z_h) dx dy \right) dk_x dk_y \quad (3.1)$$

$k_z = \sqrt{k^2 - k_x^2 - k_y^2}$ is the z-component of the spatial wavenumber, \vec{k} , describing the direction of the radiating pressure. \vec{k} is based on the acoustic angular frequency, ω ; the speed of the acoustic wave, c ; and the outward normal direction of the propagating wave \vec{n} .

$$\vec{k} = \frac{\omega}{c} \vec{n} \quad (3.2)$$

In equation (3.1), z_s is the location of the pressure plane to be calculated and z_h is the location of the measurement plane.

Also of significant importance in equation (3.1) is the integral

$$P(k_x, k_y) = \iint \hat{p}(x_h, y_h, z_h) dx dy \quad (3.3)$$

defined as the angular spectrum of the surface. The angular spectrum is the k-space representation of the surface pressure (or velocity) and provides an understanding of the in-plane frequency content of the surface. For example, in the case of a vibrating plate, the angular spectrum would illustrate the structural vibration frequency content of the plate. The angular spectrum also provides a role in the definition of NAH resolution guidelines.

In practical applications, measurement and reconstruction surfaces are discrete. Consequently, a matrix representation of equation (3.1) is formulated. The matrix representation of Rayleigh's second integral is defined as

$$\hat{P}_{mx1} = F_{m,n}^H G F_{m,n} \hat{p}'_{mx1} \quad (3.4)$$

Where G is a diagonal matrix containing the transfer functions of the discrete set of k_z

$$G = \text{diag}(e^{ik_z(z_s - z_h)}) \quad (3.5)$$

and

$$F_{m,n} = \frac{1}{\sqrt{N}} e^{\frac{-2\pi i(m-1)(n-1)}{N}}, \quad m, n=1 \dots N \quad (3.6)$$

is the discrete Fourier Transform and $F_{m,n}^H$ is its conjugate. The pressures at the measurement and reconstruction surfaces are represented as column vectors \hat{p}'_{mx1} and \hat{p}_{mx1} , respectively. The analogous discrete angular spectrum is

$$\hat{P}_{mx1} = F_{m,n} \hat{p}'_{mx1} \quad (3.7)$$

In a reconstruction problem, $z_s - z_h$ is a positive value, which leads (equation 3.4) to an exponentially increasing function. Though an exponential increase in pressure intuitively

matches expectations with decreasing distance, error or noise in the measurement plane also increases exponentially. Noise is of particular importance since it is associated with high frequency wavenumber content. Since Fourier Acoustics and NAH methods both generally use the entire wavenumber spectrum to increase resolution, even a small amount of measurement error or noise in the measurement plane can lead to significant error in the reconstruction plane. In order to minimize the effects error in reconstruction, regularization techniques must be employed.

Williams and Maynard provide reconstruction resolution guidelines for Fourier Acoustics¹. The principals of the formulation are based on the exponential decay of evanescent waves as the acoustic wave propagates from the source surface. The reconstruction resolution limits are based on dynamic range (D) and stand-off distance ($z_h - z_s$)

$$R = \frac{20\pi(z_h - z_s)}{D \ln(10)} \quad (1.1)$$

The dynamic range of the systems is the range of input levels that can be usefully transmitted in the system. Dynamic range can be affected by background noise, electrical resistance and the acoustical characteristics of the test environment⁵³. The dynamic range can be thought of as the difference between the ideal and non-ideal measurement due to measurement error and noise.

Usually, background noise corresponds to high wavenumber content based on the randomness of the error, and leads to non-smooth distortion of the measurement field. As stand-off distance increases, less evanescent wave energy reaches the measurement array. Consequently, less information regarding high wavenumber content is captured. If the noise of the system produces a low Signal to Noise Ratio (SNR), the evanescent wave energy cannot be distinguished and resolution in reconstruction is reduced.

Williams and Maynard formulated equation (1.1) based on a two dimensional radiator. Williams later summarized the formulation of the resolution requirement as follows⁵:

Using equations (3.1) and (3.2), the relationship between the angular spectrum at the measurement and source surfaces is

$$P(k_x, 0, z_h) \approx P(k_x, 0, z_s)e^{-ik_z(z_h-z_s)} \quad (3.8)$$

For supersonic wave (non-evanescent waves) k_z , is real and the magnitude of the energy radiation is constant with increasing distance from the source. When the wave is evanescent, the wavenumber, k_z , is imaginary and the radiation of acoustic energy decreases with increasing distance from the source, producing a well-posed problem⁴. However, in reconstruction, the evanescent energy increases. Thus any errors in measurement increase exponentially with increasing stand-off distance, and may cause the problem to become ill-posed.

Williams attempts to limit the effects of noise on reconstruction by calculating the stand-off distance required to ensure that non-evanescent waves are not masked by the exponential increasing magnitude of the evanescent waves noise. In order to do so, the dynamic range (or SNR), D , must be greater than $e^{k_c(z_h-z_s)}$. Where the D is in decibels and k_c is the wavenumber cutoff which is usually greater than the highest wavenumber of interest.

$$10^{D/20} > e^{k_c(z_h-z_s)} \quad (3.9)$$

Defining k_c as $\frac{2\pi}{\lambda_c}$ and setting the resolution to be half the Nyquist rate of the corresponding cutoff wavelength, λ_c , the resolution limit becomes

$$R_x > \frac{20\pi(z_s - z_h)}{D \ln(10)} \quad (3.10)$$

Note that the resolution limit does not take into account phase angle, excitation frequency and sampling resolution. Williams formulates equation (3.10) assuming spatial sampling rates of

the measurement plane do not violate the Nyquist rate. Since the Nyquist rate requirement is met, spatial aliasing does not occur. Williams states that reconstruction spatial resolution is not based on the source excitation wavelength, which in itself is quite surprising if one does not examine the formulation of equation (3.10).

NAH resolution limits and spatial sampling theory

At this point, an important distinction must be emphasized in spatial resolution limitations. Spatial resolution can be limited by insufficient knowledge of the wavenumber spectrum and spatial aliasing. Since the DFT is used in Fourier Acoustics, the spatial Nyquist rate must be met to ensure sources of high wavelengths and significant energy are not distorted. In contrast, HELS methodologies do not use the DFT and are not limited by the Nyquist rate during measurement. Thus, the question posed concerning the validity of equation (3.10) with regards to HELS is produced. Before exploring HELS, a brief review of spatial sampling is provided.

Uniform discrete sampling can be mathematically described by Shannon's sampling theorem (also known as the Whittaker-Shannon-Kotel'nikov sampling theorem, or the acronym WSK sampling theorem)⁵⁴

“If a function of time is limited to the band from 0 to W cycles per second, it is completely determined by giving its ordinate at a series of discrete points spaced $1/2W$ seconds apart in the manner indicated by the following result: If $f(t)$ has no frequencies over W cycles per second, then

$$f(t) = \sum_{n=-\infty}^{\infty} f\left(\frac{n}{2W}\right) \frac{\sin \pi(2Wt-n)}{\pi(2Wt-n)},$$

Though the theorem was initially stated for time based systems, application of the theorem is valid for any equidistantly spaced coordinate system.

Use of the DFT invokes the use of the WSK theorem, and consequently Shannon's requirement of discrete points spaced $1/2W$ seconds apart, which is historically known as the

Nyquist rate. Violation of the Nyquist rate leads to aliasing, which distorts frequencies above the Nyquist sampling rate to appear as lower frequencies. The DFT, and discrete sampling in general, also may lead to discrete ill-posed problems. Discrete ill-posed problems are ill-conditioned and may cause inverse problem solutions to be unstable during reconstruction.

Applying equation (3.10) and Nyquist spatial sampling requirements incur significant restrictions on the measurement array. For example, if two coherent sources separated by 10 mm are required to be reconstructed with an SNR of 20 dB, the maximum stand-off distance would be 7.33 mm with a corresponding minimum measurement spacing of 5 mm. The minimum measurement spacing requirement is not necessarily a sufficient in real-world applications.

Depending on the proximity of the sources to the microphone locations, relative error of up to 50% can be realized with respect to the spacing of the sources when the minimum measurement spacing is used. To improve reconstructed source localization, a more refined measurement surface must be taken. However, with typical free-field microphone dimensions of 6.35 mm⁵⁵, multiple measurement patches would be required leading to more measurement and computation time.

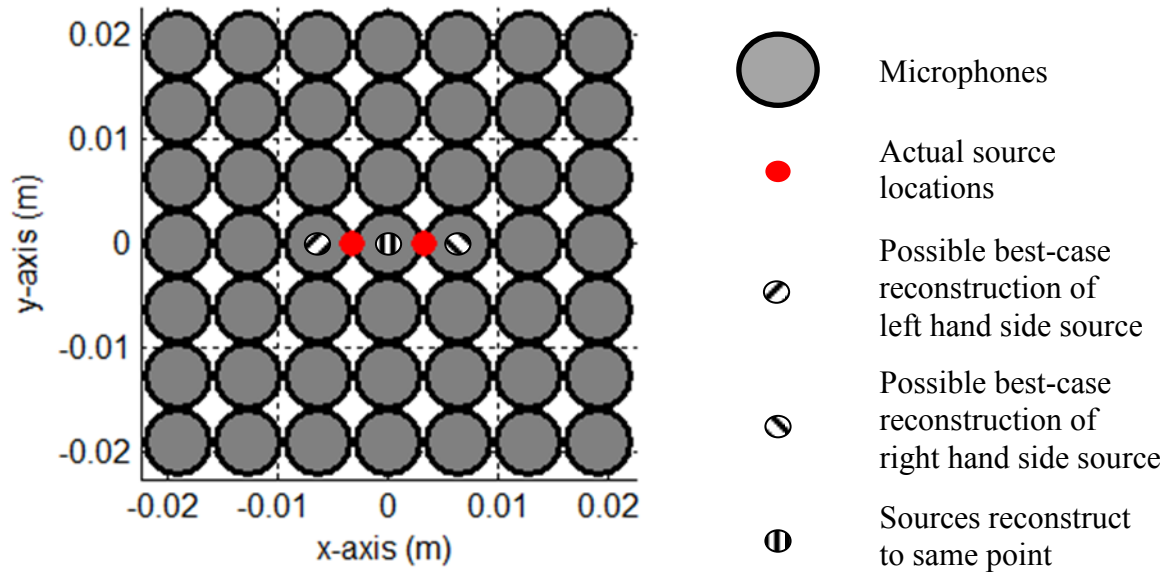


Figure 0.1: Feasible source reconstruction locations with 6.35 mm microphones spaced at minimal measurement spacing

Kim and Nelson investigated Williams NAH spatial resolution guidelines numerically based on a plate with a single point source^{56, 57}. The paper discusses ill-conditioning of the transfer matrix and how the condition number of the matrix relates to the spatial resolution in reconstruction. Kim and Nelson concluded that the “super-resolution” provided by NAH is feasible in theory, but resolution significantly beyond the half wavelength limit may be difficult to reproduce in practice. In particular, as the number of measurement points and/or sources increase, the transfer matrix becomes more ill-conditioned.

Helmholtz Equation Least Squares (HELs) method

The HELs formulation solves the Helmholtz equation with the Sommerfield radiation condition as the boundary condition directly by applying LSAM. LSAM was first introduced by Meecham⁵⁸ as a variational method of determining the Fourier coefficients for the Rayleigh expansion approximation of scattered waves on a periodic surface in prediction. LSAM was

proven in back-propagation by Isakov and Wu⁵⁹, and HELS was proven as a special case of LSAM by Semanova and Wu⁶⁰.

HELs defines the pressure distribution $\hat{p}(\vec{x}; \varpi)$ as

$$\hat{p}(\vec{x}; \varpi) = \psi_j(\vec{x}; \varpi) C_j(\varpi) \quad (3.11)$$

Where $\hat{p}(\vec{x}; \varpi)$ is the pressure distribution of the field defined by a j term expansion of the admissible basis functions, $\psi(\vec{x}; \varpi)$; and $C(\varpi)$ are weighting coefficients (HELs coefficients). $\psi(\vec{x}; \varpi)$ are a combination of spherical Hankel and spherical harmonic functions that are solutions to the Helmholtz equation. The basis functions are of the form

$$\psi(\vec{x}; \varpi) = \psi_{nl}(r, \theta, \phi; \varpi) = h_n^{(1)}(kr) Y_n^l(\theta, \phi) \quad (3.12)$$

The HELs expansion level is defined as $j = n^2 + n + l$, with n varying from 0 to N and l varying from $-n$ to n .

HELs coefficients are determined by solving an overdetermined linear system of equations produced from equating the assumed form solutions to the measured pressures and then using least squares to minimize the errors. The HELs method can be summarized as follows:

1. Define the measured and reconstructed pressures $\hat{p}_m(\vec{x}_m; \varpi)$ and $\hat{p}_r(\vec{x}_r; \varpi)$, respectively

$$\hat{p}_m(\vec{x}_m; \varpi) = \psi_m(\vec{x}_m; \varpi) C(\varpi) \quad (3.13)$$

$$\hat{p}_r(\vec{x}_r; \varpi) = \psi_r(\vec{x}_r; \varpi) C(\varpi) \quad (3.14)$$

2. Solve for the expansion coefficients from equation (3.13), i.e. HELs coefficients

$$\psi_m^H(\vec{x}_m; \varpi) \hat{p}_m(\vec{x}_m; \varpi) = C(\varpi) \quad (3.15)$$

3. Calculate the desired pressure field points

$$\hat{p}_r(\vec{x}_r; \varpi) = G(\vec{x}_r | \vec{x}_m) \hat{p}_m(\vec{x}_m; \varpi) \quad (3.16)$$

Where $G(\vec{x}_r | \vec{x}_m) = \psi_r \psi_m^\dagger$ is a transfer function relating the pressures at any point in the field to the measured pressures.

Relationships between stand-off distance and frequency content are given by Wu⁶¹ based on the characteristic radius of the source object, the wave number to be reconstructed and the stand-off distance of the measurement plane. The given relationships essentially describe the nearfield of the surface as the valid region of HELS when applied to an inverse problem

$$\begin{aligned} d &\ll a \\ d &\ll \lambda_{\min} = c / f_{\max} \\ d &\ll \frac{k_{\max} a^2}{2} \end{aligned} \quad (3.17, 3.18, 3.19)$$

Wu also states that spatial resolution is not based on measurement spacing, but rather on the synthesis of wave patterns through the expansion of the spherical Hankel functions and harmonics. As is the case with all NAH methods, issues may occur at higher frequency reconstruction due to the ill-conditioning of the system of equations. Regularization must be implemented to reduce such effects.

Comparison of the spherical variant of Fourier Acoustics and HELS shows that both methods rely on truncation of spherical harmonics and Hankel functions

$p(r_s, \theta, \phi; \omega) = \sum_{n=0}^{\infty} \sum_{m=-n}^n h_n^{(1)}(kr_s) Y_n^m(\theta_s, \phi_s) C(\omega)$	HELS measurement field equation
$p(r_r, \theta, \phi; \omega) = \sum_{n=0}^{\infty} \sum_{m=-n}^n h_n^{(1)}(kr_r) Y_n^m(\theta_r, \phi_r) C(\omega)$	HELS reconstruction field equation
$p(r_s, \theta, \phi; \omega) = \sum_{n=0}^{\infty} \sum_{m=-n}^n \left\{ \int_0^{2\pi} \int_0^\pi [p(r_h, \theta, \phi; \omega)] Y_n^m(\theta, \phi)^* \sin\theta d\theta d\phi \frac{h_n^{(1)}(kr_s)}{h_n^{(1)}(kr_h)} \right\}$	Spherical Fourier Acoustics reconstruction equation

However, HELS calculates a “fit” to the problem by calculating the HELS coefficients using least-squares. The HELS coefficients characterize the pressure radiation at the measurement field based on the locations of the measurement points with respect to the origin of the object. HELS relies on the fact that the field radiation pattern (not amplitude) should not change appreciably with distance, and the coefficients should hold at both the measurement and reconstruction surface. Error resulting from the use of spherical expansion functions at the measurement and reconstruction planes is minimized by altering the HELS coefficients to match the measured pressures. In the case of spherical Fourier Acoustics, significant error may result from using spherical harmonics for a planar surface since the pressure radiation is assumed to be from a spherical surface and no flexibility is provided otherwise. The flexibility of the HELS coefficients allows reconstruction of non-separable source geometries and reduced stand-off distances of measurement planes through conformal measurements⁶².

Modified HELS

At face value, the requirements required for HELS in equations (3.17-3.19) limit the spatial resolution of HELS to be the similar to other NAH methods, but with less measurements and calculation time required. However, Dziklinski and Wu indicate improved reconstruction is feasible through a modified HELS method⁶³ provided that the sources are monopoles (point sources). Dziklinski and Wu emphasize that Modified HELS is not likely applicable to distributed sources due to the weighting procedure.

Modified HELS incorporates a weighting multiplier to the measured pressures prior to application of the HELS algorithm. Where the weighted or “modified” pressure is defined as

$$\begin{aligned}
P_{\text{mod}} &= P_{w,\text{real}} + P_{w,\text{imag}} \\
P_{w,\text{real}} &= \left| \frac{\text{real}(p_n) - \text{mean}(\text{real}(p))}{\text{mean}(\text{real}(p))} \right| \\
P_{w,\text{imag}} &= \left| \frac{\text{imag}(p_n) - \text{mean}(\text{imag}(p))}{\text{mean}(\text{imag}(p))} \right|
\end{aligned} \tag{3.20, 3.21, 3.22}$$

In effect, the most significant contributions of the measured pressures are amplified. The reduction in lower pressure level contributions provides reasoning for not applying Modified HELS with distributed sources. In the case of a distributed source, the wave pattern at the source is approximately continuous and the peaks and valleys are smoother than in the case of point sources. The smoothness of distributed sources reduces the effectiveness in the weighting procedure since amplitude differences point to point are much less than with point sources.

Regularization methods

Due to the ill-posed nature of inverse problems, regularization is required to yield a well-posed problem that will produce satisfactory reconstruction results. Williams provides a summary of NAH regularization techniques applicable for Fourier Acoustics, HIE and LSAM methods⁶⁴. Semenova and Wu similarly summarize a number of regularization techniques applied to HELS⁶⁵. Maybe the most referenced summary of regularization techniques was done by Hansen⁶⁶. In his book, regularization techniques along, with their relation to rank-deficiency and discrete ill-posed problems, are discussed. However, a prevailing theme in most publication is no perfect regularization scheme exists for all problems. In fact, even when a regularization procedure works well, optimization of the regularization parameters for all cases is not necessarily feasible.

Regularization of inverse problems in practice usually depends on investigation and modification of the SVD of the transfer matrix. The SVD of any real or complex matrix A is defined as

$$A = USV^H = \sum_{i=1}^n u_i \sigma_i v_i^H \quad (3.23)$$

where U and V form a basis of orthogonal vectors (termed right and left singular vectors) and S is a diagonal matrix of singular values. The orthogonal vectors follow a pattern of oscillating sign, while the singular values are normally ordered in decreasing value. The decreasing singular values correlate to increasing wavenumbers similar to eigenvalues in the eigenvalue problem⁶⁷. The use of SVD for eigenvalue problems and similarities in their solutions in relation to NAH are summarized by the Williams paper mentioned above.

From the singular values, the condition number of the transfer function can be determined

$$\alpha = \frac{\sigma_{max}}{\sigma_{min}} \quad (3.24)$$

The condition number of a matrix is the quantity that controls the amount of error propagating from the data to the solution⁴. A high condition number relates to an ill-conditioned problem and is an effect of fine discretization of the measurement surface (discrete ill-posed) or significant noise in the measurement data (rank ill-posed). If a problem is ill-conditioned, a small perturbation in the measurement data can create a significant change in the reconstructed values. The objective of regularization is to minimize the condition number by modifying the singular value matrix of A by a filter f

$$A = USV^H = \sum_{i=1}^n u_i f_i \sigma_i v_i^H \quad (3.25)$$

SVD is often applied to invert rank deficient or nearly rank deficient matrices (i.e. the pseudo-inverse). As mentioned previously, inversion of the transfer matrices of both Fourier Acoustics and HELS methodologies may lead to unstable solutions due to discretization of the

measurement surface and measurement error. Discretization leads to discrete ill-posed problems characterized by a gradual decay in singular values. As the number of measurements increase, the number of singular values increase and more singular values approach zero. Singular values close to zero cause asymptotic solutions following inversion. On the other hand, measurement or round-off errors are represented by high frequency content and may cause A to be underdetermined. The lack of linear dependence is characterized by large gaps in the singular values. Well defined gaps represent conditions where one or more columns of the matrix A are nearly linearly combinations of other columns. If inversion is done without regularization, the gaps will cause instability in the solution.

Two typical types of regularization used in NAH are Truncation Singular Value Decomposition (TSVD) and Tikhonov Regularization (TR). TSVD is categorized as a sharp low pass filter with the filter f defined as

$$f_i = \begin{cases} 1, & \sigma_i \leq \text{cutoff} \\ 0, & \sigma_i > \text{cutoff} \end{cases} \quad (3.26)$$

Whereas, TR is a smooth low pass filter with f defined as

$$f_i = \frac{\sigma_i^2}{\sigma_i^2 + \beta} \quad (3.27)$$

where β is the filter parameter.

Essentially, TSVD truncates the singular value matrix by replacing a given number of values with zero, based on a threshold. On the other hand, TR increases attenuation with smaller singular values, thus allowing for increased wavenumber content to be reconstructed with respect to TSVD.

Both methods have pros and cons. TSVD does well in minimizing noise effects in reconstruction. However, undershooting the threshold of useable wavenumber content reduces

reconstruction resolution. Cutoff selection for high wavenumber content is often difficult since the singular values are small and vary little with increasing singular value number. TR allows for some level of the wavenumber energy neglected in TSVD to be used in reconstruction. Unfortunately, some level of unwanted wavenumber energy will also be reconstructed. Though the level of unwanted wavenumber content can be reduced by optimizing β , the possibility of over-smoothing lower wavenumber content exists.

One method of determining the cutoff or β value is Generalized Cross-Validation (GCV)⁶⁸. GCV seeks to optimize the regularization parameter *a priori* by removing data points one by one and computing each point from the remaining data set with the regularized transfer function. The regularization parameter is varied until the error of the computed data is minimized on average. Mathematically, GCV is represented as

$$G(\sigma) = \frac{\|Ax_\sigma - \tilde{b}\|_2^2}{\text{trace}(I_m - AA^\#)} \quad (3.28)$$

Where I_m is an m by m identity matrix and the numerator and denominator can be expressed as:

$$\|Ax_\sigma - \tilde{b}\|_2^2 = \sum_{i=1}^n \left((1 - f_i) u_i^* \tilde{b} \right)^2 + \|(I_m - UU^*)\tilde{b}\|_2^2 \quad (3.29)$$

$$\text{trace}(I_m - AA^\#) = m - \sum_i^n f_i \quad (3.30)$$

CHAPTER 4: NUMERICAL SIMULATIONS

In chapter four, the question of whether HELS is capable of performing more accurate reconstructions than expected by NAH resolution guidelines is explored through simulation. For the remainder of this dissertation, the term NAH resolution guidelines refers to both equation (3.10) and the spatial Nyquist sampling rate unless otherwise specified. The problem is formulated as two coherent point sources varying in separation distance, location, phase angle and frequency (note that for the remainder of the paper, acoustic frequency will be regarded as

frequency). Stand-off distance is tested at 5 and 15 mm. At 5 mm, NAH resolution guidelines are met and validation of the model and NAH algorithms are verified. Following validation of the model, the stand-off distance is increased to 15 mm and source parameters are varied. Planar Fourier Acoustics, HELS and Modified HELS are applied in the simulations. Justification for the choice of regularization and a method differentiating between ghost and real sources is given, followed by possible reasoning for improved reconstruction performance with Modified HELS.

The choice of point sources is based on the fact that many real world sources can be estimated as point sources. If the size of the source is relatively small with respect to the size of other sources in the system, point source approximation is valid. Examples of point sources are resistors or capacitors on computer motherboards, squeaking of control valves in automobile hydraulic systems, and mechanical relays located in many major home appliances. A few examples are shown in figure 4.1.

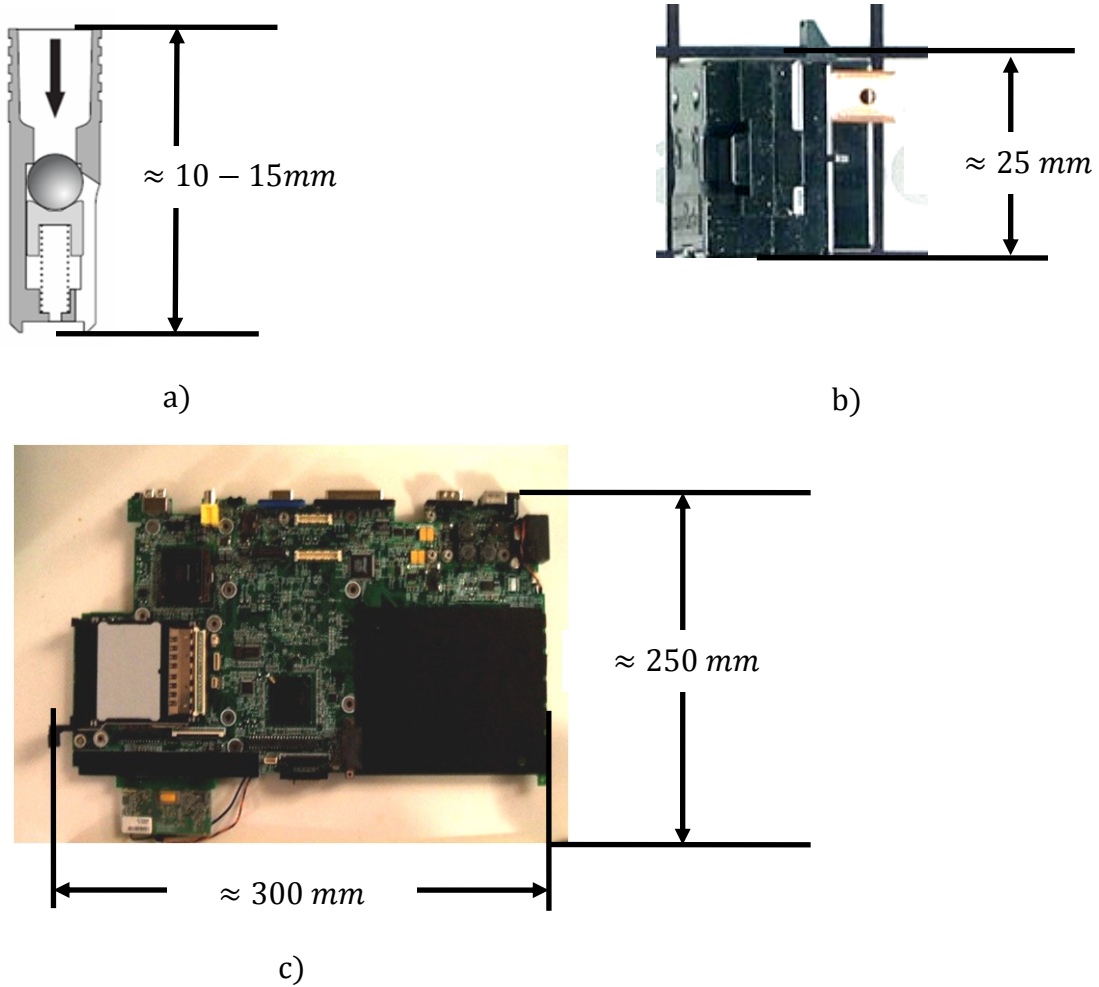


Figure 0.1: Real-world point-like source examples – a) hydraulic check valve common in hydraulic systems⁶⁹; b) refrigerator compressor relay⁷⁰; c) computer motherboard

Mathematical model

Our main focus is to demonstrate reconstruction of small components or subsystems, which normally produce acoustic radiation patterns that can be approximated by point sources. The pressure radiation of a point source in the absence of scattering objects can be described by Helmholtz's equation with boundary conditions specified by the Sommerfield radiation condition

$$\nabla^2 \hat{p} + k\hat{p} = 0, r > a \quad (4.1)$$

$$\lim_{r \rightarrow 0} \left(\frac{1}{r} \frac{\partial \hat{p}}{\partial r} - ik\hat{p} \right) = 0 \quad (4.2)$$

where a is the characteristic radius of a radiating source defined as the smallest sphere enclosing the source^{42, 71}.

The pressure radiation of point sources satisfies equations (4.1) and (4.2) everywhere except at the location of the source. As the distance from the source to the enclosing surface approaches zero, the idea of a point source is realized by the inhomogeneous equation

$$(\nabla^2 + k^2)\hat{p}_\varepsilon = -4\pi\hat{S}\delta(x-x_s)\delta(y-y_s)\delta(z-z_s) \quad (4.3)$$

where the δ is the Dirac delta function and the $\varepsilon \rightarrow 0$ represents the limiting case at the source location. The described conditions provide the following solution to equation (4.1)

$$\hat{p}_m = \hat{S} \frac{e^{i(kR_m + \phi)}}{R_m} \quad (4.4)$$

where \hat{p}_m is the noise-less data measured on the measurement hologram at distances R_m , \hat{S} is the monopole amplitude and ϕ is the phase angle.

In practice, background noise plays a significant role in reconstruction amplitude, resolution and location accuracy based on equation (3.10). Uniformly distributed, zero mean noise was introduced to \hat{S} , by δ using the Mersenne Twister algorithm⁷².

$$\hat{p}_m = (1 \pm \delta)\hat{S} \frac{e^{i(kR_m + \phi)}}{R_m} \quad (4.5)$$

Test setup

To test the resolution requirements of each method, two coherent point sources of various phase difference ϕ , and separation distance δ , are simulated. Source spacing and stand-off distances are selected to adhere and violate the NAH resolution guidelines to determine the validity of the requirements with respect to Planar Fourier Acoustics, HELS and Modified

HELs. δ is varied between 5 and 15 mm to simulate significant sources of acoustic radiation on surfaces similar to the examples given previously, while the phase is varied between 0 and π . Excitation frequencies are selected over a wide range to understand the relationship between excitation frequency reconstruction accuracy. Figure 4.2 illustrates the simulated problem

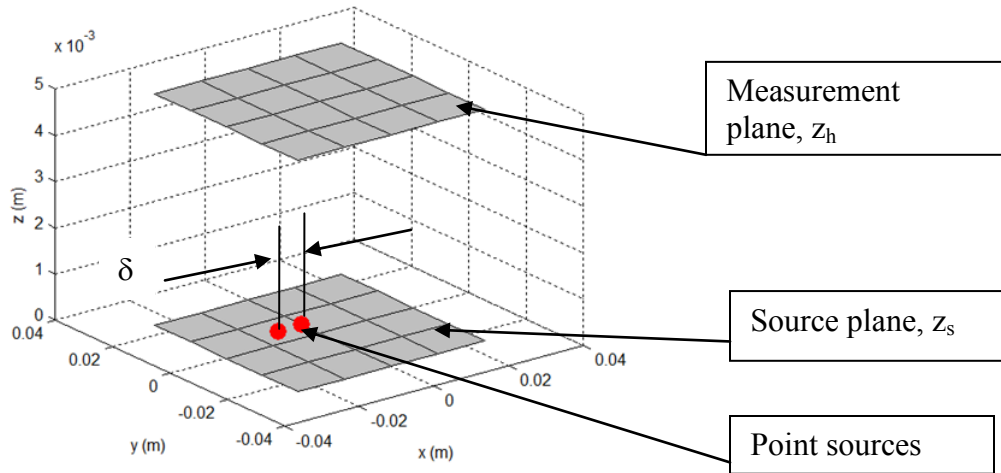


Figure 0.2: Measurement and source planes

Measurement and reconstruction surface size is based on δ . In Fourier Acoustics typical measurement aperture sizing has been prescribed by Williams to be at least four times the size of the actual source to limit edge effects during reconstruction⁵. On the other hand, HELs has shown to provide satisfactory results with much smaller aperture to reconstruction surface ratios⁴². To ensure a fair comparison between the two methods, the measurement aperture is chosen to be a 50x50 mm plane to satisfy the more conservative measurement requirements of Fourier Acoustics. A 5x5 measurement array is chosen to allow for testing across nodal lines of the surface while also ensuring a minimum of two measurement points between the source and the surface edge. The buffer of measurement points reduces edge effects in reconstruction.

The environment is simulated to be a free-field, thus acoustic intensity and pressure are proportional. In terms of HELS, pressure formulations are computationally easier than the velocity equation, since no spatial derivatives of the spherical harmonics are required. Therefore, pressure reconstruction is used instead of acoustic intensity in all solution methods.

In order to apply the HELS methods in reconstruction, a characteristic radius must be calculated. The characteristic radius is the smallest sphere enclosing an object. However, a point source has no physical dimensions and the typical definition of characteristic radius cannot be used. Instead, the characteristic radius of a plate is used, where the plate is defined as the measurement surface shown in figure 4.2.

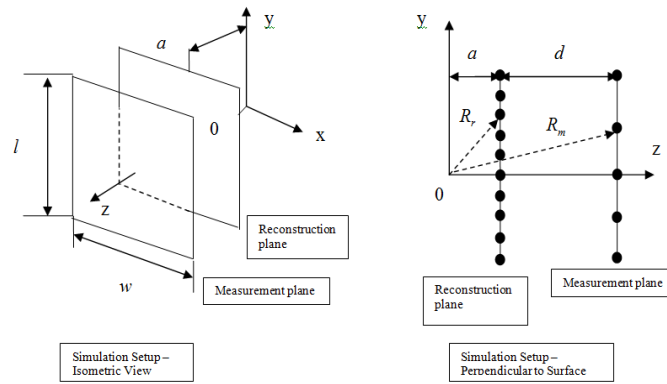


Figure 0.3: Theoretical plane characteristic dimension and reconstruction plane

The characteristic radius is defined as

$$a = \frac{\sqrt{l^2 + w^2}}{2} \quad (4.6)$$

where l and w are the length and width of the measurement plane, and the characteristic radius a is the distance from the theoretical origin to the center point of the reconstruction plane. R_r are the distances between the reconstruction points of interest and the theoretical origin deduced

from a . The measurement plane is defined by R_m at the standoff distance from the reconstruction plane.

$$\vec{R}_m = \vec{R}_r + \vec{d}$$

Source locations are selected to take advantage of the symmetry of the surfaces. All source locations are selected between measurement points except in the cases where the origin of the surfaces was selected. Figure 4.4 illustrates the locations scenarios for $\delta=10$ mm. Each scenario is identified by a number in the left hand corner of the surface, and sources are identified by black dots surrounded by white circles. The left and right sources are called the left-hand source (LHS) and right-hand source (RHS), respectively, throughout the paper.

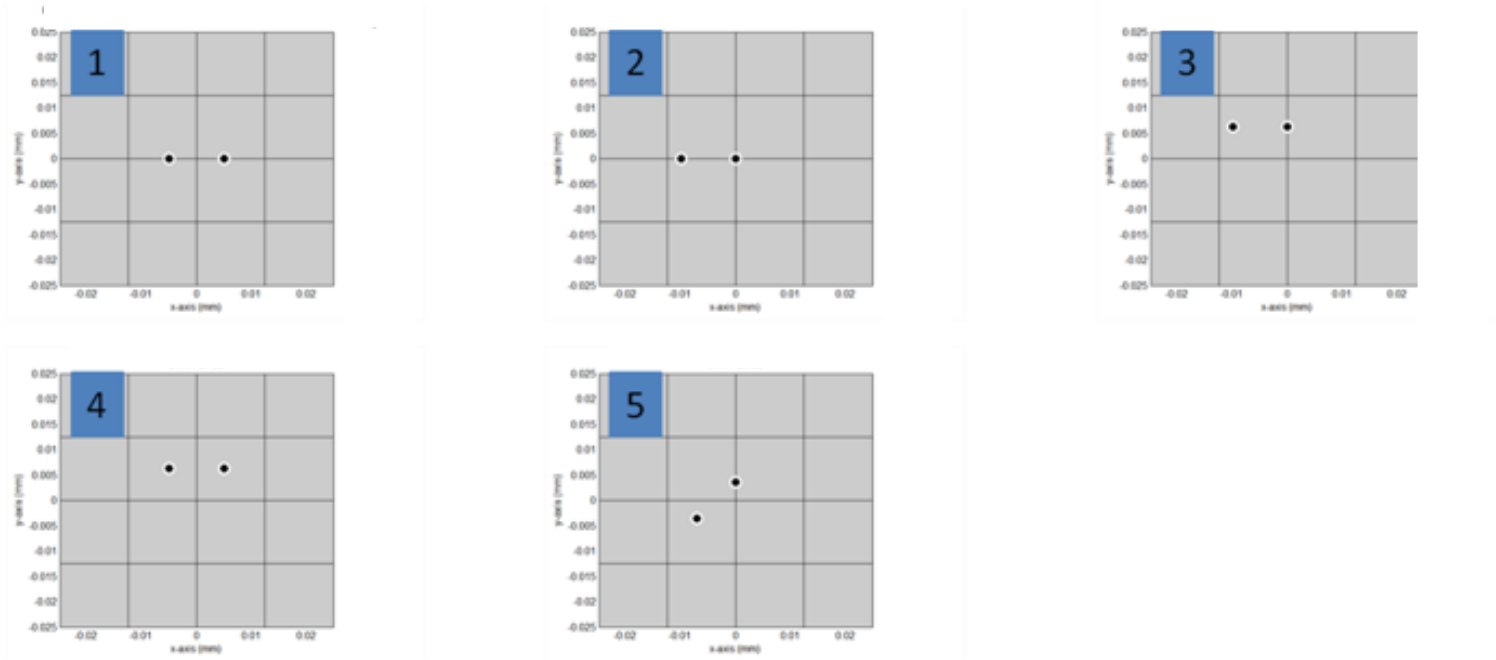


Figure 0.4: Source locations reconstructed in simulation for $\delta=10$ mm. Reconstruction scenarios are indicated by the number in left hand corner. Source locations are indicated by black dots surrounded by white circles.

Table 4.1 below summarizes the ranges used in simulation for each reconstruction scenario.

Table 4.1: Simulation parameter ranges

Parameter	Value
Source strength (Pa)	1
δ (mm)	5, 10, 15
d (mm)	5, 15
Acoustic excitation frequency (Hz)	100; 1,000; 5,000; 10,000; 12,000-20,000 in 1,000 Hz increments
Relative phase between sources, ϕ (radians)	$0, \frac{\pi}{2}, \pi$
SNR (dB)	10

Simulation results

The following section summarizes the simulation results of HELS and Planar Fourier Acoustics in reconstruction of two coherent point sources when NAH resolution guidelines are met and violated. Tables 4.2 and 4.3 summarize the required Nyquist sampling rate and NAH spatial resolution guideline (based on equation (3.10) only) for the test combinations outlined in table 4.1. For example, at an SNR of 10 dB and stand-off distance of 5 mm, Planar Fourier Acoustics should be able to distinguish sources separated by 13.64 mm or more if the measurement spacing meets the Nyquist sampling requirement.

Table 4.2: Spatial Nyquist sampling rate

δ (mm)	Required measurement spacing according to Nyquist sampling rate (mm)
5	2.5
10	5
15	7.5

Table 4.3: NAH spatial resolution guideline based on equation 3.10 only

d (mm)	SNR (dB)	NAH resolution guideline (mm)
5	10	13.64
15	10	40.93

As stated in Ch. 3.3, HELS has the advantage of synthesizing points in between the measurement points. Therefore, the Nyquist sampling rate does not have to be satisfied to accurately reconstruct source locations properly. On the other hand, Fourier Acoustics is based on the DFT which requires sampling at the Nyquist rate as a minimum. Due to the constraints of the DFT, Fourier Acoustics measurement and reconstruction planes are sampled at 12.5 and 2.5 mm resolution. 12.5 mm matches the measurement spacing used with HELS, while 2.5 mm was chosen to satisfy the minimum Nyquist rate when $\delta=5$ mm.

Analysis starts with validation of the model and NAH algorithms. Validation is done by simulating scenarios that are expected to reconstruct correctly with respect to the NAH resolution guidelines. Following validation, parameters are varied to compare the reconstruction accuracy of Fourier Acoustics and HELS while in violation of the Nyquist NAH resolution guidelines.

Validation of model and algorithms

Based on the parameter values used in simulation, reconstruction should be feasible if the two sources are out of phase by π radians, with an SNR of 10 dB, a stand-off distance of 5 mm and $\delta=15$ mm. Justification for the stated stand-off distance and SNR are based on equation (3.10). Since the expectation is that reconstruction should be possible in this scenario, only source location 1 and min/max acoustic frequencies are analyzed for brevity. Source location 1 is used based purely on symmetry of the problem.

The reconstructed pressure is presented in linear scale with the pressures normalized by the peak reconstructed pressure to better visualize the peak reconstructed locations. The color scale of each surface may differ to aid in visualization of the peaks. Actual source locations are

indicated by large dots on the surface, while reconstruction locations are represented by surface nodal points. In the case of the HELS methods, the measurement locations are represented by X's. Fourier Acoustic measurement points match the nodal points of the surfaces.

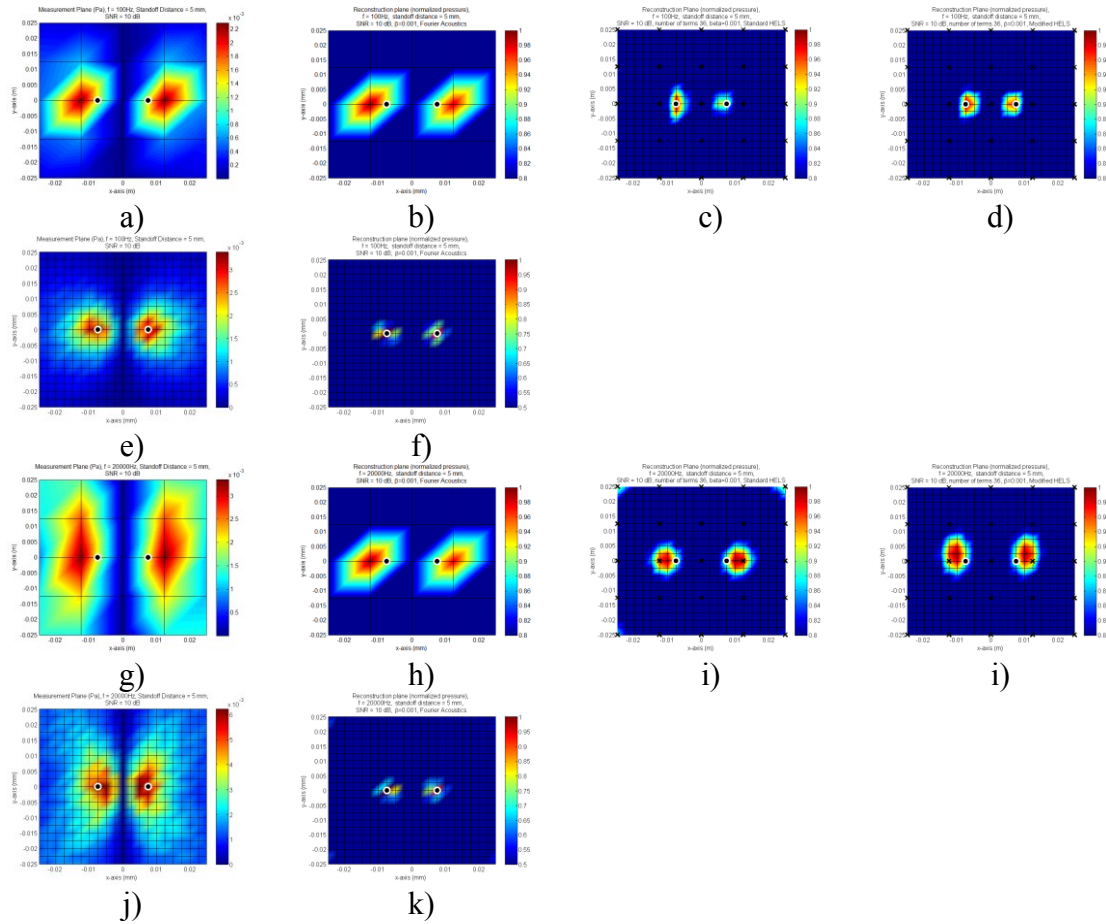


Figure 0.5: a) Measurement plane with 12.5 mm spacing, $\delta=15\text{ mm}$, $d=5\text{ mm}$, $\phi=\pi$ radians, $f=100\text{Hz}$; b) Fourier Acoustics reconstruction surface with 12.5 mm measurement spacing; c) Standard HELS reconstruction surface; d) Modified HELS reconstruction surface; e) Measurement surface plane with 2.5 mm spacing; f) Fourier Acoustics reconstruction surface with 2.5 mm measurement spacing; g) Measurement plane with 12.5 mm spacing, $\delta=15\text{ mm}$, $d=5\text{ mm}$, $\phi=\pi$ radians, $f=20\text{kHz}$; h) Fourier Acoustics reconstruction surface with 12.5 mm measurement spacing; i) Standard HELS reconstruction surface; j) Modified HELS reconstruction surface; k) Fourier Acoustics reconstruction surface with 2.5 mm measurement spacing

Figure 4.5 shows that with a measurement spacing of 12.5 mm Fourier Acoustics is able to distinguish the two sources, however, the reconstructed locations are not accurate. In fact, the reconstruction is not significantly better than the measurement surface image. Though the Nyquist sampling rate is satisfied, possible reconstruction locations are limited by the measurement surface as discussed in Ch. 3.2. Once the measurement spacing is refined, Fourier Acoustics reconstructs the source locations exactly. On the other hand, HELS and Modified HELS are able to reconstruct the sources accurately with measurement spacing of 12.5 mm as a consequence of HELS ability to synthesize field locations. More accurate reconstruction is possible if the number of measurement points is increased.

Based on the results above, simulations are conducted with phase angles of $\frac{\pi}{2}$ and 0 radians. Since Fourier Acoustics with 12.5 mm spacing did not produce satisfactory results previously, results are omitted from the remaining summaries. At $\phi = \frac{\pi}{2}$ (figure 4.6), both HELS methods and Fourier Acoustics are able to reconstruct the sources accurately. Similarly to $\phi = \pi$, Fourier Acoustics provides more accurate reconstruction locations. When ϕ is reduced to 0 (figure 4.7), all methods are able to reconstruct at 20 kHz. However, at 100 Hz, only Fourier Acoustics reconstructs the sources accurately.

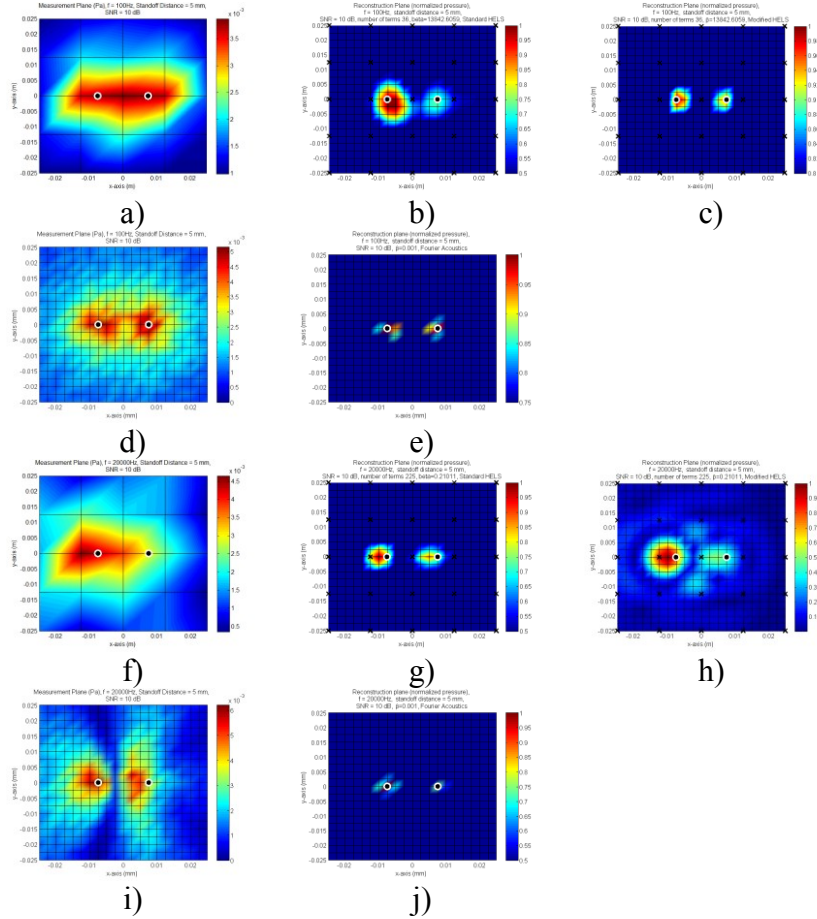


Figure 0.6: a) Measurement plane with 12.5 mm spacing, $\delta=15$ mm, $d=5$ mm, $\phi=\frac{\pi}{2}$ radians, $f=100$ Hz; b) Standard HELS reconstruction surface; c) Modified HELS reconstruction surface; d) Measurement surface plane with 2.5 mm spacing; e) Fourier Acoustics reconstruction surface with 2.5 mm measurement spacing; f) Measurement plane with 15 mm spacing, $\delta=10$ mm, $d=5$ mm, $\phi=\frac{\pi}{2}$ radians, $f=20$ kHz; g) Standard HELS reconstruction surface; h) Modified HELS reconstruction surface; i) Measurement surface plane with 2.5 mm spacing; j) Fourier Acoustics reconstruction surface with 2.5 mm measurement spacing

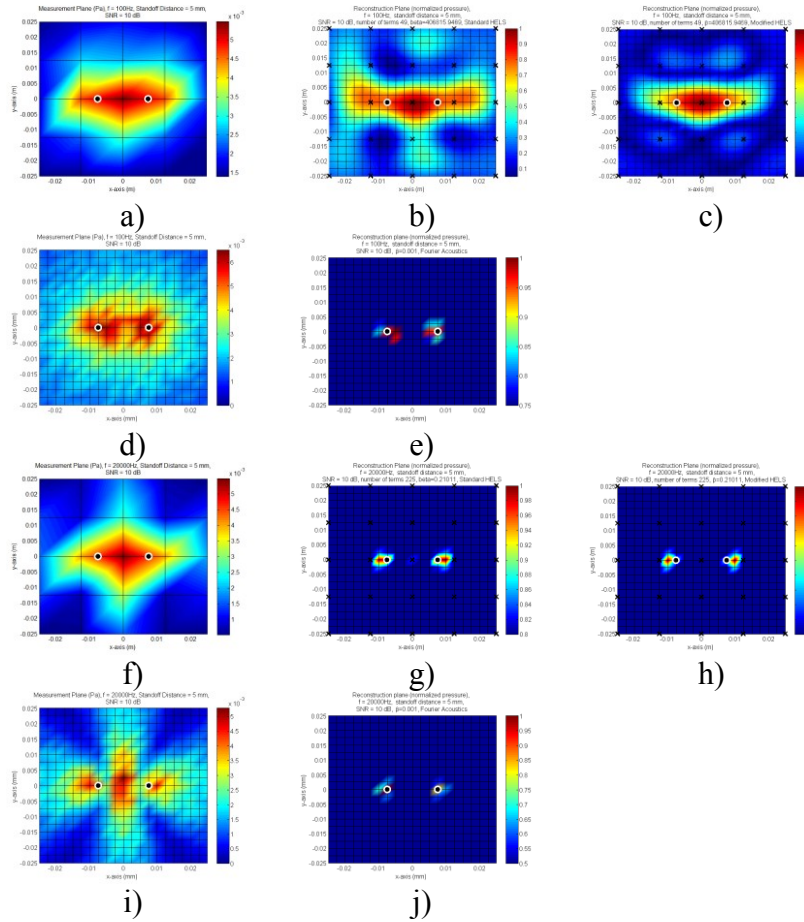


Figure 0.7: a) Measurement plane with 12.5 mm spacing, $\delta=15$ mm, $d=5$ mm, $\phi=0$ radians, $f=100$ Hz; b) Standard HELS reconstruction surface; c) Modified HELS reconstruction surface; d) Measurement surface plane with 2.5 mm spacing; e) Fourier Acoustics reconstruction surface with 2.5 mm measurement spacing; f) Measurement plane with 12.5 mm spacing, $\delta=15$ mm, $d=5$ mm, $\phi=0$ radians, $f=20$ kHz; g) Standard HELS reconstruction surface; h) Modified HELS reconstruction surface; i) Measurement surface plane with 2.5 mm spacing; j) Fourier Acoustics reconstruction surface with 2.5 mm measurement spacing

The HELS methods presented use significantly coarser surfaces than with Fourier Acoustics. If the measurement resolution is refined, reconstruction is possible with HELS. Figure 4.8 shows that at a measurement spacing of 5 mm, the HELS methods are able to reconstruct with similar accuracy to Fourier Acoustics with 2.5 mm spacing. Further improvement in reconstruction resolution is expected if the measurement resolution was increased to that of the Fourier Acoustic measurements. However, the objective of this

investigation is not to match the resolution of Fourier Acoustics. Instead, it is to determine if HELS is able to reconstruct sources in violation of the NAH guidelines outlined by Williams. Therefore, HELS simulations will return to the 5x5 measurement array when simulating sources in violation of the NAH resolution guidelines.

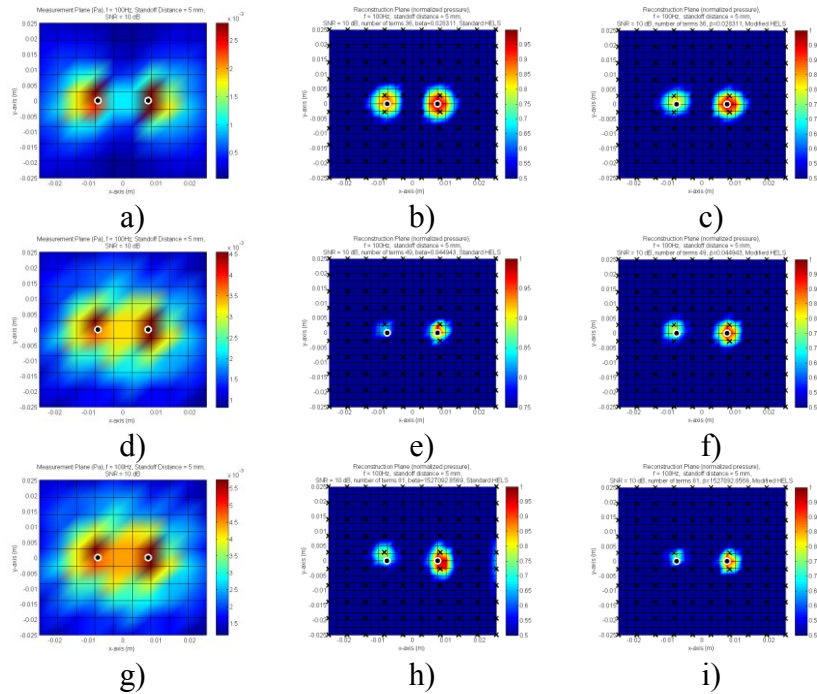


Figure 0.8: a) Measurement plane with 5 mm spacing, $\delta=15$ mm, $d=5$ mm, $\phi=\pi$ radians, $f=100$ Hz; b) Standard HELS reconstruction surface; c) Modified HELS reconstruction surface; d) Measurement plane with 5 mm spacing, $\delta=15$ mm, $d=5$ mm, $\phi=\frac{\pi}{2}$ radians, $f=100$ Hz; e) Standard HELS reconstruction surface; f) Modified HELS reconstruction surface; g) Measurement plane with 5 mm spacing, $\delta=15$ mm, $d=5$ mm, $\phi=\frac{\pi}{2}$ radians, $f=100$ Hz; h) Standard HELS reconstruction surface; i) Modified HELS reconstruction surface;

Based on the above results, proper reconstruction of each method is feasible when the NAH guidelines are met. However, inaccurate reconstructions were produced with the HELS methods at low frequency, a phase angle of zero, and coarse measurement spacing. The inaccurate reconstruction is not a consequence of violating the NAH resolution guidelines or the HELS method itself. Since the accuracy improved greatly when the measurement resolution was

reduced to twice that of the Fourier Acoustic surfaces, it is likely that the results are due to the problem being significantly underdetermined, and consequently ill-conditioned⁷³.

Reconstruction accuracy when violating NAH resolution guidelines

Due to the number of combinations created from the range of parameters, the following section begins by summarizing the results of each set of parameters simulated. Following the summaries, relative error plots are provided for each set of parameters at each location scenario. At the beginning of each summary, the correlating figure numbers are listed for reference. Where appropriate, reconstruction surfaces that add value to the investigation are provided.

The relative error is based on the distance between the source location and the reconstructed location compared to the spacing of the 12.5 mm measurement array. The 12.5 mm microphone spacing is chosen since it gives a sense of HELS' ability to refine spatial resolution from coarse measurements. Though the Fourier Acoustics' measurement spacing is at finer resolution, the choice of HELS measurement spacing indicates the advantages of using the HELS method in reconstruction. If two sources are not distinguishable in reconstruction or accurate source locations are not recognizable, the relative error is listed as 100% since no advantage is gained over taking a measurement surface at very close stand-off distances. In some cases, reconstruction may be worse.

$$error\% = \frac{\sqrt{(x_{actual} - x_{reconstructed})^2 + (y_{actual} - y_{reconstructed})^2}}{0.0125} * 100\% \quad (4.7)$$

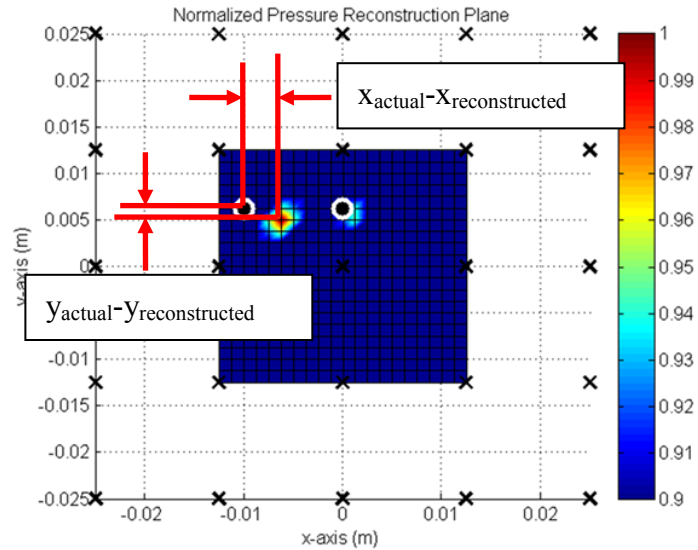


Figure 0.9: Illustration of location error calculation

In order to meet the spatial sampling requirement and mitigate aliasing effects, the 10 and 5 mm source separation simulations require finer resolution in reconstruction. In the case of HELS, the measurement spacing is kept at 12.5 mm and the reconstruction resolution is reduced from 2.5 mm to 1.25 mm. Since HELS is able to synthesize any field point, the choice of reconstruction surface is refined by reconstructing the inner 50% of the surface with the same number of reconstruction points. Given that the same number of reconstruction points is used, the reconstruction resolution is refined while not increasing measurement and computation time. To provide an equivalent resolution, Fourier Acoustics' reconstructions are provided at 1.25 mm spacing, in addition to the previous reconstruction resolution of 2.5 mm. Error analysis of Fourier Acoustics surfaces are done only on the “zoomed-in” area used with HELS. $\delta=15$ mm analysis was done at reconstruction resolution of 2.5 mm, with the original reconstruction surface, since LHS sources of locations two and three are located close to the edge of the 50% surface.

In order to have a sense of the relative error calculation, HELS, Modified HELS and the 2.5 mm Fourier Acoustic reconstructions, are shown for source location four with $\delta=10$ mm, $\phi=\frac{\pi}{2}$, and frequencies of 12 kHz (figure 4.10). The top 50% of the peak amplitude is shown to better understand the error between the actual and reconstructed sources. Stars are located on the surfaces to indicate peak reconstruction locations. Note that in the case of Standard HELS and Fourier Acoustics, two sources are not distinguishable on the reconstruction surface. Therefore, their relative error in reconstruction was deemed as 100%. The relative error level for Modified HELS reconstruction is 21% in the case of both sources.

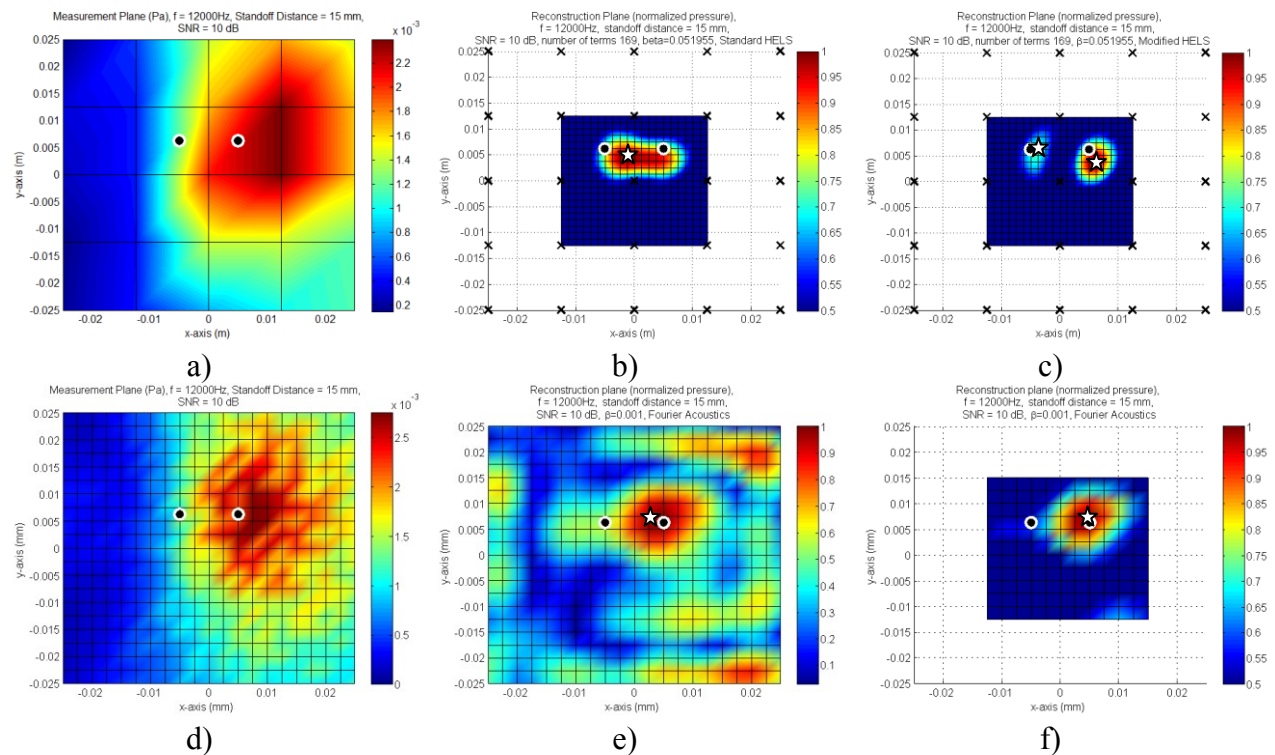


Figure 0.10: a) Measurement surface with 12.5 mm spacing, $\delta=10$ mm, $d=15$ mm, $\phi=\frac{\pi}{2}$ radians, $f=12$ kHz; b) Standard HELS reconstruction surface with 1.25 mm spacing; c) Modified HELS reconstruction surface with 1.25 mm spacing; d) Measurement surface with 2.5 mm spacing, $\delta=10$ mm, $d=15$ mm, $\phi=\frac{\pi}{2}$ radians, $f=12$ kHz; e) Fourier Acoustics reconstruction surface with 2.5 mm spacing; f) Fourier Acoustics reconstruction surface with 2.5 mm measurement spacing (inner 50% of surface)

1.1.1.1 Reconstruction with $\delta=15$ mm, $d=15$ mm, $\phi=\pi$ radians (Figures 4.15, 4.16)

At a stand-off of 5 mm and at location scenario four, HELS and Fourier Acoustic reconstructions were excellent. Based on the NAH resolution guidelines, we expect reconstruction accuracy to decrease significantly with the stand-off distance increased to 15 mm. According to the NAH resolution guidelines, the spatial resolution at 15 mm with an SNR of 10 dB should not be finer than 40.93 mm.

Figures 4.15 and 4.16 indicate that the NAH resolution guidelines do not match well with simulation results, particularly at high frequency. Both HELS (Standard and Modified) and Fourier Acoustics reconstructed the source locations accurately for frequencies of 10 kHz and above. At 5 kHz and below, Fourier Acoustics had difficulties reconstructing source locations accurately in some of the cases. Both HELS methods are able to accurately reconstruct the source locations in each of the location scenarios and at all tested frequencies. No significant difference between HELS methods is identifiable.

Possible root causes for accurate reconstruction may be the type of source modeled and phase angle considerations. The resolution guidelines are based on the angular spectrum, which is essentially a two dimensional Fourier Transform of the measured pressures. In the case of Planar Fourier Acoustics, the guidelines assume that the shape of the plate will composed of sinusoidal functions. In the case of point sources, the shape of the wave still contains oscillatory characteristics. However, the shape of the waveform is concentrated rather than distributed across the surface. Though the SNR may be low point to point, the overall SNR can be quite high since the areas surrounding the sources have relatively low energy (pressure) concentration. Consequently, the angular spectrum is not significantly affected by the added noise and the

sources can be reconstructed accurately in most cases (figure 4.11). The use of a point source may also justify the reduction in accuracy with decreasing frequency, due to more significant spherical spreading with decreasing frequency. Further comments on spherical spreading are discussed in chapter 4.6. The provided reasoning applies to all remaining simulations since all parameters provide scenarios in violation of the NAH resolution guidelines.

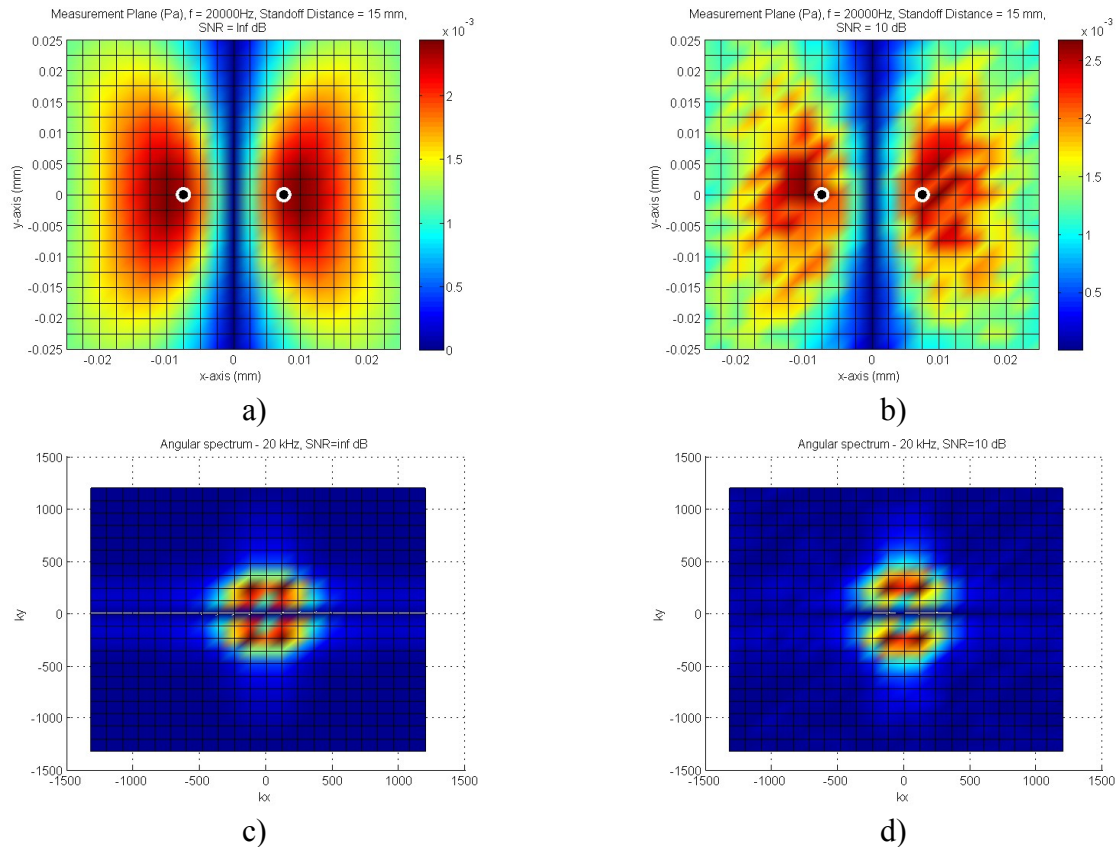


Figure 0.11: a) Measurement surface with 12.5 mm spacing, $\delta=10$ mm, $d=15$ mm, $\phi=\pi$ radians, $f=20$ kHz, $\text{SNR}=\infty$ dB; b) Measurement surface with 12.5 mm spacing, $\delta=10$ mm, $d=15$ mm, $\phi=\pi$ radians, $f=20$ kHz, $\text{SNR}=10$ dB; c) Angular spectrum at $\text{SNR}=\infty$ dB; d) Angular spectrum at $\text{SNR}=10$ dB

The phase of the point sources also plays a role in reconstruction accuracy. As stated, the angular spectrum is a two dimensional Fourier Transform of the measurement surface, where the wavenumbers are related to the wavelength of the in-plane oscillation by $k = \sqrt{k_x^2 + k_y^2}$. Two

sources separated by 15 mm, with a relative phase of π , equates to a wavelength of 30 mm in terms of a sinusoidal wave. Even when considering the distance between sources based on “sinusoidal wavelength”, the source separation remains smaller than the resolution provided by the NAH resolution guidelines. In combination with the increased SNR due to the use of point sources, the increased resolution capability seems reasonable. However, based on results at lower frequencies, there may be possibility of improved resolution with HELS methodologies worth considering with respect to Fourier Acoustics.

1.1.1.2 Reconstruction with $\delta=15$ mm, $d=15$ mm, $\phi=\frac{\pi}{2}$ radians (Figures 4.17, 4.18)

Decreasing the phase to $\phi=\frac{\pi}{2}$ significantly reduced accuracy at acoustic frequencies below 10 kHz. Above 10 kHz, no significant difference in accuracy was noted between HELS, Modified HELS and Fourier Acoustics.

1.1.1.3 Reconstruction with $\delta=15$ mm, $d=15$ mm, $\phi=0$ radians (Figures 4.19, 4.20)

Similar to $\phi=\frac{\pi}{2}$, results below 10 kHz are poor and are omitted from the results. Above 10 kHz, results vary based on location scenario. For example, Modified HELS is not able to accurately reconstruct two sources in the case of location scenario two. On the other hand, at location scenario four, Modified HELS shows a significant increase in capable frequency range. Similar statements can be made for both Standard HELS and Fourier Acoustics at other combinations of locations and frequencies. Based on the inconsistencies, none of the methods are considered reliable at the given parameters.

1.1.1.4 Reconstruction with $\delta=10$ mm, $d=15$ mm, $\phi=\pi$ radians (Figures 4.21, 4.22)

As was the case at $\delta=15$ mm, reconstruction with the HELS methods are more accurate than Fourier Acoustics, particularly below 12 kHz (no significant difference between HELS methods). However, the relationship of decreased accuracy with decreasing frequency appears in both HELS methods as well as Fourier Acoustics. Since the only parameter held constant between the two variants of tests at $\phi=\pi$ thus far is stand-off distance, one may hypothesize that the stand-off distance plays a role in the decreasing accuracy.

Fourier Acoustics at 1.25 mm did not show increased resolution over the 2.5 mm variant. In many cases, reconstruction accuracy is worse. The unsatisfactory reconstruction accuracy is a result of increased ill-conditioning due to the increased number of measurement points. In many cases, an optimal β value could not be determined which produced high resolution reconstruction without over-smoothing the surface to the point where the two sources were indistinguishable. Discussion of regularization issues with Fourier Acoustics are discussed in chapter 4.5.

1.1.1.5 Reconstruction with $\delta=10$ mm, $d=15$ mm, $\phi=\frac{\pi}{2}$ radians (Figures 4.23, 4.24)

The trend of decreasing reconstruction accuracy with decreasing frequency is more prominent at $\phi=\frac{\pi}{2}$ radians and $\delta=10$ mm. Reduction in reconstruction accuracy is due to additional interference between the two source wavefronts in comparison to $\phi=\pi$ and $\delta=15$ mm. Similar to the previous cases, reconstruction accuracy of both HELS methods decreased significantly for frequencies below 12 kHz. Fourier Acoustics saw an increase in the minimum capable frequency to approximately 14 kHz. Therefore, all plots are limited to frequencies greater than or equal to 10 kHz.

Analysis of the 1.25 mm Fourier Acoustic reconstructions shows inconsistent reconstruction accuracy, similar to the $\phi=\pi$ case. Comparison of 2.5 mm Fourier Acoustic reconstructions with HELS and Modified HELS also showed similar trends to the $\phi=\pi$ case. Specifically, as frequency decreases, the two HELS methodologies tend to produce more accurate reconstruction locations than Fourier Acoustics. However, both HELS and Modified HELS have issues at particular frequencies depending on the source locations. Table 4.4 summarizes the poor reconstruction scenarios. Fourier Acoustics reconstruction with 1.25 mm spacing was not included due to inconsistencies in reconstruction.

Table 4.4: Frequencies of poor reconstruction for HELS, Modified HELS, Fourier Acoustics at 2.5 mm spacing for $\delta=10$ mm, $d=15$ mm, $\phi=\frac{\pi}{2}$ radians.

Source location scenario	HELS	Modified HELS	Fourier Acoustics 2.5 mm spacing
1	<10 ,12-14 kHz	<12 kHz	≤ 14 kHz
2	≤ 12 kHz	<12, 17 kHz	≤ 15 kHz
3	<12 kHz	<12 kHz	≤ 17 kHz
4	≤ 17 kHz	<12 kHz	≤ 14 kHz
5	<10 kHz	<10, 16 kHz	≤ 14 kHz

The cases shown in figure 4.12 are indicative of the issues seen following reconstruction. Unlike the difficulties in reconstruction seen with Fourier Acoustics at 1.25 mm, even when the two sources are not identified properly, a sense of their location can be seen by the other three methods. Note that the examples in figure 4.12 are listed as 100% error because two distinguishable sources cannot be identified.

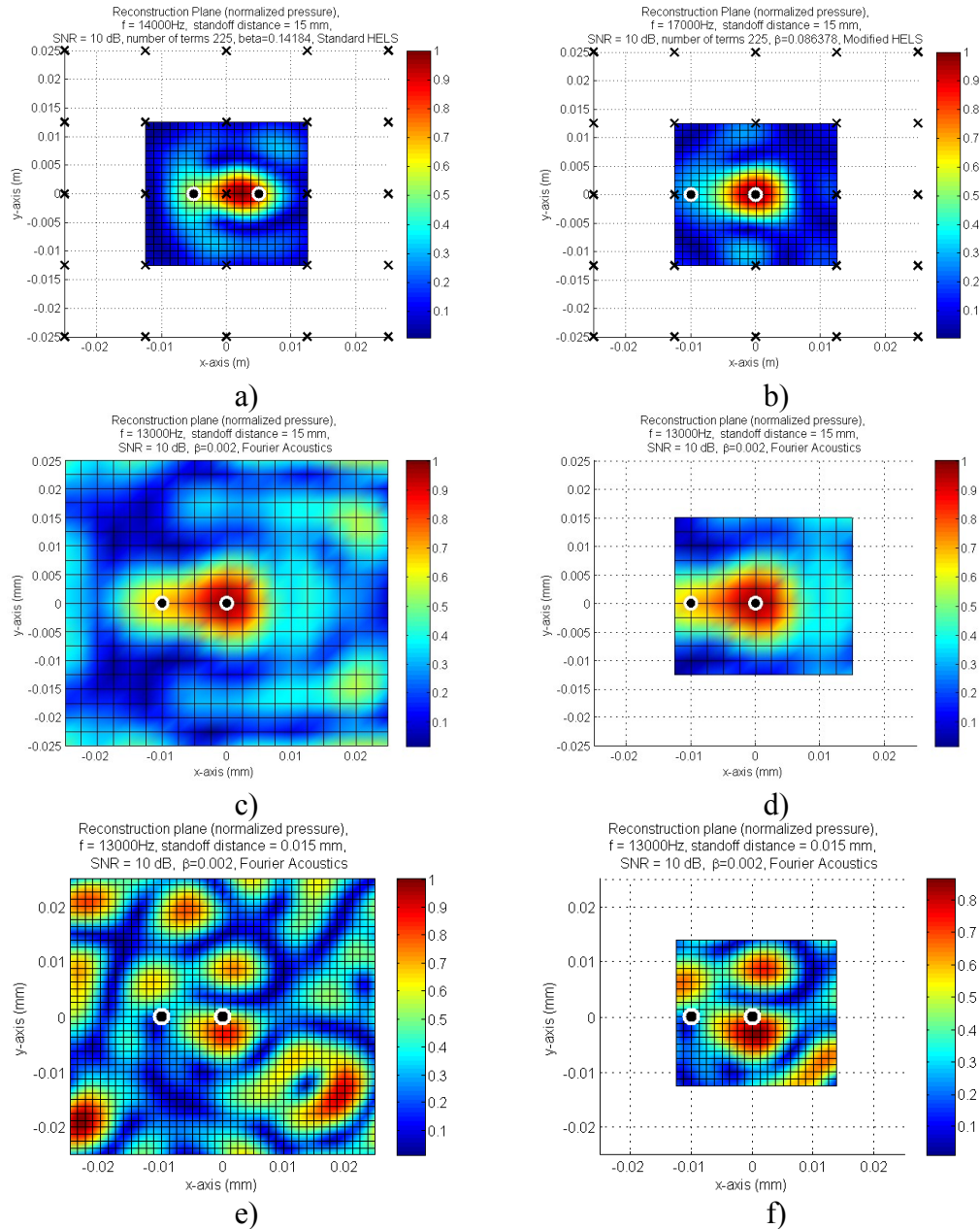


Figure 0.12: Examples of reconstructions not producing two distinguishable sources with $\delta=10$ mm, $d=15$ mm, $\phi=\frac{\pi}{2}$ radians: a) Standard HELS, location 1 at 14 kHz; b) Modified HELS, location 2 at 17 kHz; c) Fourier Acoustics reconstruction at 2.5 mm spacing, location 2 at 13 kHz; d) Fourier Acoustics reconstruction at 2.5 mm spacing, location 2 at 13 kHz (zoomed-in); e) Fourier Acoustics reconstruction at 1.25 mm spacing, location 2 at 13 kHz; f) Fourier Acoustics reconstruction at 1.25 mm spacing, location 2 at 13 kHz (zoomed-in);

Comparison of the HELS methodologies indicates Modified HELS shows significant improvement in reconstruction accuracy below 15 kHz. In particular, the advantage is apparent in source location scenarios two and three. The root cause of the decrease in accuracy for Standard HELS is likely due to the LHS source being lower in pressure magnitude than the RHS source. The reduced magnitude is a result of relative phase angle. Though the measurement surfaces in Modified HELS are identical to those of standard HELS, Modified HELS weights the input to the HELS algorithm based on the highest pressure peak. Thus, the measurement point magnitudes closest to the LHS source will be amplified as long as the magnitudes are relatively higher than the measurements surrounding the local points. Further insight into the justification is given in chapter 4.6.

1.1.1.6 Reconstruction with $\delta=10$ mm, $d=15$ mm, $\phi=0$ radians

None of the methods reconstruct the sources accurately. As the phase angle is decreased to zero, two sources cannot be distinguished at the stand-off distance tested. Figure 4.13 provides plots of the both HELS methods and Fourier Acoustics at 2.5 mm spacing for source location scenario four at 19 kHz. Fourier Acoustics at 1.25 mm spacing is not shown based on poor reconstruction results at $\phi=\frac{\pi}{2}$. 19 kHz was chosen as an example based on the satisfactory accuracy of each method at the given location with $\phi=\frac{\pi}{2}$.

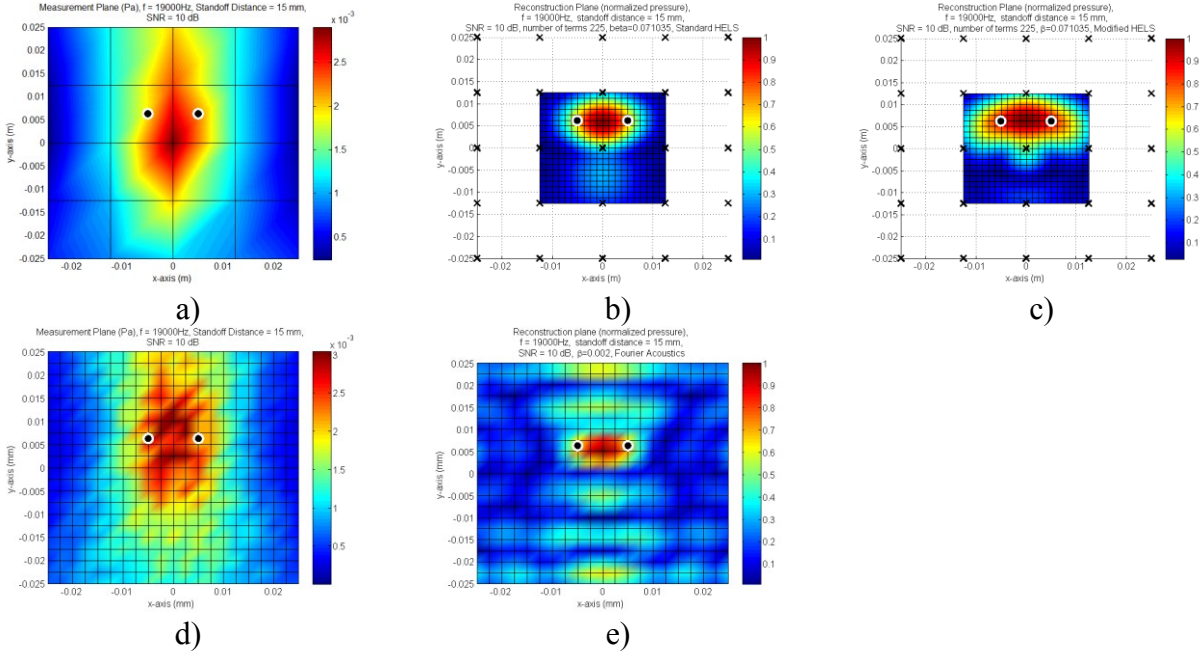


Figure 0.13: Reconstruction at 19 kHz with $\delta=10$ mm, $d=15$ mm, $\phi=0$ radians - a) 12.5 mm spacing measurement surface b) Standard HELS; c) Modified HELS; d) 2.5 mm spacing measurement surface e) Fourier Acoustics at 2.5 mm spacing

1.1.1.7 Reconstruction with $\delta=5$ mm, $d=15$ mm, $\phi=\pi$ radians (Figures 4.25, 4.26)

Results are similar to $\delta=10$ mm, $d=15$ mm, $\phi=\pi$ radians, but with a reduction in accuracy due to the reduction in source spacing. Both HELS methods produced more accurate results than Fourier Acoustics. Fourier Acoustics reconstructions at 1.25 mm are omitted due to inconsistent and poor reconstruction accuracy. Overall, no significant differences between the HELS methods occur.

1.1.1.8 Reconstruction with $\delta=5$ mm, $d=15$ mm, $\phi=\frac{\pi}{2}$ radians

No accurate reconstructions consistently occurred in any of the methods. The term “consistency” refers to shifting the measurement surface and reconstructing to the original reconstruction locations. Shifting the surface is used to determine the difference between actual

sources and ghost sources. A discussion of the procedure is provided in chapter 4.4. An example of false reconstruction is shown in figure 4.14.

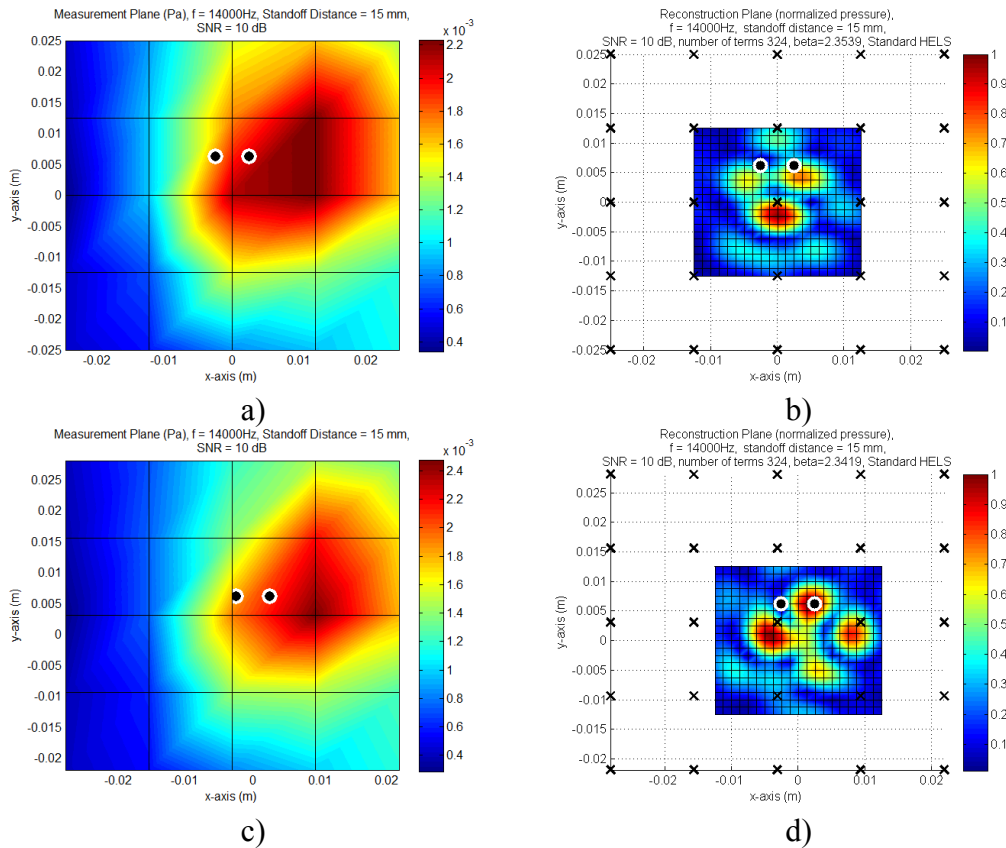


Figure 0.14: Determination of false sources – a) original measurement surface; b) original reconstructions surface with reconstructed sources near actual locations and an assumed false source at origin; c) shifted measurement surface; d) reconstruction of shifted measurement surface illustrating source reconstruction was not consistent following measurement shift

1.1.1.9 Reconstruction with $\delta=5$ mm, $d=15$ mm, $\phi=0$ radians

Similar to the case at $\delta=10$ mm, none of the methods reconstructed the sources accurately.

1.1.1.10 Relative error plots

Reconstruction with $\delta=15$ mm, $d=15$ mm, $\phi=\pi$ radians

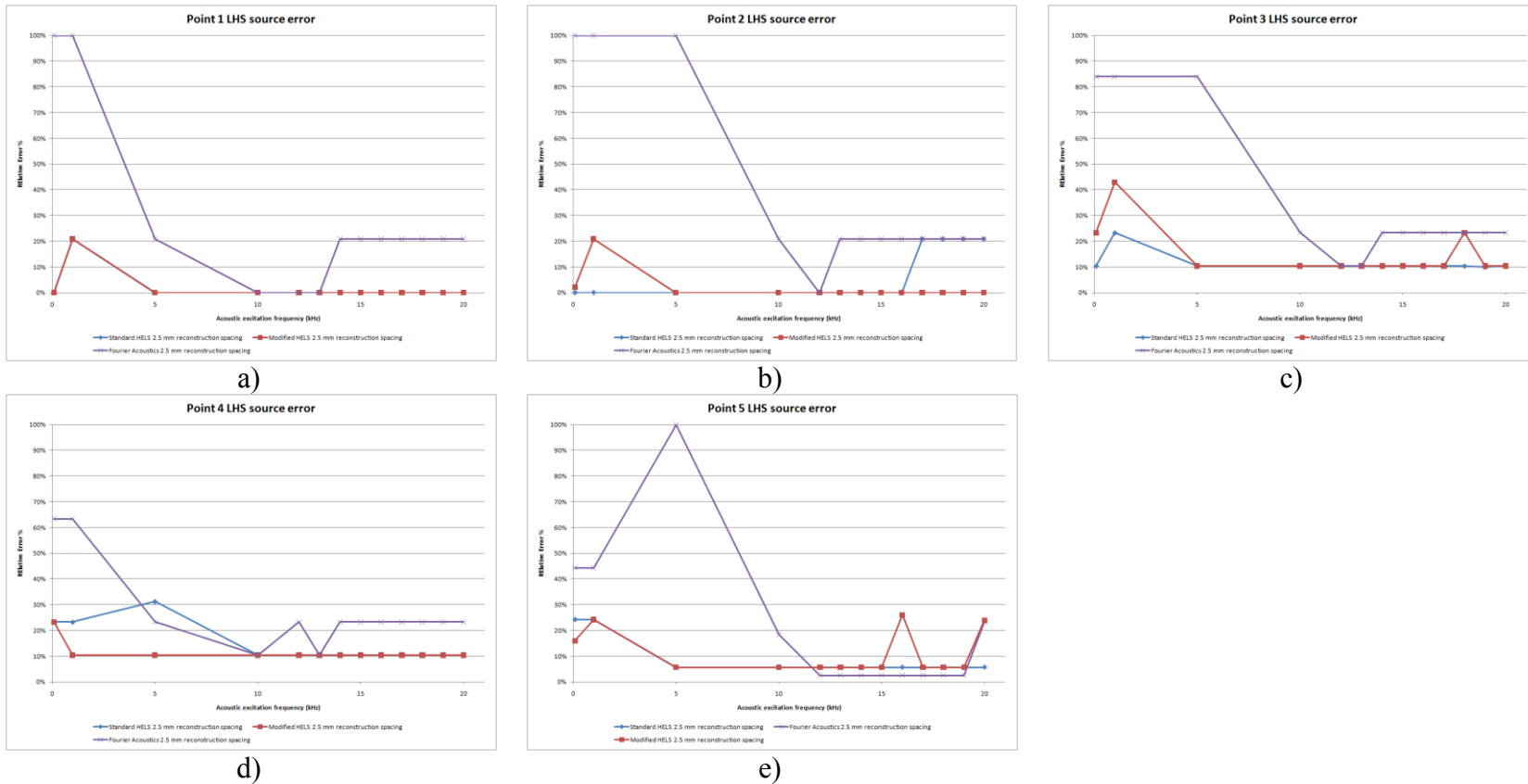
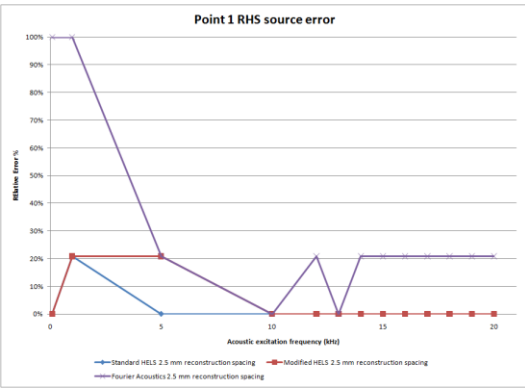
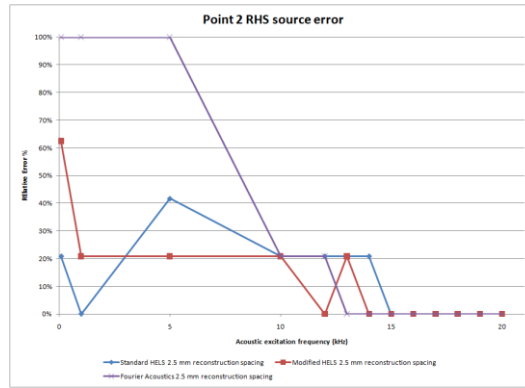


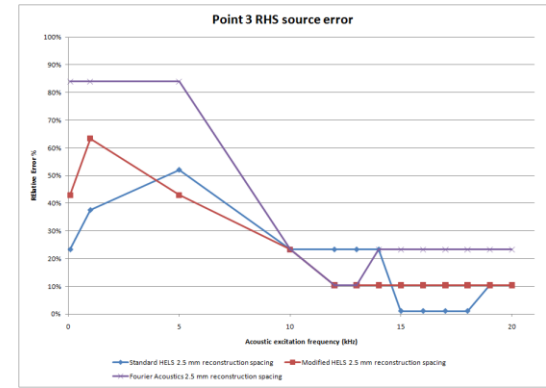
Figure 0.15: Relative error analysis of LHS source for $\delta=15$ mm, $d=15$ mm, $\phi=\pi$ radians – a) location 1; b) location 2; c) location 3; d) location 4; e) location 5



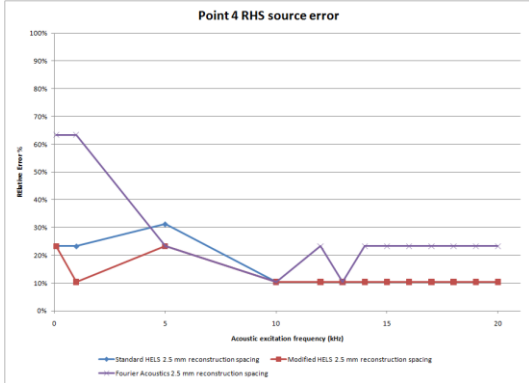
a)



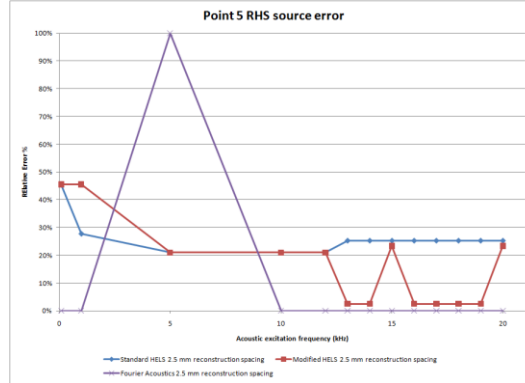
b)



c)



d)



e)

Figure 0.16: Relative error analysis of RHS source for $\delta=15$ mm, $d=15$ mm, $\phi=\pi$ radians – a) location 1; b) location 2; c) location 3; d) location 4; e) location 5

Reconstruction with $\delta=15$ mm, $d=15$ mm, $\phi=\frac{\pi}{2}$ radians

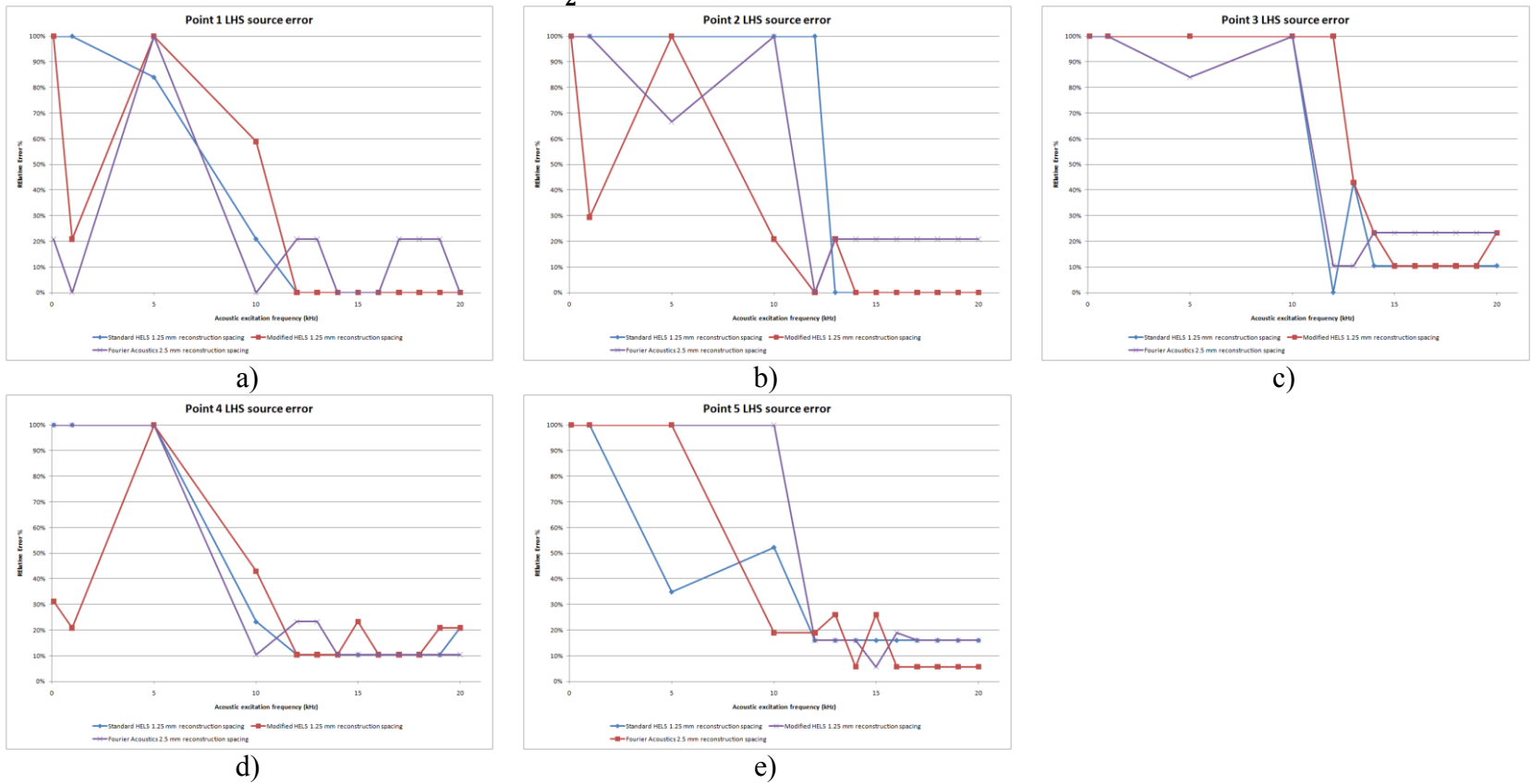
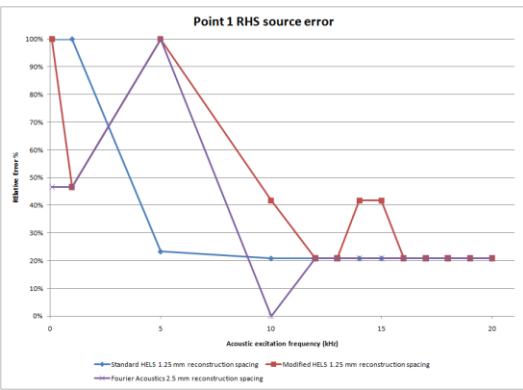
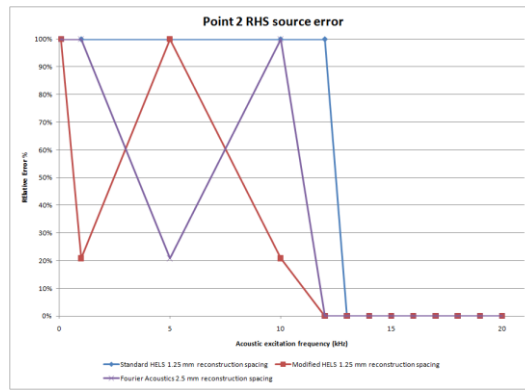


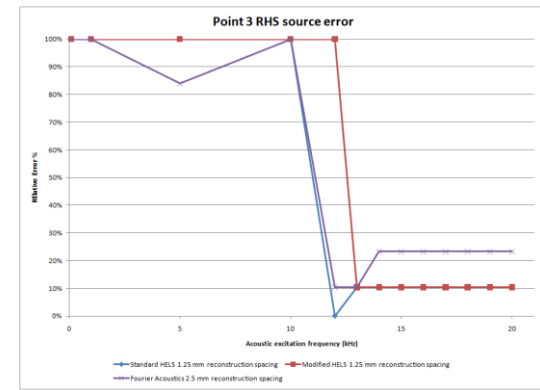
Figure 0.17: Relative error analysis of LHS source for $\delta=15$ mm, $d=15$ mm, $\phi=\frac{\pi}{2}$ radians – a) location 1; b) location 2; c) location 3; d) location 4; e) location 5



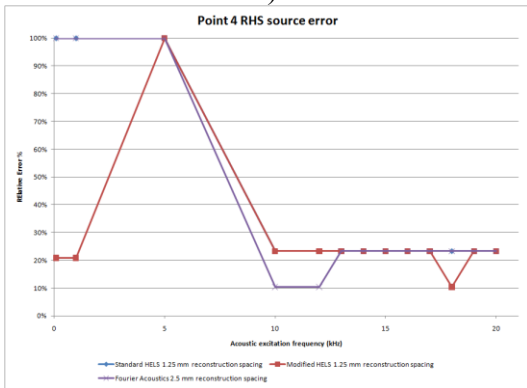
a)



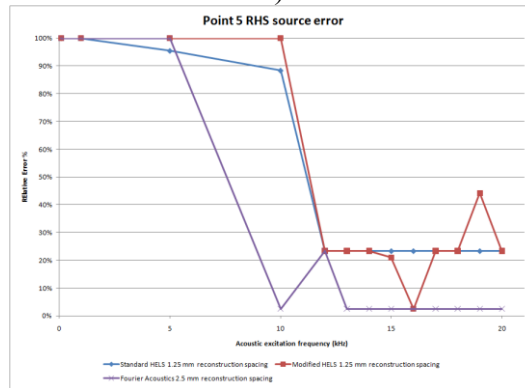
b)



c)



d)



e)

Figure 0.18: Relative error analysis of RHS source for $\delta=15$ mm, $d=15$ mm, $\phi=\frac{\pi}{2}$ radians – a) location 1; b) location 2; c) location 3; d) location 4; e) location 5

Reconstruction with $\delta=15$ mm, $d=15$ mm, $\phi=0$ radians

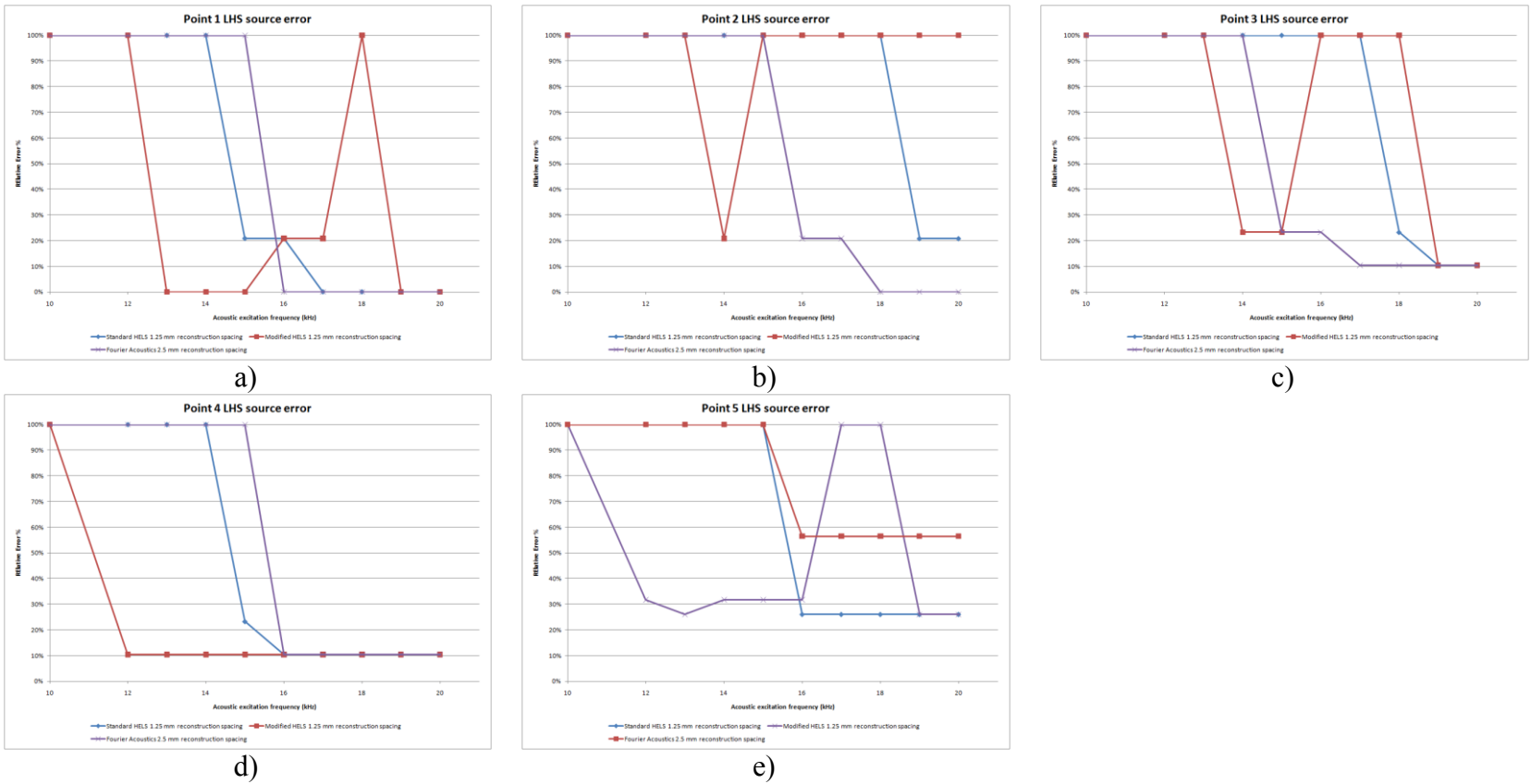
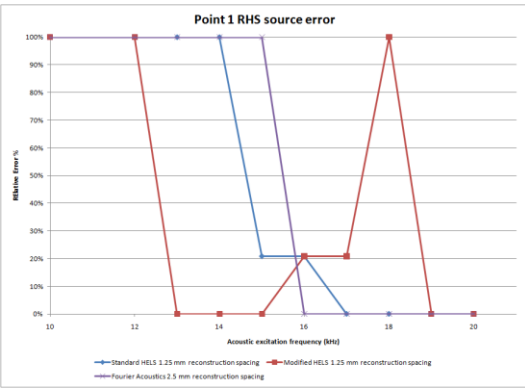
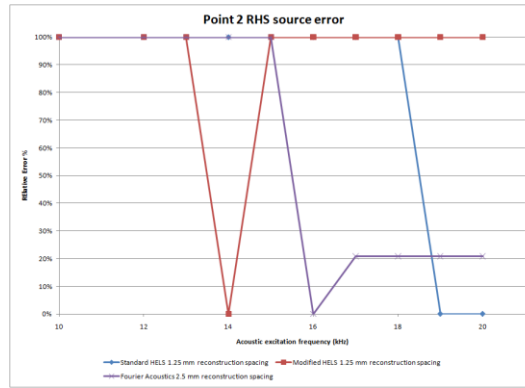


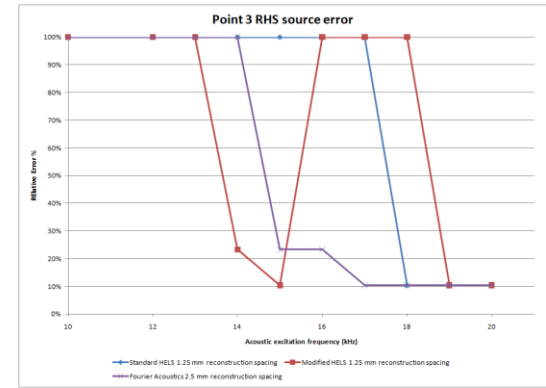
Figure 0.19: Relative error analysis of LHS source for $\delta=15$ mm, $d=15$ mm, $\phi=0$ radians – a) location 1; b) location 2; c) location 3; d) location 4; e) location 5



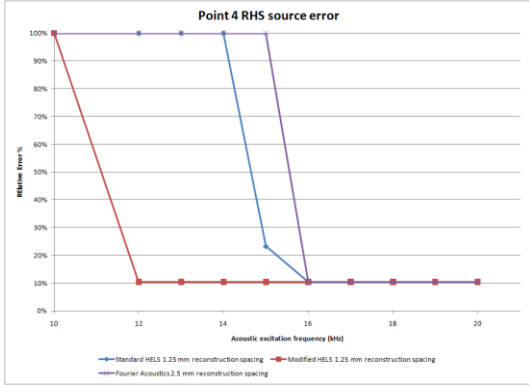
a)



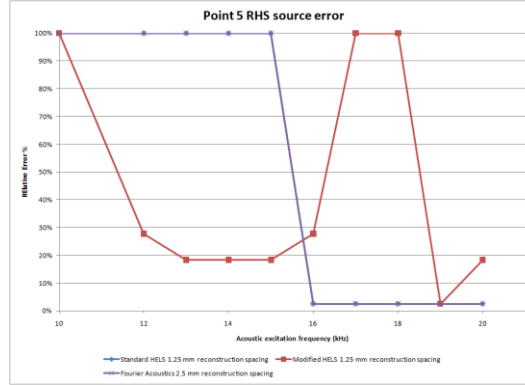
b)



c)



d)



e)

Figure 0.20: Relative error analysis of RHS source for $\delta=15$ mm, $d=15$ mm, $\phi=0$ radians – a) location 1; b) location 2; c) location 3; d) location 4; e) location 5

Reconstruction with $\delta=10$ mm, $d=15$ mm, $\phi=\pi$ radians

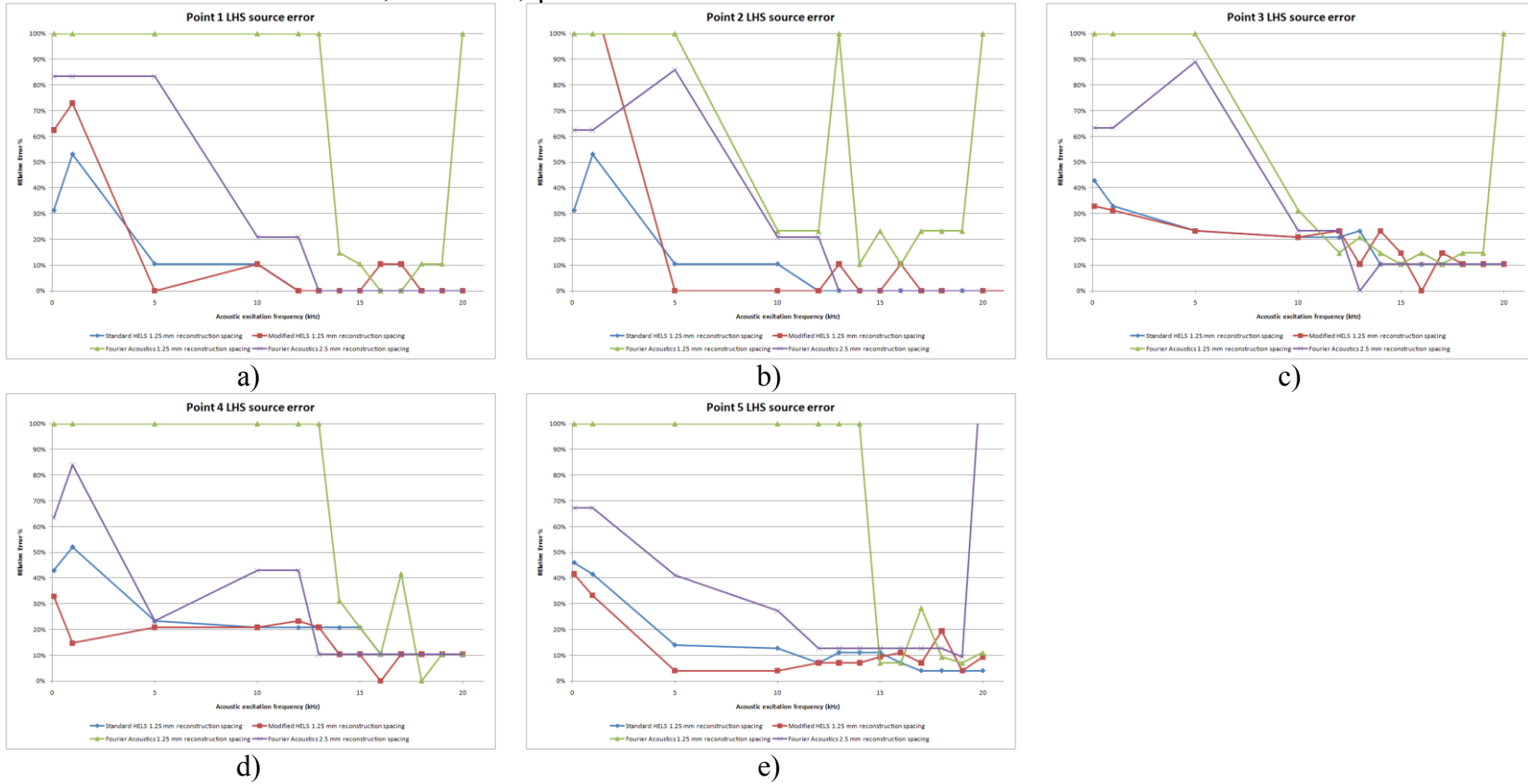
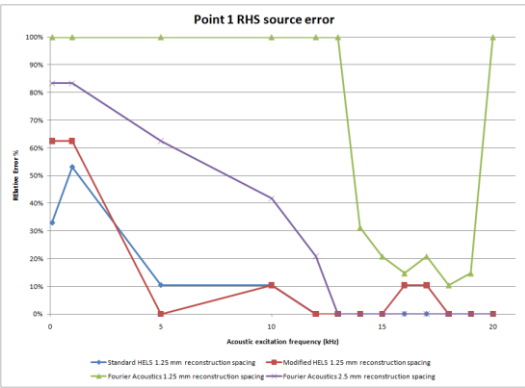
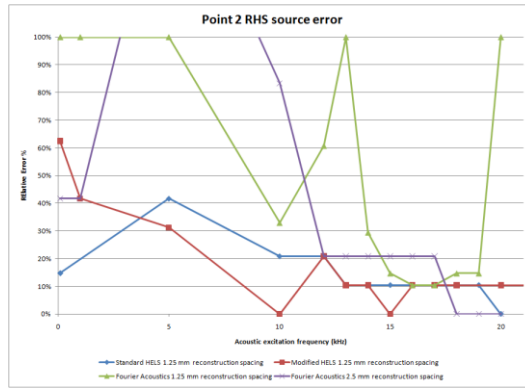


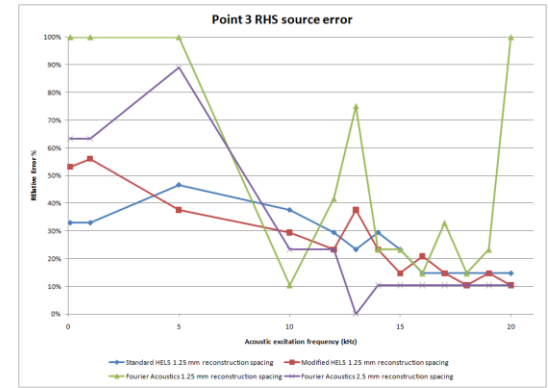
Figure 0.21: Relative error analysis of LHS source for $\delta=10$ mm, $d=15$ mm, $\phi=\pi$ radians – a) location 1; b) location 2; c) location 3; d) location 4; e) location 5



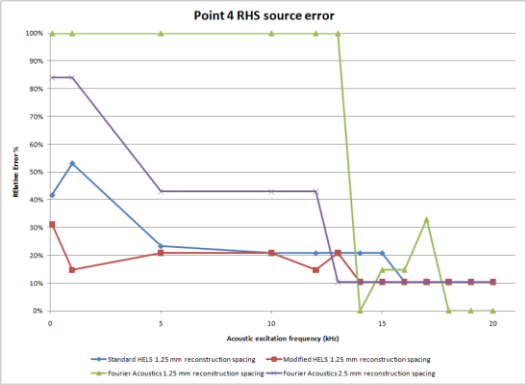
a)



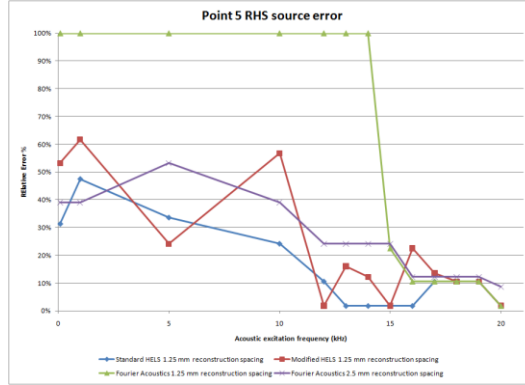
b)



c)



d)



e)

Figure 0.22: Relative error analysis of RHS source for $\delta=10$ mm, $d=15$ mm, $\phi=\pi$ radians – a) location 1; b) location 2; c) location 3; d) location 4; e) location 5

Reconstruction with $\delta=10$ mm, $d=15$ mm, $\phi=\frac{\pi}{2}$ radians

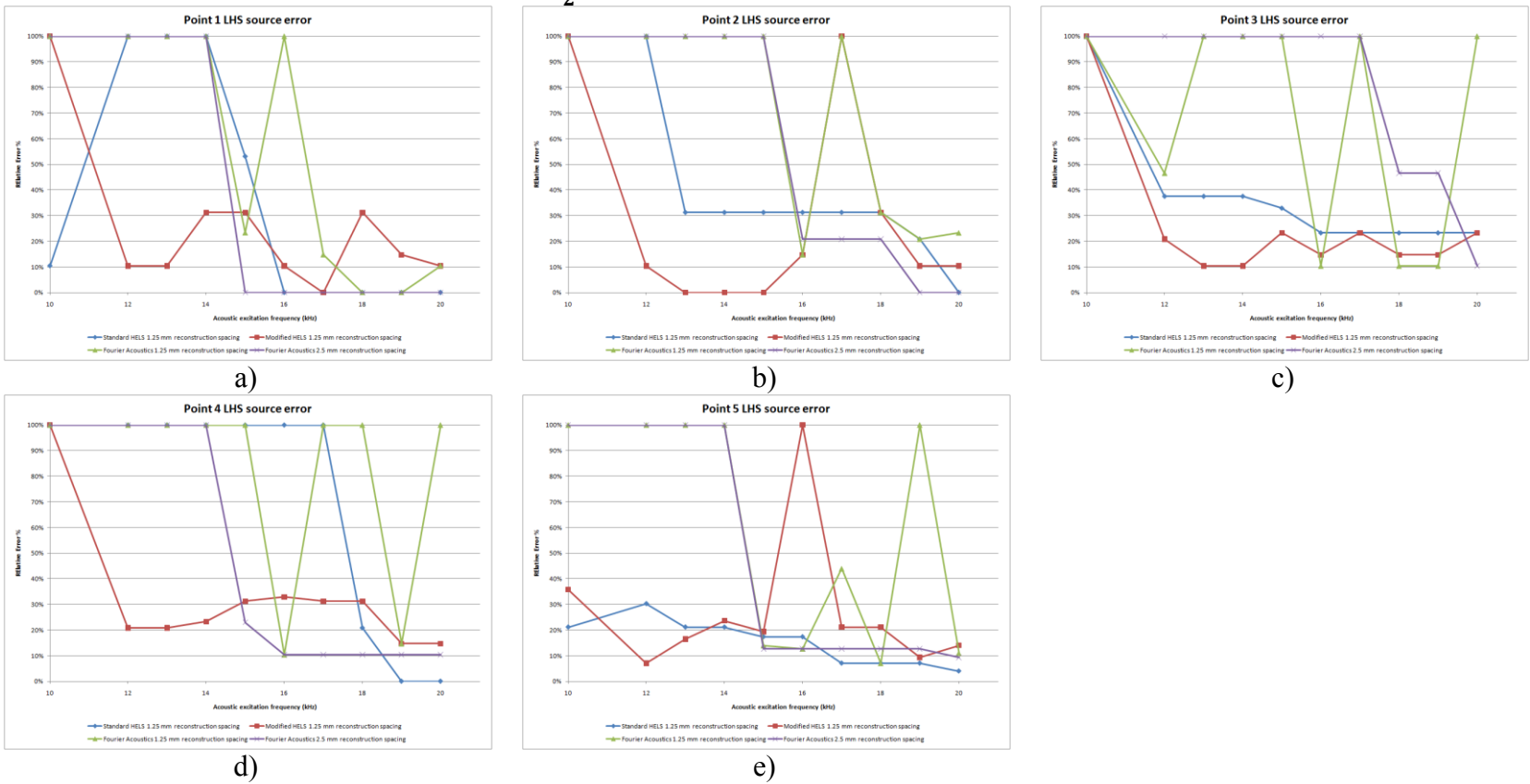
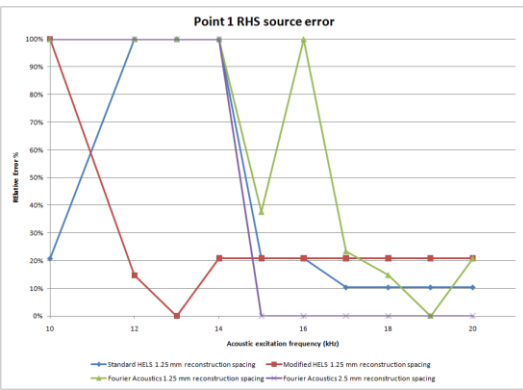
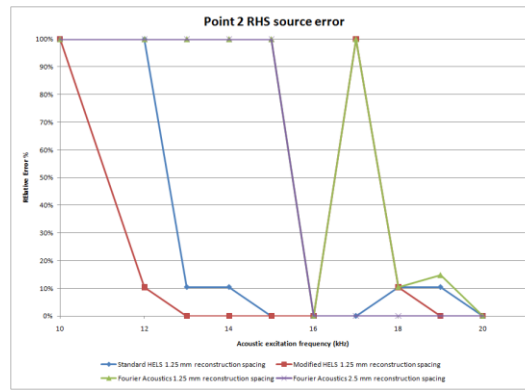


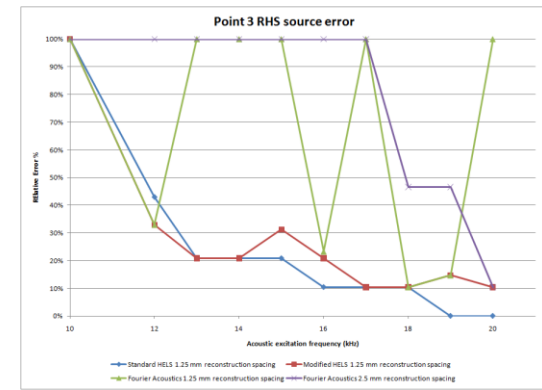
Figure 0.23: Relative error analysis of LHS source for $\delta=10$ mm, $d=15$ mm, $\phi=\frac{\pi}{2}$ radians – a) location 1; b) location 2; c) location 3; d) location 4; e) location 5



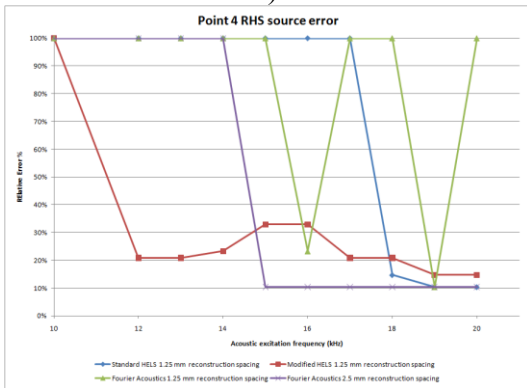
a)



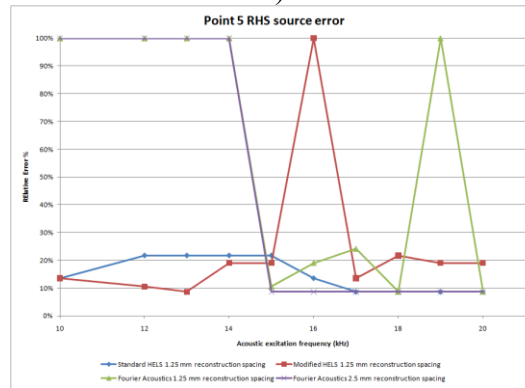
b)



c)



d)



e)

Figure 0.24: Relative error analysis of RHS source for $\delta=10$ mm, $d=15$ mm, $\phi=\frac{\pi}{2}$ radians – a) location 1; b) location 2; c) location 3; d) location 4; e) location 5

Reconstruction with $\delta=10$ mm, $d=15$ mm, $\phi=\pi/2$ radians

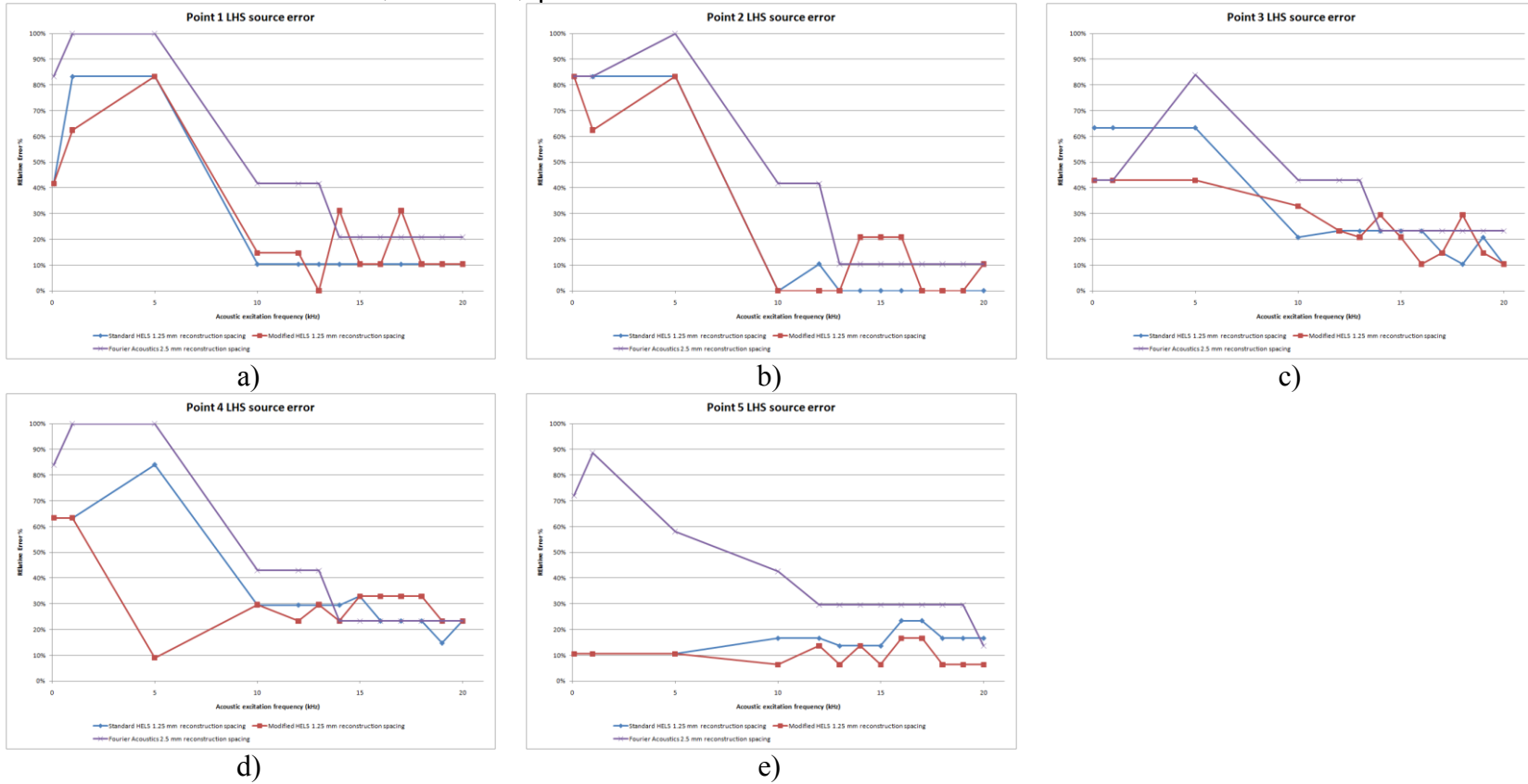
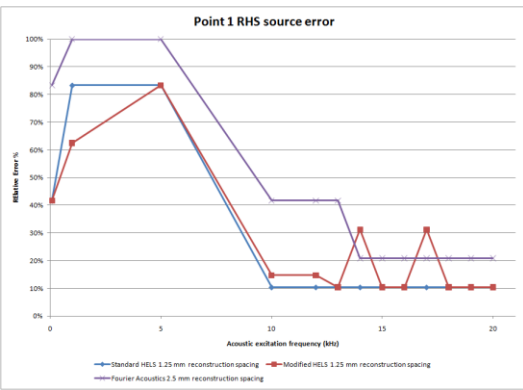
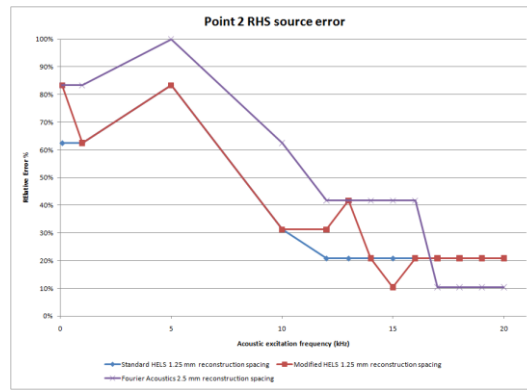


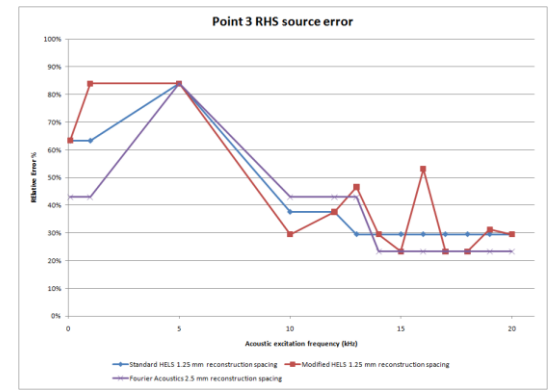
Figure 0.25: Relative error analysis of LHS source for $\delta=5$ mm, $d=15$ mm, $\phi=\pi$ radians – a) location 1; b) location 2; c) location 3; d) location 4; e) location 5



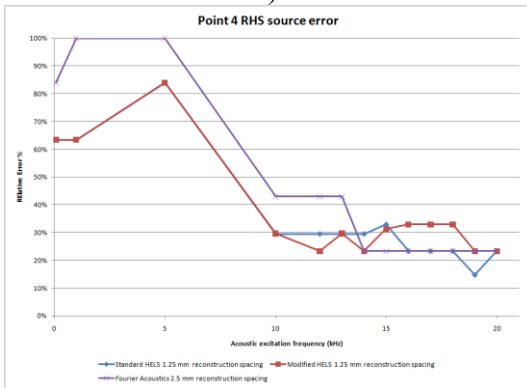
a)



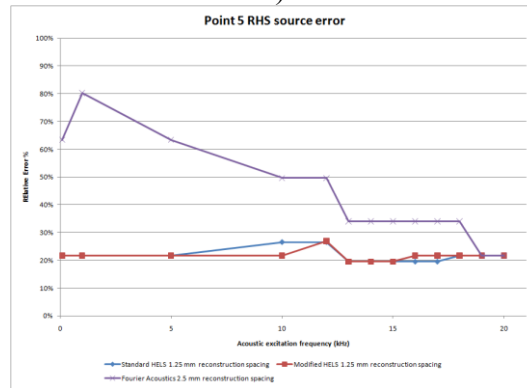
b)



c)



d)



e)

Figure 0.26: Relative error analysis of RHS source for $\delta=5$ mm, $d=15$ mm, $\phi=\pi$ radians – a) location 1; b) location 2; c) location 3; d) location 4; e) location 5

Ghost source identification

Results show that all methods are susceptible to ghost images when reconstructing sources out of phase by $\frac{\pi}{2}$ radians or less. Ghost images occur when any portion of the acoustic radiation pattern of multiple sources are in phase. In the case of a phase difference of $\frac{\pi}{2}$ and 0 radians, a significant portion of the radiated wave patterns are in phase. Therefore, a method was required to ensure that the assumptions regarding source reconstruction location in the simulation results are valid.

Ghost images can be identified by shifting the measurement surface with respect to the source surface. Shifting the measurement surface changes the relative phase between the ghost and real sources. Figure 4.27 illustrates ghost imaging identification for $\delta=10$ mm, $d=15$ mm, $\phi=\frac{\pi}{2}$ at 14 kHz using Modified HELS. Applying a measurement shift to the numerical simulations significantly reduced the amplitude of the ghost image and shifted it towards the center of the reconstruction surface (lower right hand corner of surface). Therefore, the reduced and shifted source is deemed a ghost image and is disregarded. Though identifying ghost images requires another set of measurements and analysis, such a methodology is required regardless of the NAH methodology used.

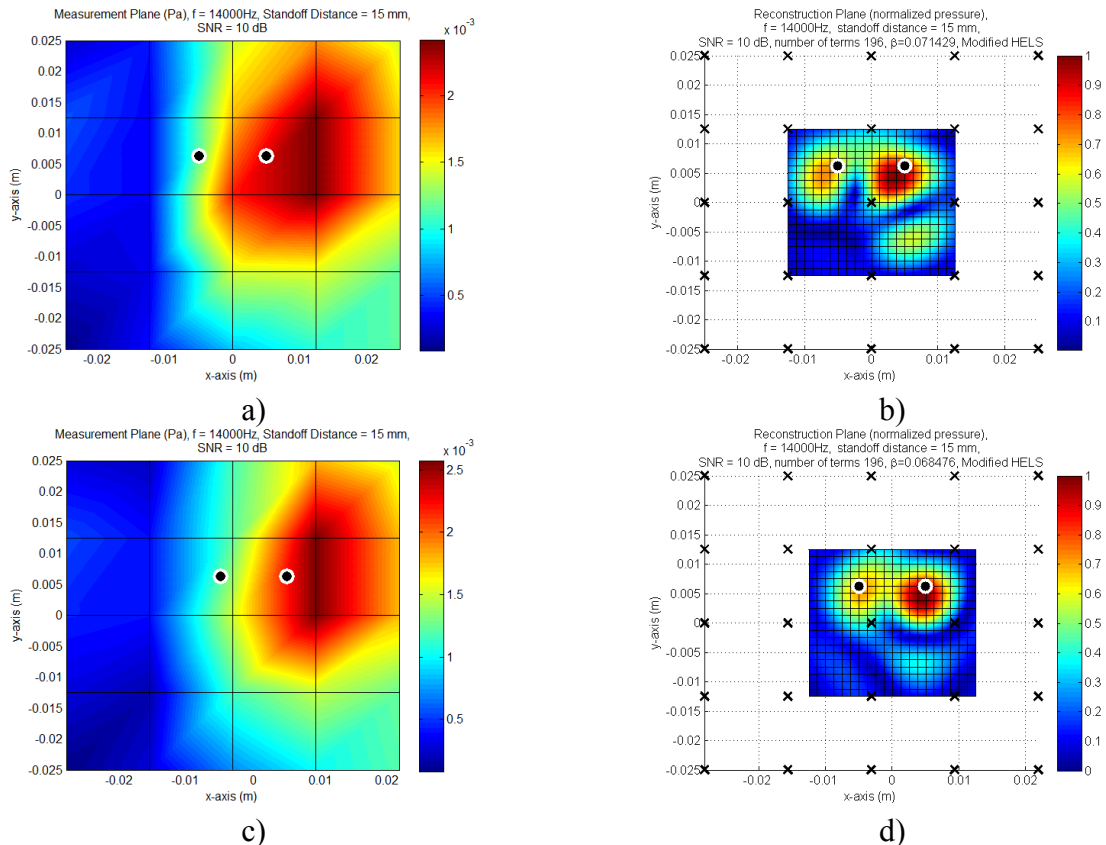


Figure 0.27: Reconstruction from a shifted measurement location to identify ghost sources – a) original measurement surface; b) original reconstruction surface with ghost sources located in lower right hand corner; c) shifted measurement surface; d) shifted reconstruction surface with shifted ghost source and reduced amplitude.

Regularization justification

TSVD and TR with GCV were both used to determine which method provided the most accurate reconstructions over the spectrum of parameters tested. In many cases both methods showed similar results. Unfortunately, because of a lack of a gap in the singular values, no significant inflection points and relatively small values at high frequency caused TSVD to be ineffective in some cases. In most cases where TSVD was ineffective, TR was able to reconstruct accurately. Figure 4.29 shows a case where TR produces significantly improved reconstruction over TSVD.

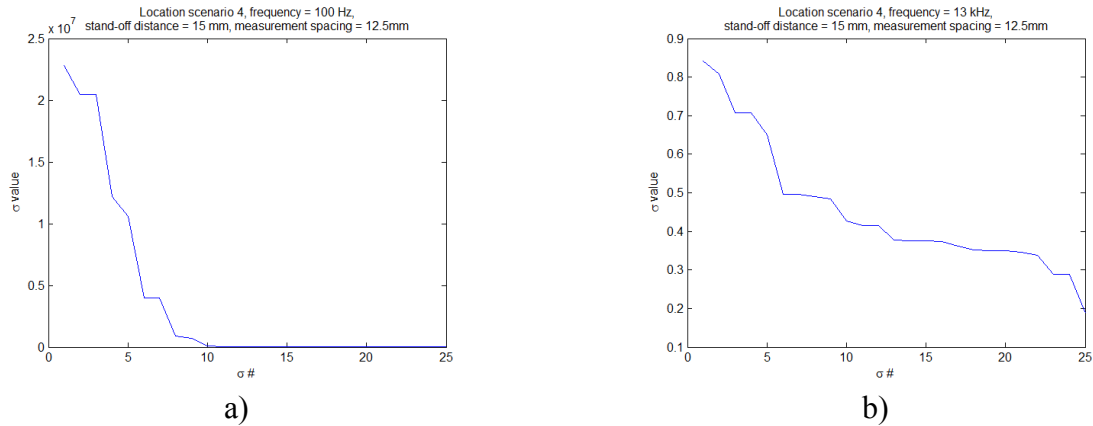


Figure 0.28: Comparison of singular values at 100 Hz and 13 kHz. The 100 Hz case is characterized by a group of large and small singular values, whereas the 13 kHz case only has small singular values

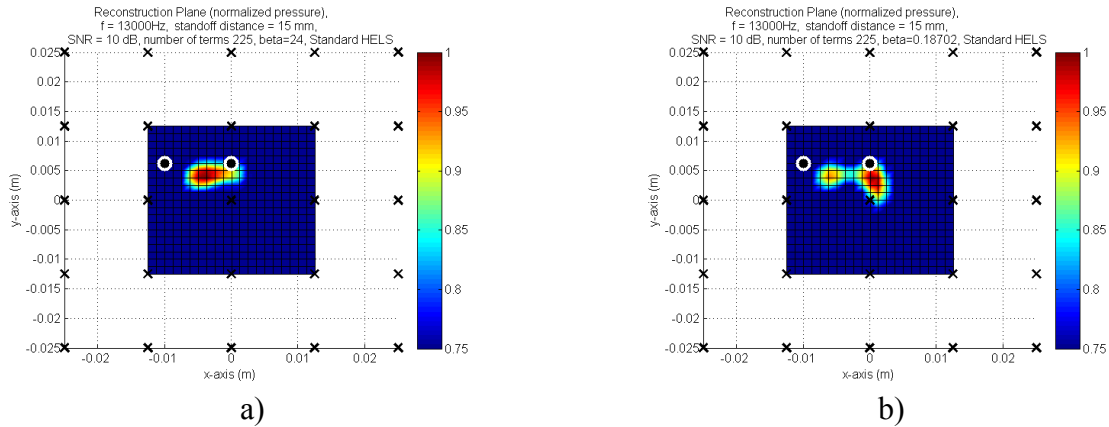


Figure 0.29: a) Reconstruction of location scenario 4 at 13 kHz, $\delta=10\text{mm}$ and $\phi=\frac{\pi}{2}$ with TSVD; b) Reconstruction of location scenario 4 at 13 kHz, $\delta=10\text{mm}$ and $\phi=\frac{\pi}{2}$ with TR

GCV with HELS and Modified HELS showed success in finding an optimal β value for TR⁷⁴. However, Fourier Acoustics did not show similar correlations. β values produced by GCV in the case of HELS were 4-5 times the order of magnitude of that of Fourier Acoustics. The difference in β values is due to the increased number of measurement points required in Fourier Acoustics to create an equivalent reconstruction surface. Increasing the number of

measurement points increases the number of singular values and the discrete ill-posedness of the problem.

Difficulties with minimum GCV values near zero were investigated by Wahba and Wang⁷⁵. They show as the number of data points increases, the likelihood of β approaching zero increases exponentially. Therefore, β values were chosen manually for Fourier Acoustics in an attempt to find a parameter that would produce a well-conditioned problem while also not over-smoothing the surface. An example of Fourier Acoustics with β determined by GCV and manually is shown in figure 4.30.

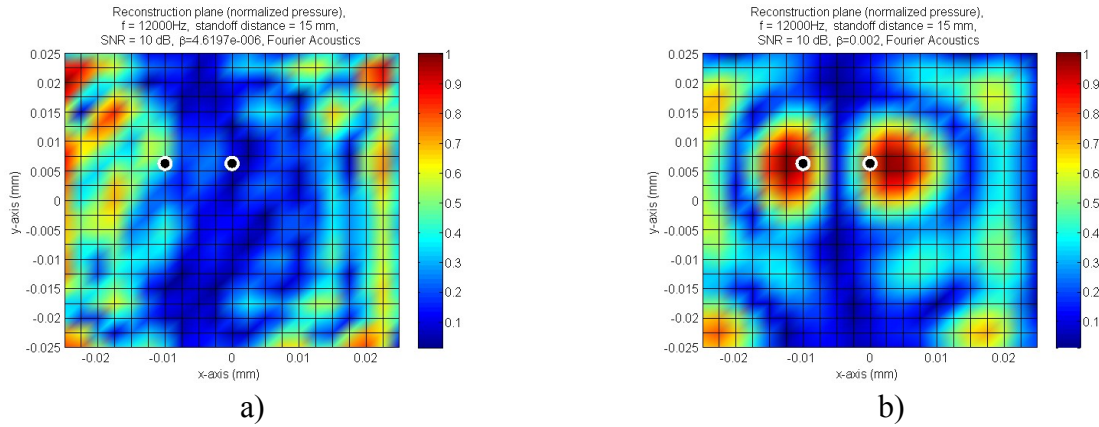


Figure 0.30: a) Reconstruction of location scenario 4 at 12 kHz, $\delta=10\text{mm}$ and $\phi=\pi$ with β chosen via GCV; b) Reconstruction of location scenario 4 at 13 kHz, $\delta=10\text{mm}$ and $\phi=\pi$ β chosen manually

Modified HELS and the relationship of frequency and reconstructed source accuracy

The field pressure radiation from a point source is dependent on the acoustic wavenumber (i.e. frequency) and the radial distance between the source and the field point.

$$\hat{P}_m = \hat{S} \frac{e^{ikR_m}}{R_m} \quad (4.4)$$

Frequency, and consequently, spherical spreading plays a role in reconstruction accuracy. The role of frequency and spherical spreading can be shown by taking the gradient of a single monopole source. If the pressure gradient of a source is high, the spherical spreading of the source will be small since the point-to-point pressure difference will be large. Sources in close proximity to each other with high spatial gradient consequently result in less interference than cases with smaller gradients, since pressure amplitude reduces significantly with increasing in-plane distance from the center of the source.

$$\vec{\nabla} \hat{p}_m = \frac{\partial \hat{p}_m}{\partial R} = \hat{S} i k \frac{e^{i k R_m}}{R_m} \quad (4.5)$$

Equation (4.5) shows the gradient is proportional to the acoustic wavenumber. Therefore, with increasing frequency, the gradient increases and less spherical spreading occurs. To illustrate, two point sources separated by 10 mm are located on a line extending from -25 to 25 mm, and measurements are taken at a stand-off distance of 15 mm (figure 4.31). The radiated pressure is shown for phase differences of 0, $\frac{\pi}{2}$, and π for frequencies of 100 Hz and 20 kHz. The source locations are located at -5 and 5 mm from the origin.

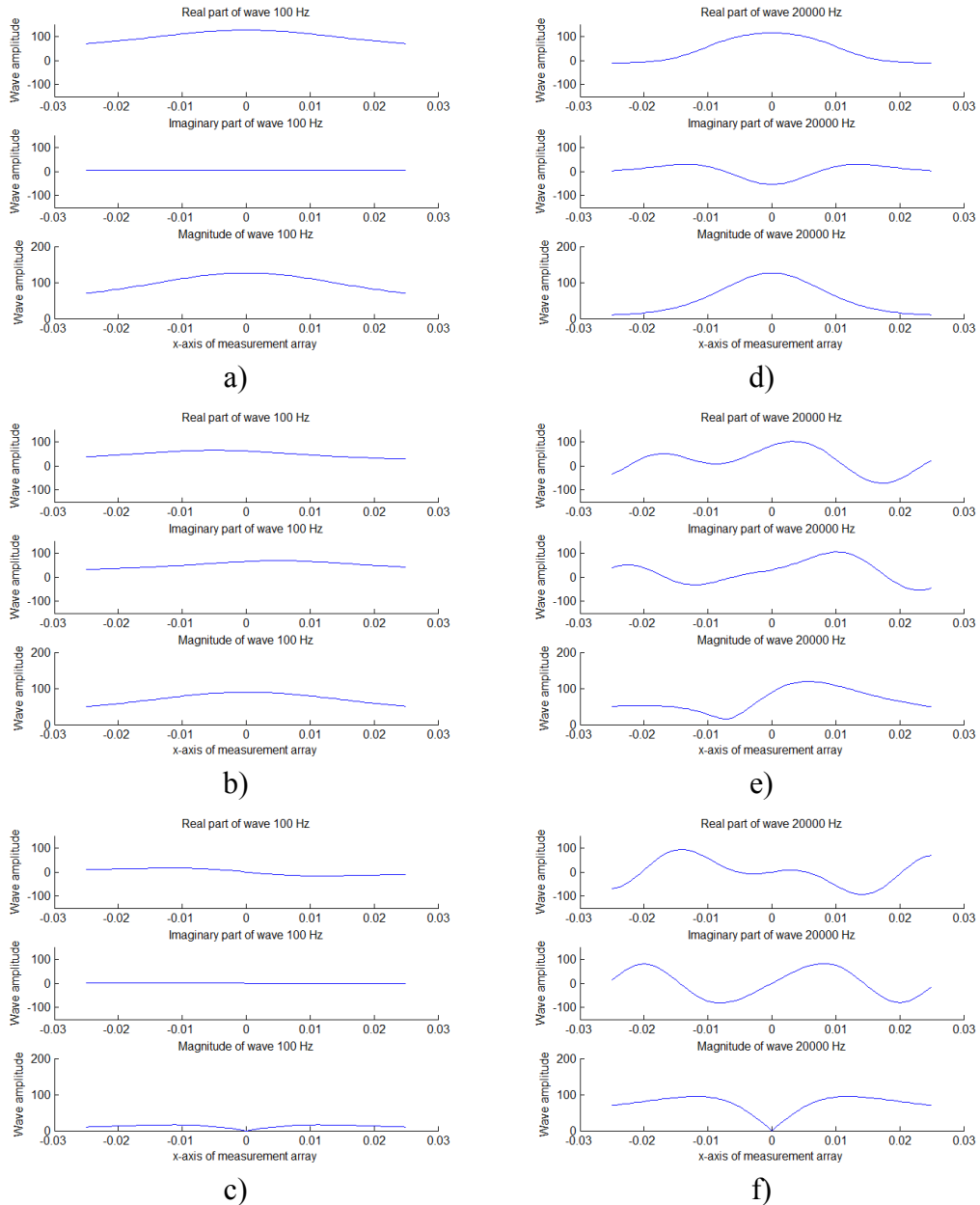


Figure 0.31: Wavefronts of two coherent sources on a line demonstrating the relationship between spherical spreading and interference at the measurement plane – a) $f=100$ Hz, $\phi=0$; b) $f=100$ Hz, $\phi=\frac{\pi}{2}$; c) $f=100$ Hz, $\phi=\pi$; d) $f=20$ kHz, $\phi=0$; e) $f=20$ kHz, $\phi=\frac{\pi}{2}$; f) $f=20$ kHz, $\phi=\pi$

Magnitudes of the 100 Hz sources show no significant difference exists between the amplitudes of the 0 and $\frac{\pi}{2}$ phase angle cases. Therefore, the inability to reconstruct at low frequencies with a phase angle of $\frac{\pi}{2}$ is similar to attempting to reconstruct two sources completely in phase (i.e. $\phi=0$). Once the sources are out of phase by π , two sources are visible in the measurement plane, and one would expect accurate reconstruction at the source surface.

Increasing the frequency of the point sources to 20 kHz shows a dramatic shift in the imaginary component and magnitude of the radiation when the two sources are out of phase by $\frac{\pi}{2}$. Significant destructive interference occurs to the LHS source, which is illustrated in the imaginary component of the field. The differences at higher frequencies produce characteristics of two separate sources not seen at lower frequencies.

Extending the observations to Modified HELS, the weighted measured pressure is shown for 14 and 20 kHz frequencies and phase differences of 0, $\frac{\pi}{2}$, and π for the same source locations. 14 kHz matches a frequency at which Standard HELS has difficulty reconstructing in the three dimensional version of the system given (source location four), whereas Modified HELS was capable of accurate reconstruction. Both methods were able to reconstruct sources accurately at 20 kHz.

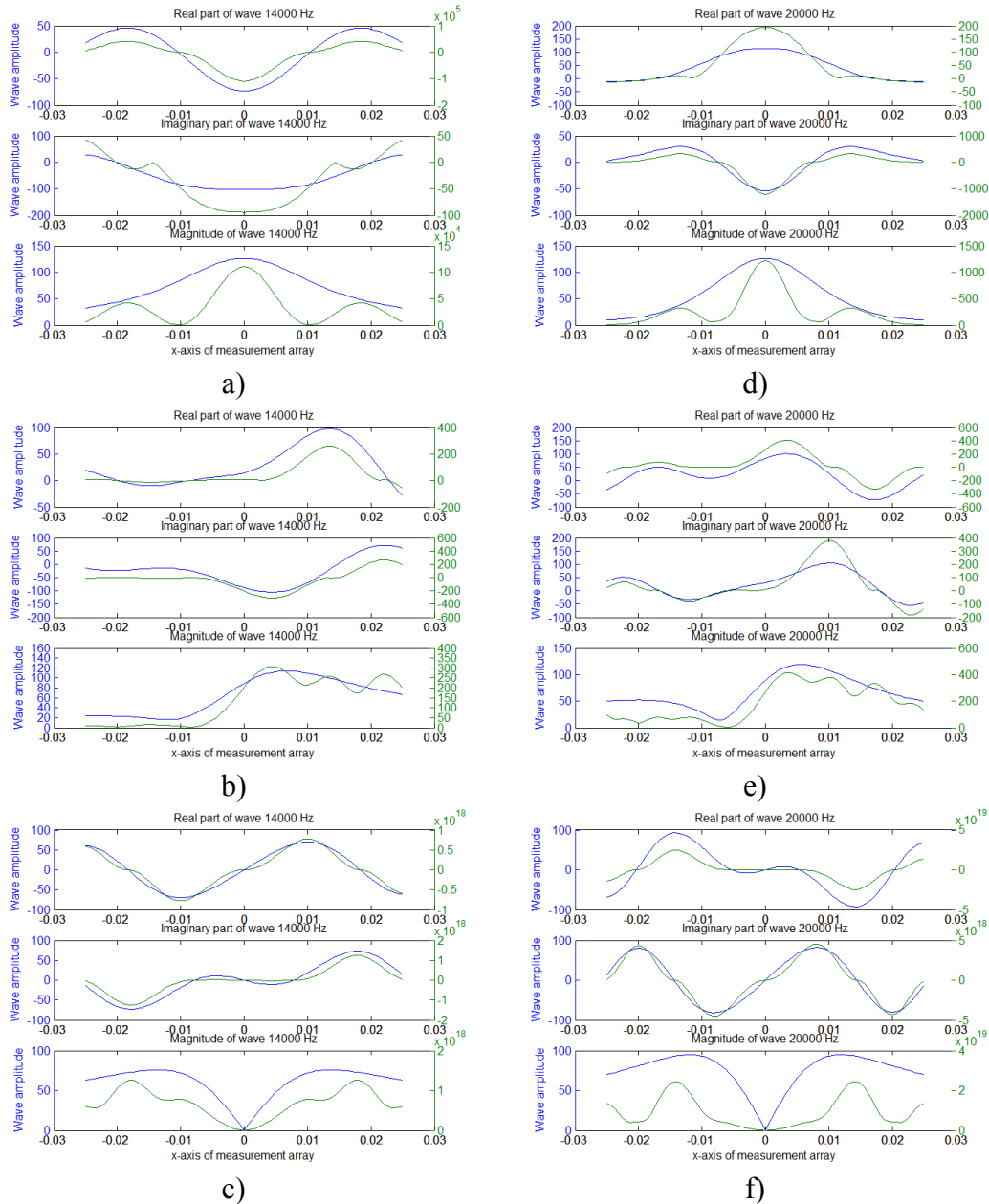


Figure 0.32: Comparison of non-weighted and weighted wavefronts of two coherent sources on a line demonstrating the effects on interference at the measurement plane – a) $f=14$ kHz, $\phi=0$; b) $f=14$ kHz, $\phi=\frac{\pi}{2}$; c) $f=14$ kHz, $\phi=\pi$; d) $f=20$ kHz, $\phi=0$; e) $f=20$ kHz, $\phi=\frac{\pi}{2}$; f) $f=20$ kHz, $\phi=\pi$

Of particular interest are the cases at $\phi = \frac{\pi}{2}$. Comparing the weighted and non-weighted amplitudes in subfigure (b) shows characteristics of a peak in pressure left of the LHS source with weighted measurement pressures. On the other hand, the non-weighted pressure shows no significant change in pressure. To be fair, the overlaid plots are not at the same scale. Therefore, magnitude plots are shown in figure 4.33 with equal scaling for the $\phi = \frac{\pi}{2}$ cases.

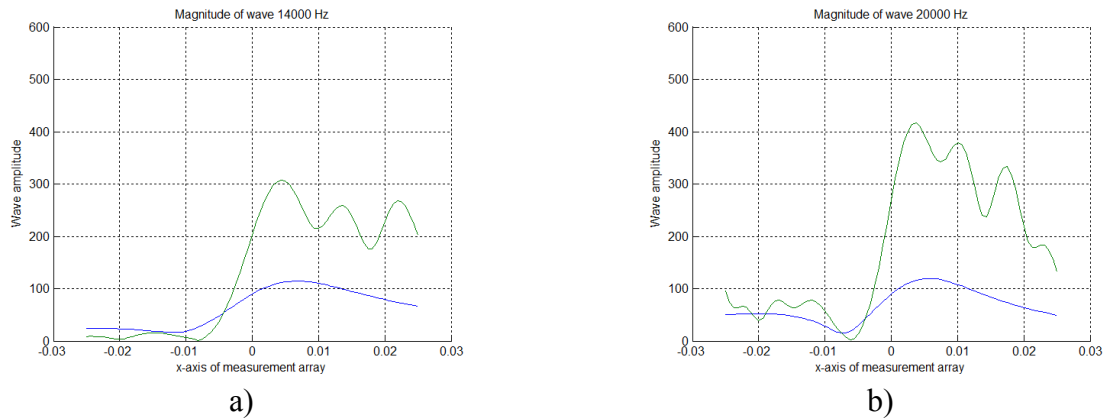


Figure 0.33: Comparison of non-weighted and weighted wavefront magnitudes of two coherent sources on a line demonstrating the effects on interference at the measurement plane – a) $f=14$ kHz, $\phi=\frac{\pi}{2}$; b) $f=20$ kHz, $\phi=\frac{\pi}{2}$

Figure 4.33 shows a definitive peak left of the LHS source in the weighted case at 14 kHz, whereas the non-weighted case does not. In the case of 20 kHz, a significant rise in magnitude can be seen in both variants of the measurement pressures. As stated earlier, both Standard and Modified HELS were capable of accurate reconstruction at 20 kHz, whereas at 14 kHz only Modified HELS produced accurate reconstruction locations. Further review of equations (3.20-3.22), show that Modified HELS effectively increases the pressure gradient at the measured surface by amplifying the highest pressure levels of the measurement plane. In effect, weighting the measured pressure reduces the interference due to spherical spreading.

$$\begin{aligned}
P_{\text{mod}} &= P_{w,\text{real}} + P_{w,\text{imag}} \\
P_{w,\text{real}} &= \left| \frac{\text{real}(p_n) - \text{mean}(\text{real}(p))}{\text{mean}(\text{real}(p))} \right| \\
P_{w,\text{imag}} &= \left| \frac{\text{imag}(p_n) - \text{mean}(\text{imag}(p))}{\text{mean}(\text{imag}(p))} \right|
\end{aligned} \tag{3.20, 3.21, 3.22}$$

Similar characteristics do not produce accurate reconstruction locations in the case of $\phi \neq 0$. The root cause may be the symmetry of the measured pressures, which produces the largest amount of constructive interference. At small δ , this leads to minimal pressure difference between the radiated sources with increasing stand-off distance. Based on the above, guidelines for determining the feasibility of source reconstruction in relation to acoustic wavenumber, stand-off distance, source separation and relative phase angle are needed before the methods can be applied in practice.

Conclusions

Testing of the NAH resolution guidelines with respect to HELS, Modified HELS and Fourier Acoustics were done by numerical simulations. Acoustic frequency, stand-off distance, phase angle, source separation and source locations were varied to provide a general understanding of the capabilities of the three methods with respect to coherent point source reconstruction.

Simulations show that the NAH resolution guidelines do not apply to coherent point sources. The guidelines are based on the angular spectrum which assumes sinusoidal motion across the entire plane, whereas the oscillations of point sources are locally concentrated. However, the relationship of decreased resolution with increased stand-off distance still holds based on the physics of the problem.

The NAH guidelines do not correlate exactly for point sources. On the other hand, simulations show that HELS significantly increases the reconstruction location accuracy as frequency decreases and stand-off distance increases. However, accurate reconstruction is limited above some low frequency limit. The low frequency limit is likely based on the amount of spherical spreading produced, which was shown to be dependent on stand-off distance, relative phase angle between sources, source separation and frequency.

Furthermore, Modified HELS was able to produce more accurate reconstructions than Standard HELS at lower frequencies. In particular, as the source separation and phase angle decreased, Modified HELS showed significant advantages. However, a few frequencies showed poor reconstruction accuracy.

Overall, both HELS methods were shown to be more accurate in reconstruction of coherent point sources than Fourier Acoustics with significantly fewer measurements. In our simulations, the HELS methods required 25 measurements, whereas Fourier Acoustics used 441 measurements. Also, further refinement of the reconstruction surface of the HELS method was feasible by reconstructing to the area of interest, which does not increase calculation or measurement time in practical applications. In our simulations, the reconstruction surface was reduced to 1.25 mm spacing. The corresponding Fourier Acoustics model required 1681 measurement points and did not provide consistently accurate reconstructions due to the extreme discrete ill-posedness of the problem. By having fewer required measurements, the level of discrete ill-posedness of HELS is significantly less and regularization is feasible.

CHAPTER 5: EXPERIMENTAL VALIDATIONS

The objective of chapter 5 is to validate the simulations experimentally. Though one could choose objects from everyday life as test subjects, the presence of coherent sources and the uncertainty of source frequencies, makes it difficult to determine if the methods provide accurate reconstructions. Therefore, a direct comparison of the numerical simulations is made by approximating two point sources in a lab setting. Due to the significant number of measurements required for Fourier Acoustics, only Standard and Modified HELS are used to validate the numerical simulations.

Test setup

Two monopole sources are created by placing a speaker within two six inch rubber cones separated by approximately 0.5 m. The cones are heavily insulated to limit transmission loss through the open end of the cone and its walls. At the apex of the cone, a nylon tube (0.5 m long 9 mm OD/3 mm ID) is inserted into the cone to approximate a plane wave. The objective of approximating a plane wave is to limit the energy loss over distance from the source location (a theoretical plane wave's energy does not vary with distance from the source). At the end of the nylon tubes, 1.5 mm orifices are inserted to create two point sources. Testing was done at Wayne State University's Acoustic Noise Vibration Controls (AVNC) laboratory in an anechoic chamber to approximate the free-field conditions used in simulation.

Source location scenario three with a phase angle of $\phi = \frac{\pi}{2}$ was chosen to validate experimentally, since the location scenario can be setup visually without much difficulty.

Microphone array spacing was set to 12.5 mm to match simulation spacing. δ was set at approximately 10 mm with a standoff distance of 15 mm.

Setting the phase angle of the two sources is difficult in practice. The phase and frequency of the individual sources are set using the “waveplay” function in Matlab©. The waveplay function allows control over individual speakers and produces sound based on user defined data. Sin waves were created for each speaker with adjustable frequencies and phase.

$$\begin{aligned} p_1(t) &= \sin(2\pi ft) \\ p_2(t) &= \sin(2\pi ft + \phi) \end{aligned} \quad (5.1)$$

Where p_1 and p_2 represent the source amplitude, f is the source frequency and ϕ is the phase difference between the two sources. Unfortunately, controlling the phase angle is also dependent on the path of the wave. Phase differences can be created by differences in tube length, restrictions within the tubes and errors within the computer soundcard. Therefore, to ensure that a phase angle of $\frac{\pi}{2}$ radians was tested, the phase angle was varied between 0 and π in increments of $\frac{\pi}{4}$. Source frequencies were tested at 14 and 15 kHz to focus on frequencies showing improved reconstruction accuracy with Modified HELS in comparison to Standard HELS with $\phi = \frac{\pi}{2}$ in simulation.

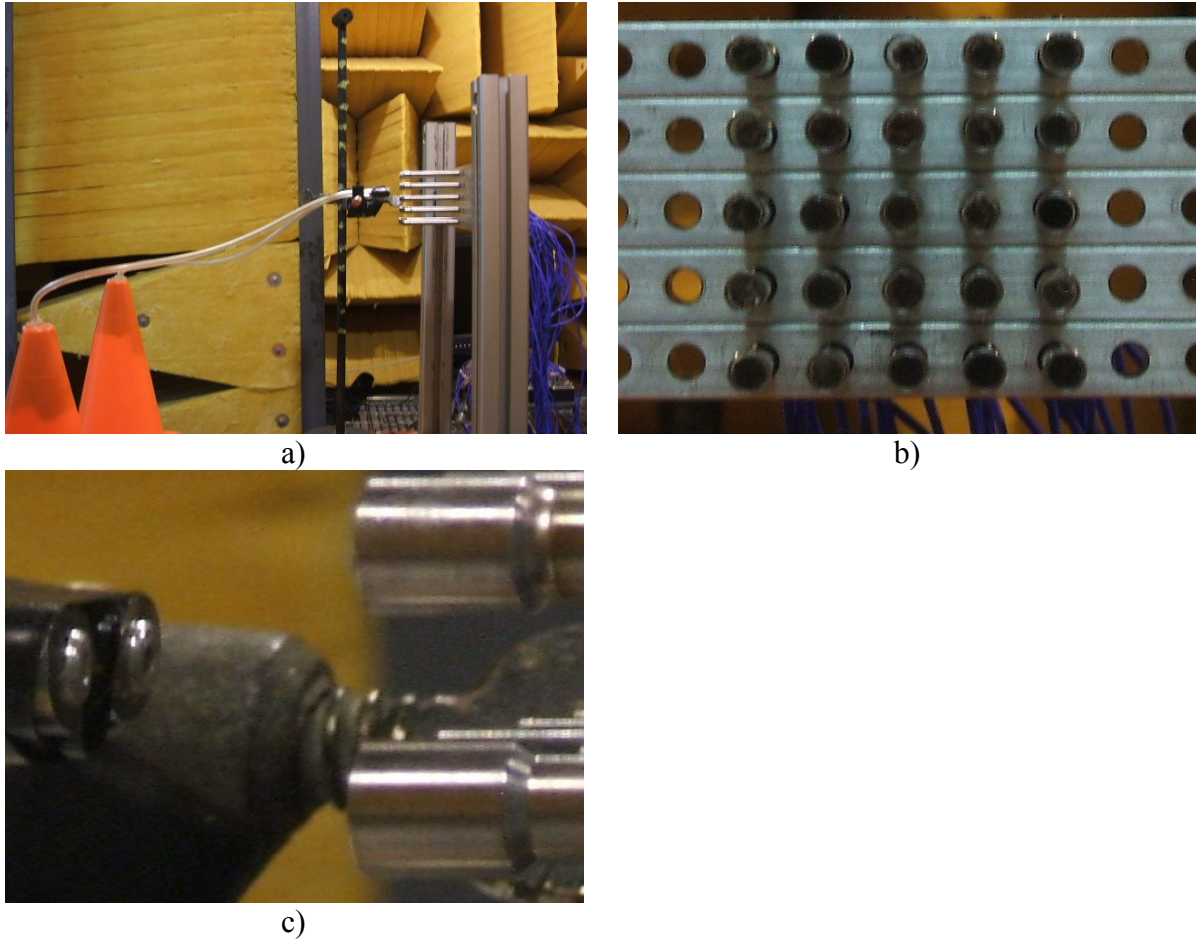


Figure 0.1: a) Test setup; b) 12.5 mm spacing microphone array; c) point source approximated by orifices separated by approximately 10 mm

Experimental results

Error analysis in the presented simulations was based on the relative distance between the actual and reconstructed source locations with respect to measurement spacing. In experimental application, the use of the relative error percentage is difficult, due to measurement accuracy of the source locations with respect to the measurement array. For example, with measurement spacing of 12.5 mm, 1 mm of error in the measurement location results in 8% relative error. Therefore, any error in measurement, human or otherwise, can lead to significant error when comparing to the experimental results. Instead, validation is based on observation of the reconstructed surfaces.

Without quantitative measurements, a baseline to compare the results was created by testing two incoherent sources at the same location as the coherent tests. Incoherent sources are significantly easier to reconstruct since relatively less interference occurs when the source sound waves have a large enough difference in frequency. Figures 5.2-5.8 summarize the results of incoherent and coherent tests. Note that incoherent results are in the upper left hand corner of each figure for comparison.

The order of results is as follows:

- Incoherent sources measurement and reconstruction surfaces (baseline)
- Coherent source measurement surface at 14 kHz
- Coherent source reconstruction surface at 14 kHz (Standard HELS)
- Coherent source reconstruction at 14 kHz (Modified HELS)
- Coherent source measurement surface at 15 kHz
- Coherent source reconstruction at 15 kHz (Standard HELS)
- Coherent source reconstruction at 15 kHz (Modified HELS)

Results show correlation between the commanded and actual phase angles is not good.

Table 5.1 attempts to correlate the commanded phase angle to the actual phase angle based on observation of measurement surfaces.

Table 5.1: Correlation of commanded and actual phase angle of experimental data.
Corresponding subfigure letters for each commanded frequency are in parenthesis.

Acoustic Frequency (kHz)	ϕ (radians)				
	0 (b)	$\frac{\pi}{4}$ (c)	$\frac{\pi}{2}$ (d)	$\frac{3\pi}{4}$ (e)	π (f)
14	$\frac{3\pi}{4}$ to π	$\frac{3\pi}{4}$ to π	$\approx \pi$	$\leq \frac{\pi}{2}$	$< \frac{\pi}{2}$
15	0 to $\frac{\pi}{4}$	0 to $\frac{\pi}{4}$	$< \frac{\pi}{2}$	$< \frac{\pi}{2}$	$\frac{\pi}{2}$ to $\frac{3\pi}{4}$

Based on table 5.1 at 14 kHz, Standard HELS should be capable of reconstruction at all cases with possible exception of (e) and (f), since the phase angles are less than or equal to $\frac{\pi}{2}$. Modified HELS is expected to show improved reconstruction in these cases. At 15 kHz, Standard HELS is expected to produce accurate reconstructions at (f) only. Possible reconstruction may be feasible for cases (d) and (e) with Modified HELS in addition to case (f).

Results show good correlation with the hypotheses mentioned above, with slight differences in reconstructed source location with respect to the incoherent sources. 14 kHz simulations matched the hypotheses except in the case of Standard HELS at case (e), where good reconstruction was possible at an estimated phase angle of less than or equal to $\frac{\pi}{2}$. At case (f), poor reconstruction resulted with Standard HELS, while Modified HELS was able to reconstruct the sources accurately.

15 kHz results also performed as expected. At phase angles near or below $\frac{\pi}{2}$, Standard HELS did not provide good reconstruction. Modified HELS did show distinguishable sources in case (e), whereas Standard HELS did not. Also, an argument can be made that HELS was able to reconstruct two distinguishable sources in the correct location for case (d). Both methods showed good reconstruction for case (f) with a an estimated phase angle between $\frac{\pi}{2}$ and $\frac{3\pi}{4}$.

Overall, experimental results match simulation results for the frequencies and stand-off distances tested. In both frequency cases, Modified HELS produced more accurate reconstructions with decreasing phase angle as shown in simulations. Based on the experimental results, Standard and Modified HELS show promise as methods of reconstructing coherent sources with relative phase angles greater than or equal to $\frac{\pi}{2}$.

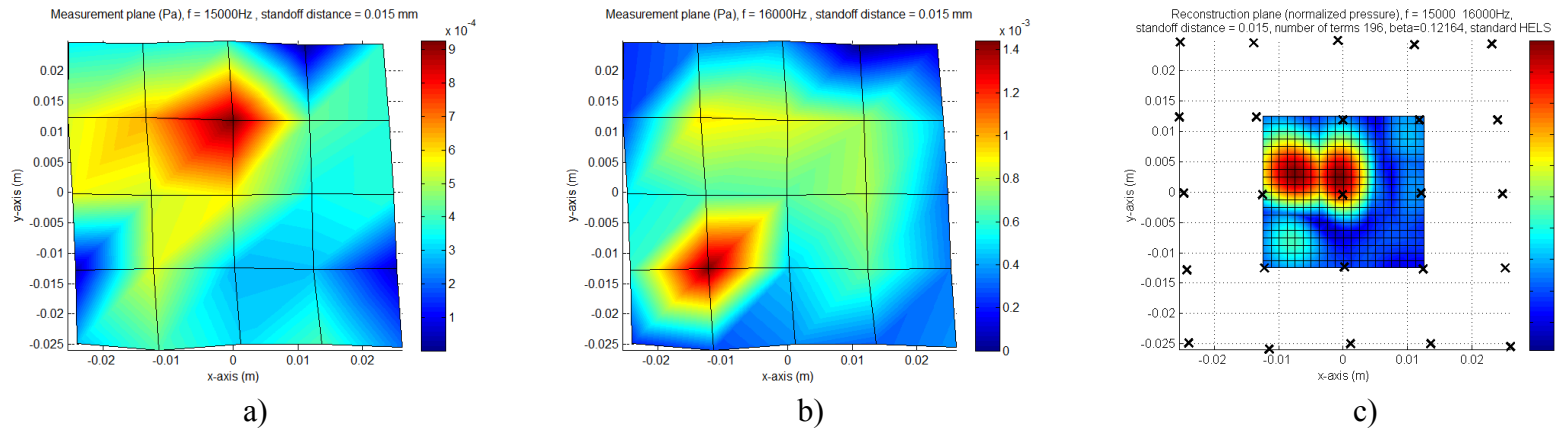


Figure 0.2: Experimental results of baseline test at $\delta=10$ mm, $d=15$ mm at source location scenario 3 (incoherent sources) – a) 15 kHz measurement surface; b) 16 kHz measurement surface c) reconstructed surfaces at 15 and 16 kHz overlaid

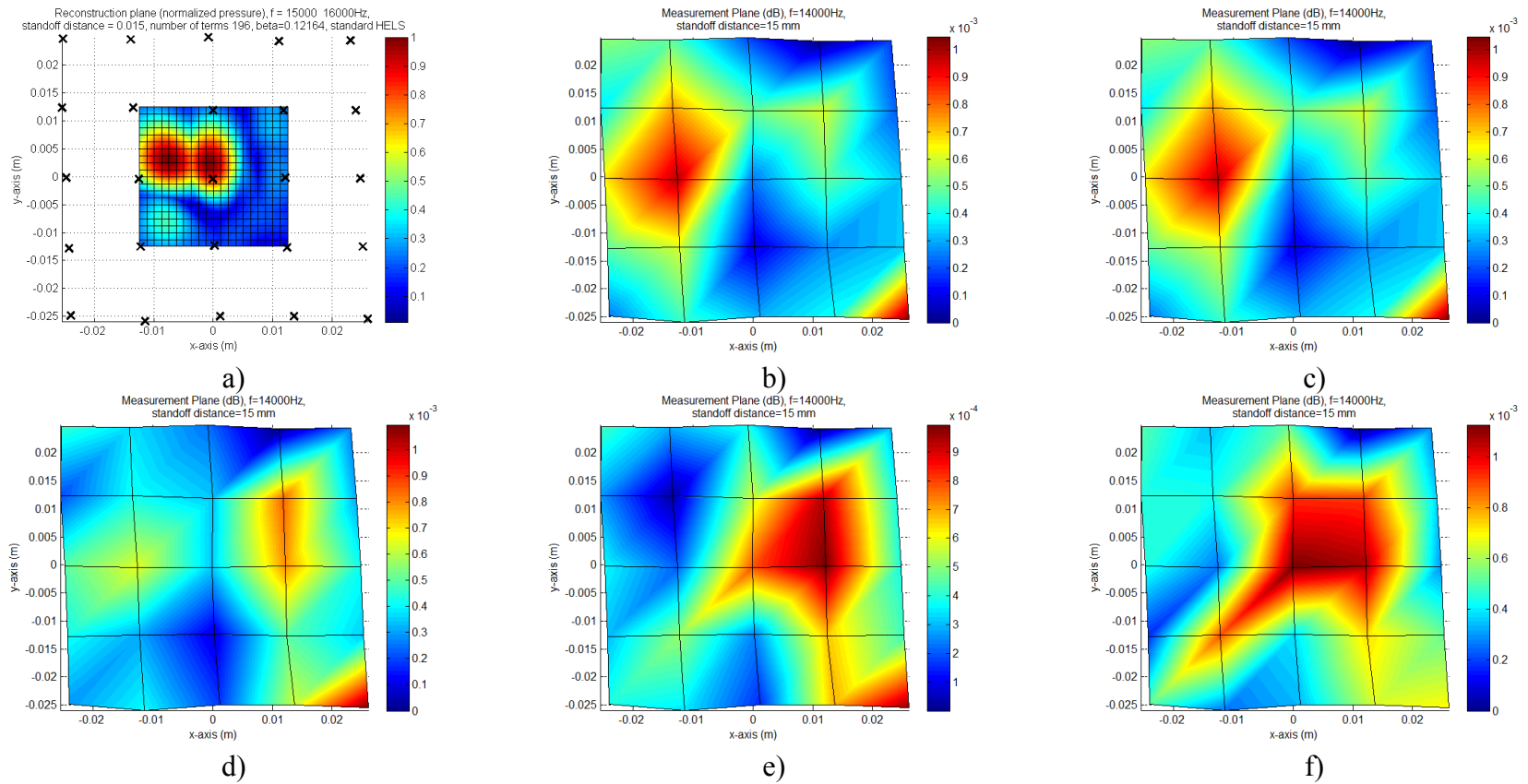
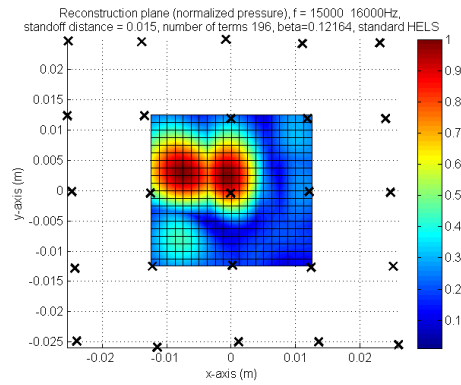
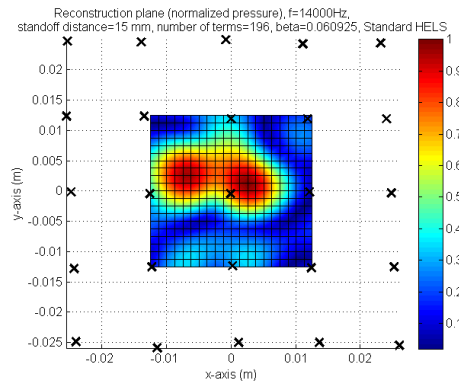


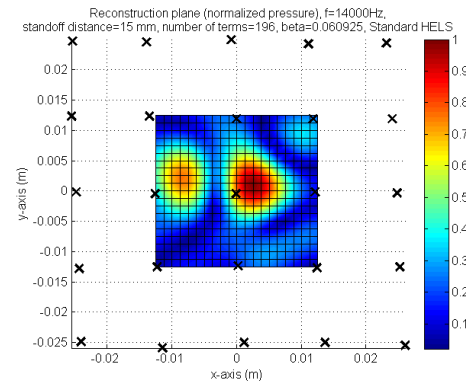
Figure 0.3: Measurement surfaces with $\delta=10$ mm, $d=15$ mm, $f=14$ kHz and varying phase angle at source location scenario 3 – a) reconstruction surface of incoherent sources (baseline); b) measurement surface with $\phi = 0$; c) measurement surface with $\phi = \frac{\pi}{4}$; d) measurement surface with $\phi = \frac{\pi}{2}$; e) measurement surface with $\phi = \frac{3\pi}{4}$; f) measurement surface with $\phi = \pi$



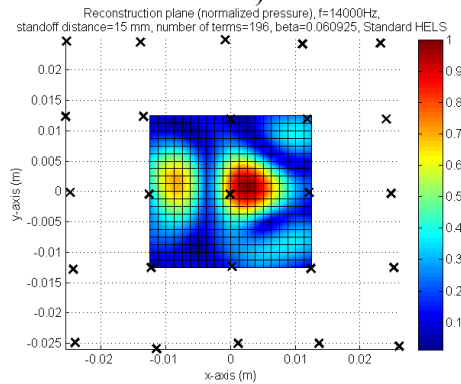
a)



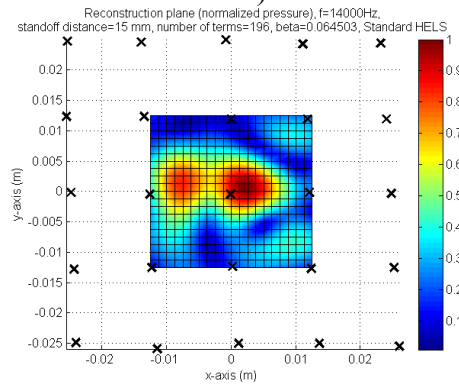
b)



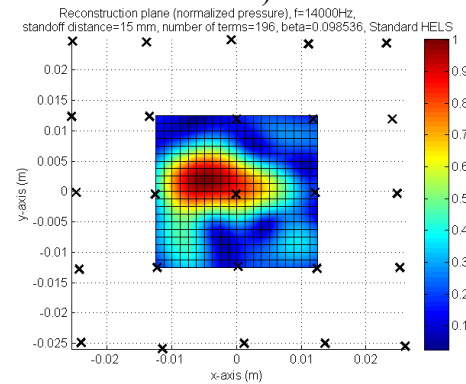
c)



d)



e)



f)

Figure 0.4: Reconstruction surfaces with $\delta = 10$ mm, $d = 15$ mm, $f = 14$ kHz and varying phase angle at source location scenario 3 – a) reconstruction surface of incoherent sources (baseline); b) Standard HELS reconstruction surface with $\phi = 0$; c) Standard HELS reconstruction surface with $\phi = \frac{\pi}{4}$; d) Standard HELS reconstruction surface with $\phi = \frac{\pi}{2}$; e) Standard HELS reconstruction surface with $\phi = \frac{3\pi}{4}$; f) Standard HELS reconstruction surface with $\phi = \pi$

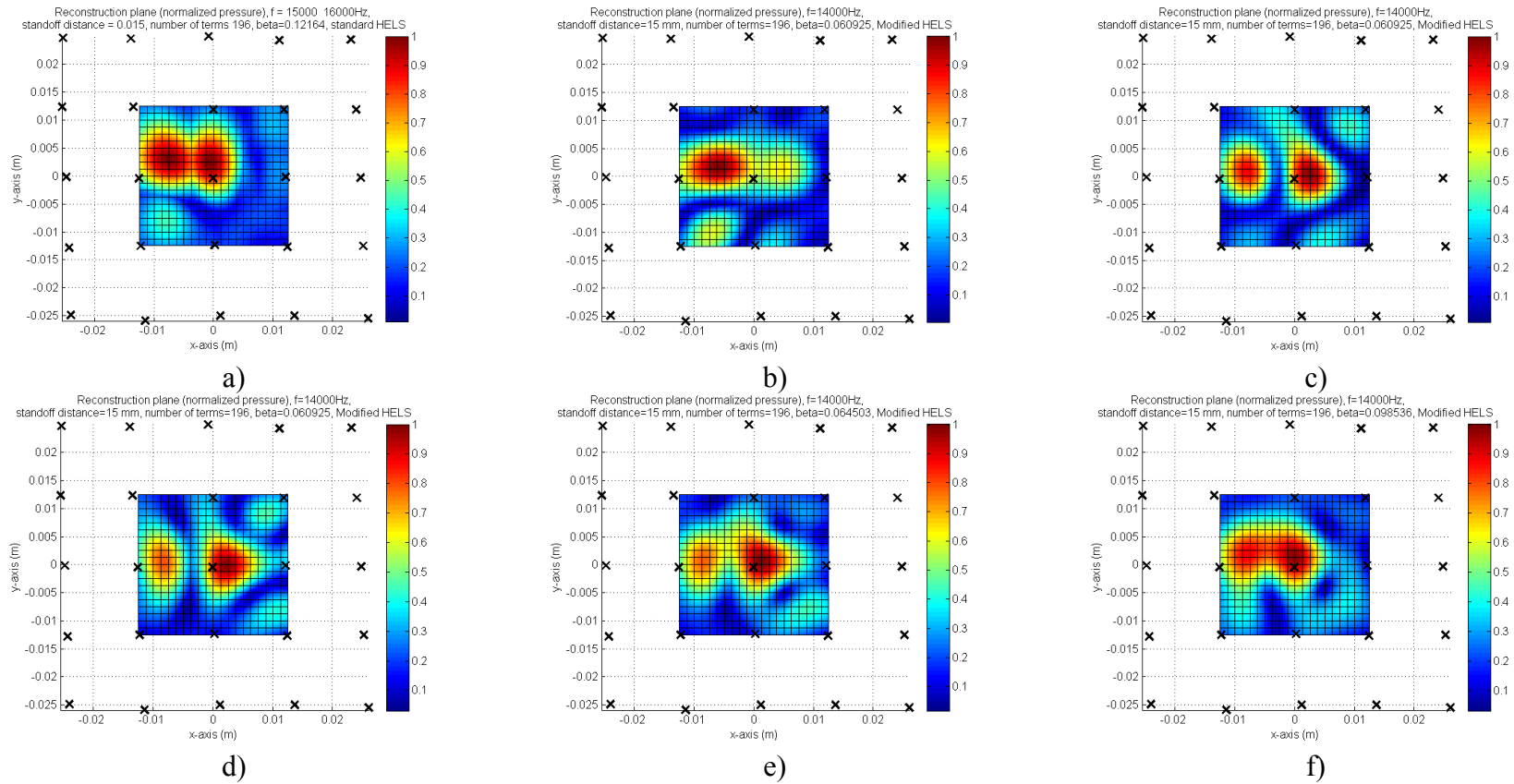


Figure 0.5: Reconstruction surfaces with $\delta=10$ mm, $d=15$ mm, $f=14$ kHz and varying phase angle at source location scenario 3 – a) reconstruction surface of incoherent sources (baseline); b) Modified HELS reconstruction surface with $\phi = 0$; c) Modified HELS reconstruction surface with $\phi = \frac{\pi}{4}$; d) Modified HELS reconstruction surface with $\phi = \frac{\pi}{2}$; e) Modified HELS reconstruction surface with $\phi = \frac{3\pi}{4}$; f) Modified HELS reconstruction surface with $\phi = \pi$

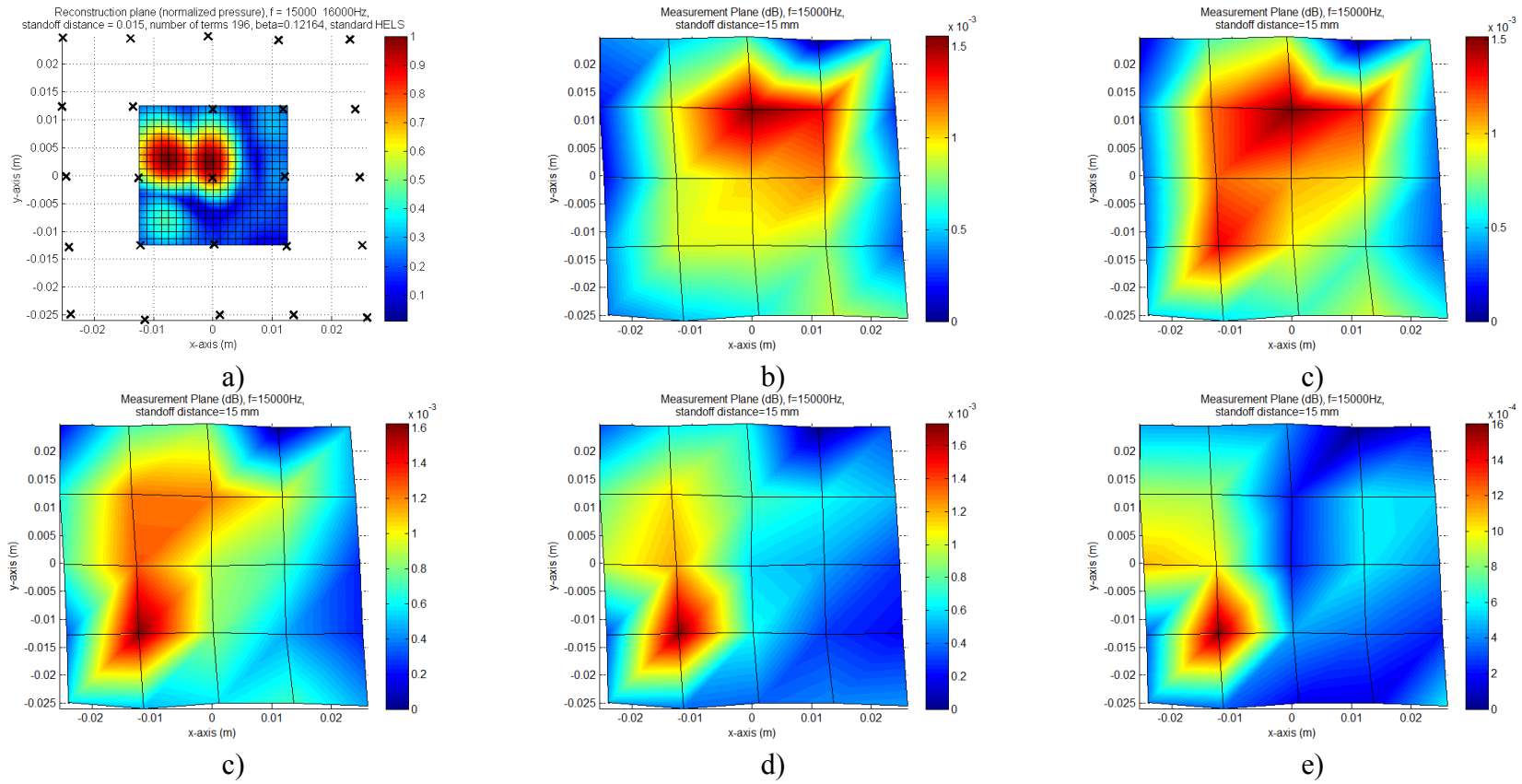


Figure 0.6: Measurement surfaces with $\delta=10$ mm, $d=15$ mm, $f=15$ kHz and varying phase angle at source location scenario 3 – a) reconstruction surface of incoherent sources (baseline); b) measurement surface with $\phi = 0$; c) measurement surface with $\phi = \frac{\pi}{4}$; d) measurement surface with $\phi = \frac{\pi}{2}$; e) measurement surface with $\phi = \frac{3\pi}{4}$; f) measurement surface with $\phi = \pi$

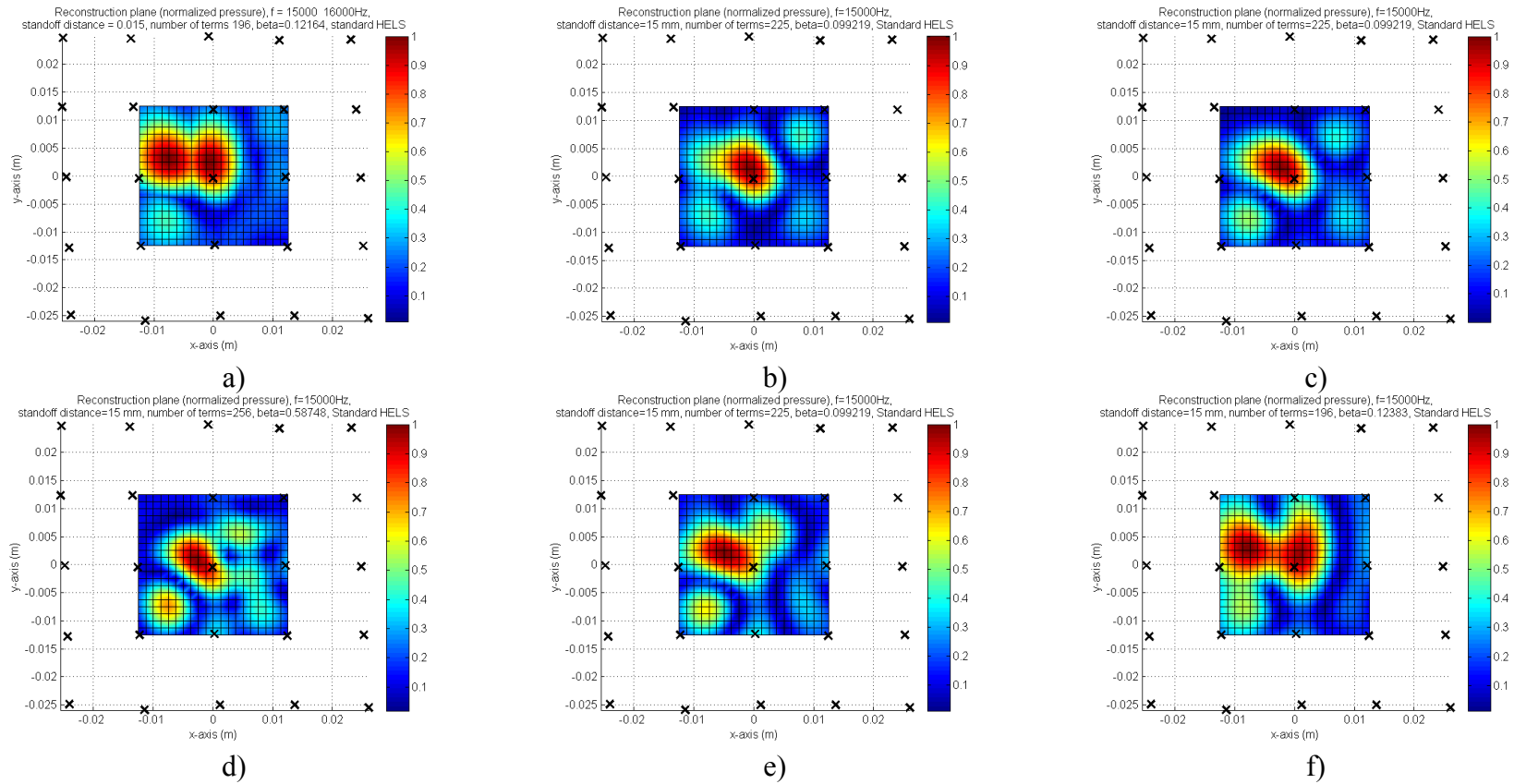


Figure 0.7: Reconstruction surfaces with $\delta=10$ mm, $d=15$ mm, $f=15$ kHz and varying phase angle at source location scenario 3 – a) reconstruction surface of incoherent sources (baseline); b) Standard HELS reconstruction surface with $\phi = 0$; c) Standard HELS reconstruction surface with $\phi = \frac{\pi}{4}$; d) Standard HELS reconstruction surface with $\phi = \frac{\pi}{2}$; e) Standard HELS reconstruction surface with $\phi = \frac{3\pi}{4}$; f) Standard HELS reconstruction surface with $\phi = \pi$

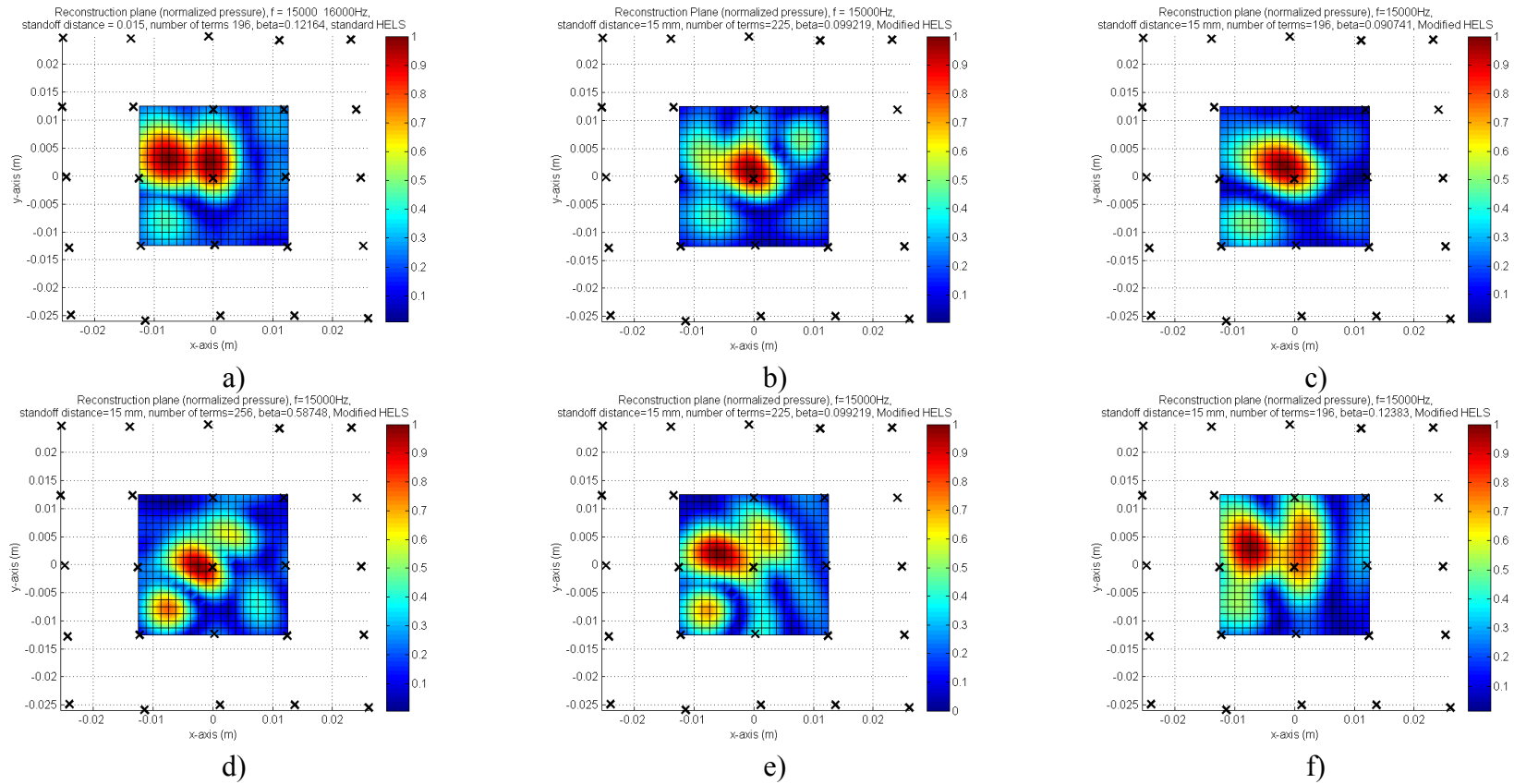


Figure 0.8: Reconstruction surfaces with $\delta=10$ mm, $d=15$ mm, $f=15$ kHz and varying phase angle at source location scenario 3 – a) reconstruction surface of incoherent sources (baseline); b) Modified HELS reconstruction surface with $\phi = 0$; c) Modified HELS reconstruction surface with $\phi = \frac{\pi}{4}$; d) Modified HELS reconstruction surface with $\phi = \frac{\pi}{2}$; e) Modified HELS reconstruction surface with $\phi = \frac{3\pi}{4}$; f) Modified HELS reconstruction surface with $\phi = \pi$

CHAPTER 6: CONCLUSIONS AND FUTURE WORK

The objective of the presented dissertation was to determine if HELS can provide better spatial resolution than NAH resolution guidelines in reconstruction of coherent point sources. HELS' ability to synthesize the entire acoustic field with less number of measurement points than other NAH methods is well documented. However, the extent of this advantage has not been applied to point-like sources in violation of the NAH resolution guidelines. Numerical simulations and experimental analysis were done to determine the feasibility of HELS violating these guidelines.

Numerical simulations were conducted with varying parameters using HELS and a new weighted variant termed, "Modified HELS". As a baseline, Fourier Acoustics was used during simulations. In simulations, we have shown that the NAH resolution guidelines provided by Williams are not applicable to coherent point sources. The concentrated energy of a point source causes the overall SNR of the surface to be much higher than the point-to-point SNR. Consequently, finer resolution reconstruction is feasible with coherent point sources. However, though both HELS and Fourier Acoustics provided better resolution than the NAH guidelines suggested, factors affecting reconstruction resolution of point sources were characterized.

Besides stand-off distance, the resolution capabilities of HELS and Fourier Acoustics were proven related to the relative phase angle, source separation and acoustic frequency. With decreasing frequency and relative phase angle, both methodologies showed reduced accuracy in reconstruction. The relationship was shown to be due to the effects of spherical spreading to the measurement plane. However, HELS and in particular Modified HELS, showed significant increases in accuracy relative to Fourier Acoustics. Increased accuracy was in spite of requiring

98% less measurement points than Fourier Acoustics (Fourier Acoustics –1681 measurement points, HELS – 25 measurement points).

Furthermore, refinement of the Fourier Acoustics measurement and reconstruction surfaces by increasing the number of measurement points proved unreliable due to an increase in discrete ill-posedness. On the other hand, the HELS methods were able to refine reconstruction resolution by a “zoom-in” approach, where a subset of the reconstruction surface was reconstructed with the same number of measurement and reconstruction points without added calculation or measurement cost. In the case of HELS, the problem does not see significant increase in ill-posedness since the measurements, and consequently, the singular values of the problem do not change.

Experimental validations of the simulations were done by approximating two point sources in a lab with a measurement system approximating the simulation model. Due to the difficulties in creating accurate phase angles in practice, phase angles were swept between 0 and π in an attempt to cover the range used in simulation. We show that when the measured pressures match the expected pressures for a given phase angle, experimental and simulation results correlate. Evidence was also provided showing Modified HELS’ ability to provide more accurate reconstruction locations as phase angle decreases. Testing with Fourier Acoustics was not done due to the number of measurements required to produce the same resolution of reconstruction as HELS.

Though HELS and Modified HELS show promise in fine resolution point source reconstruction, a number of areas remain open for future research:

- 1) Guidelines defining feasible point source reconstruction – guidelines defining feasible reconstruction based on phase angle, stand-off distance, source separation and frequency is required before general application of the methods can be implemented.
- 2) Justification for poor reconstruction at unexpected frequencies with $\delta=10$ mm, $d=15$ mm at $\phi = \frac{\pi}{2}$ – The predictability of why and when these scenarios occur is important prior to use in practical applications.
- 3) Mathematical justification for Modified HELS – Mathematical proof would help understand the limitations of the method. For example, is the intuitive restriction of only applying the method to point sources true? Also, can further resolution be gained in poor SNR environments by amplifying the weighting term by squaring or another method?
- 4) Define the relationship between the number of measurements taken and measurement resolution with the HELS methods – In Fourier Acoustics, measurement spacing is based on meeting the spatial Nyquist rate. However, the spatial Nyquist rate does not apply to HELS due to its ability to synthesize points. In the presented studies, adding one row and column of measurements at small stand-off distances significantly improved results. Would an increase in the number of measurement points increase reconstruction accuracy with HELS at farther stand-off distances, particularly at cases of $\phi=\frac{\pi}{2}$ or less? Assuming an increase in accuracy occurs, is there an optimum

number of measurement points before the level of discrete ill-posedness reduces reconstruction accuracy?

Our focus was to determine if HELS was capable of better reconstruction resolution of coherent point sources than traditional guidelines and methods. We found in almost all cases, that both HELS methods met or exceeded the baseline methodology in which the guidelines were based on. Though the above areas must be investigated before application of the method can be used in general applications, Standard and Modified HELS show promise in tackling current and future acoustic problems.

REFERENCES

1. Williams, E. G. and J. D. Maynard. "Holographic imaging without the wavelength resolution limit," *Phys. Rev. Lett.* 45, 554–557 (1980).
2. Williams, E. G. and J. D. Maynard. "Numerical evaluation of the Rayleigh integral for planar radiators using the FFT," *J. Acoust. Soc. Am.* 72, 2020–2030 (1982).
3. Maynard, J. D., E. G. Williams, and Y. Lee. "Nearfield acoustic holography: I. Theory of generalized holography and the development of NAH," *J. Acoust. Soc. Am.* 78, 1395–1413 (1985).
4. Bertero, M. and P. Boccacci. *Introduction to Inverse Problems in Imaging*. (IOP Publishing Ltd, Philadelphia, PA, 1998).
5. Williams, E.G. *Fourier Acoustics: Sound Radiation and Nearfield Acoustical Holography*. (San Diego, CA, Academic 1981).
6. Gardner, B.K. and R.J. Bernhard. "A noise source identification technique using an inverse Helmholtz integral equation method," *ASME J. Vib., Acoust., Stress, Reliab. Des.* 110, 84-90 (1988).
7. Meirovitch, L. *Principles and Techniques of Vibrations*. (Prentice-Hall Inc., Upper Saddle River, NJ, 1997).
8. Wu, S.F. "Methods for reconstructing acoustic quantities based on acoustic pressure measurements," *J. Acoust. Soc. Am.* 124 (5), 2680-2697 (2008).
9. Bruno, M., S. Magalhães, et al. "Sound sources reconstruction techniques: a review of their evolution and New Trends," *Acta Acustica United with Acustica*. Vol. 90, 190-220 (2003).

10. Wang, Z.X. and S. F. Wu. "Helmholtz equation least-squares method for reconstructing the acoustic pressure field." *Journal of the Acoustical Society of America* 102(4): 2020-2032 (1997).
11. Rayleigh, J. W. S. "On the passage of waves through apertures in plane screens, and allied problems", *Philosophical Magazine*, 43, pp. 259-272 (1897).
12. Pierce, A. *ACOUSTICS: An Introduction to its Physical Principles and Applications* (Acoustical Society of America, Woodbury, NY, 1994).
13. ISO 9614-2, Acoustics — Determination of sound power levels of noise sources using sound pressure — Precision methods for anechoic and hemi-anechoic rooms.
14. ISO 3745, Acoustics — Determination of sound power levels of noise sources using sound pressure — Precision methods for anechoic and hemi-anechoic rooms
15. Williams, E.G., J.D. Maynard, et al. "Sound source reconstruction using a microphone array," *J. Acoust. Soc. Am.* 68, 340-344 (1980).
16. Williams, E.G., H.D. Dardy, et al. "Nearfield acoustical holography using an underwater automated scanner," *J. Acoust. Soc. Am.* 78, 789-798 (1985).
17. Williams, E.G., H.D. Dardy, et al. "Generalized nearfield acoustical holography for cylindrical geometry: Theory and experiment," *J. Acoust. Am.* 81, 389-407 (1987).
18. Veronesi, W. A. and J.D. Maynard. "Nearfield acoustic holography (NAH): II. Holographic reconstruction algorithms and computer implementation," *J. Acoust. Am.* 81, 1288-1292 (1987).
19. Williams, E. G. "Supersonic acoustic intensity on planar sources." *The Journal of the Acoustical Society of America* 104(5): 2845-2850 (1998).

20. Williams, E.G., B. H. Houston, et al. "Broadband nearfield acoustical holography for vibrating cylinders." *The Journal of the Acoustical Society of America* 86(2): 674-679 (1989).
21. Williams, E.G., B. H. Houston, et al. "Fast Fourier Transform and singular value decomposition formulations for patch near-field acoustical holography." *Journal of the Acoustical Society of America* 114(3): 1322-1333 (2003).
22. Sarkissian, A. "Method of superposition applied to patch near-field," *J. Acoust. Am.* 115, 1593-1596 (2004).
23. Lee, M. and J. S. Bolton. "Patch near-field acoustical holography in cylindrical geometry," *J. Acoust. Soc. Am.* 118, 3721-3732 (2005).
24. Harris, F. J. "On the use of windows for harmonic analysis with the discrete Fourier transform." *Proceedings of the IEEE* 66(1): 51-83 (1978).
25. Sarkissian, A. "Extension of measurement surface in near-field acoustic holography," *J. Acoust. Am.* 115, 1593-1596 (2004).
26. Haberman, R., *Applied Partial Differential Equations* (Prentice-Hall, Upper Saddle River, NJ, 2004).
27. Kim, B.-K. and J.-G. Ih. "On the reconstruction of the vibro-acoustic field over the surface enclosing an interior space using the boundary element method." *The Journal of the Acoustical Society of America* 100(5): 3003-3016 (1996).
28. Veronesi, W. A. and J. D. Maynard, "Digital holographic reconstruction of sources with arbitrarily shaped surfaces." *J. Acoust. Am.* 85(2): 588-598 (1989).
29. Bronson, R., *Schaum's Outlines: Matrix Operations* (McGraw-Hill, New York, 1989).

30. Borgiotti, G.V., A. Sarkissian, et al. "Conformal generalized nearfield acoustic holography for axis symmetric geometries." *Journal of the Acoustical Society of America* 88(1): 199-209 (1990).
31. Kim, G.T. and B.-T. Lee. "3-D sound source reconstruction and field reproduction using the Helmholtz integral equation," *J. Sound Vib.* 136, 245–261 (1990).
32. Bai, M. R. "Application of BEM boundary element method based acoustic holography to radiation analysis of sound sources with arbitrarily shaped geometries," *J. Acoust. Soc. Am.* 92, 533–549 (1992).
33. Kim, Y. K. and Y.-H. Kim. "Holographic reconstruction of active sources and surface admittance in an enclosure," *J. Acoust. Soc. Am.* 105, 2377–2383 (1999).
34. Zhang, Z, N. Vlahopoulos, et al. "A computational acoustic field reconstruction process based on an indirect boundary element formulation," *J. Acoust. Soc. Am.* 108, 2167–2178 (2000).
35. Schuhmacher, A., J. Hald, K. B. Rasmussen, and P. C. Hansen. "Sound source reconstruction using boundary element calculations," *J. Acoust. Soc. Am.* 113, 114–127 (2004).
36. Saijyou, K. and H. Uchida. "Data extrapolation method for boundary element method-based near-field acoustical holography," *J. Acoust. Soc. Am.* 115, 785–796 (2004).
37. Valdivia, N. and E. G. Williams. "Implicit methods of solution to integral formulations in boundary element method based nearfield acoustic holography," *J. Acoust. Soc. Am.* 116, 1559–1573 (2004).

38. Langrenne, C., M. Melon, et al. "Boundary element method for the acoustic characterization of a machine in bounded noisy environment," J. Acoust. Soc. Am. 121, 2750–2757 (2007).
39. Rayess, N. and S.F. Wu. "Experimental validations of the HELS method for reconstructing acoustic radiation from a complex vibrating structure," J. Acoust. Am. 107(6): 2955-2964 (2000).
40. Rayess, N., S.F. Wu, et al. "Visualization of acoustic radiation from a vibrating bowling ball," J. Acoust. Am. 109(6): 2771-2779 (2001).
41. Lu, H.C. "Reconstruction of vibroacoustic responses using Helmholtz equation least squares method." ETD Collection for Wayne State University. Paper AAI3152338 (2004).
42. Lu, H.C. and S. F. Wu. "Reconstruction of vibroacoustic responses of a highly nonspherical structure using Helmholtz equation least-squares method." Journal of the Acoustical Society of America 125(3): 1538-1548 (2009).
43. Wu, S.F. and J. Yu. "Reconstructing interior acoustic pressure fields via Helmholtz equation least-squares." J. Acoust. Am., 104(4): 2054-2060 (1998).
44. Candes, E. "Compressed sensing makes every pixel count."
<http://www.ams.org/samplings/math-history/hap7-pixel.pdf>. n.d. Web. 12 Sep. 2010.
45. "Compressive Sensing Sources." *<http://dsp.rice.edu/cs>*. n.d. Web. 12 Sep. 2010.
46. Romberg, J. "Imaging via compressive sampling." IEEE Signal Processing Magazine 25(2): pp. 14-20 (2008).
47. Gilbert, A.C, S. Muthukrishnan, et al. "Improved Time Bounds for Near-Optimal Sparse Fourier Representation via Sampling". Proc. SPIE Wavelets XI. San Diego, CA (2005).

48. Ragheb, T., S. Korolos, et al. "Implementation Models for Analog-to-Information Conversion via Random Sampling". IEEE International Midwest Symposium on Circuits and Systems. Montreal, Canada (2007).
49. Davis, Tim. "Sparse Matrix." From MathWorld--A Wolfram Web Resource, created by Eric W. Weisstein. <http://mathworld.wolfram.com/SparseMatrix.html>.
50. Baraniuk, R. "An introduction to compressive sampling" IEEE Signal Processing Magazine 24(2): pp. 118-121 (2007).
51. Candes, E. J., J. Romberg, et al. "Robust uncertainty principles: exact signal reconstruction from highly incomplete frequency information." Information Theory, IEEE Transactions on 52(2): 489-509 (2006).
52. Tao, T. "Compressed sensing: Robust recovery of sparse signals from limited measurements." <http://www.youtube.com/watch?v=i2aY7tZ5S7U>. 19 Dec. 2008. Web. 12 Sep. 2010.
53. Beranek, L. *Acoustical Measurements*. (American Institute of Physics, College Park, Maryland, 1998).
54. Zayed, A. I. *Advances in Shannon's Sampling Theory*. (CRC Press., Ann Arbor, MI, 1993).
55. "Model 130E21 specification sheet" <http://www.pcb.com>. n.d.. Web. 25 Mar. 2010.
56. Yoon, S.H. and P. A. Nelson. "Spatial resolution limits for the reconstruction of acoustic source strength by inverse methods." Journal of Sound and Vibration 265(3): 583-608 (2003).

57. Nelson, P. A. and S. H. Yoon. "Estimation of acoustic source strength by inverse methods: Part I, conditioning of the inverse problem." *Journal of Sound and Vibration* 233(4): 643-668 (2000).
58. Meecham, W.C. "Variational Method for the Calculation of the Distribution of Energy Reflected from a Periodic Surface. I." *Journal of Applied Physics* 27(4): 361-367 (1956).
59. Isakov, V. and S. F. Wu. "On theory and application of the Helmholtz equation least squares method in inverse acoustics." *Inverse Problems* 18(4): 1147-1159 (2002).
60. Semenova, T. and S. F. Wu. "The Helmholtz equation least-squares method and Rayleigh hypothesis in near-field acoustical holography." *J. Acoust. Am.* 115(4): 1632-1640 (2004).
61. Wu, S. "On reconstruction of acoustic pressure fields using the Helmholtz equation least squares method." *Journal of the Acoustical Society of America* 107(5): 2511-2522 (2000).
62. Borgiotti, G. V., A. Sarkissian, et al. "Conformal generalized nearfield acoustic holography for axis symmetric geometries." *Journal of the Acoustical Society of America* 88(1): 199-209 (1990).
63. Dziklinski, R. and S.F. Wu. "Spatial resolution of Helmholtz equation least-squares-based nearfield acoustical holography " *The Journal of the Acoustical Society of America* 121 (5): p. 3070 (2007).
64. Williams, E.G. "Regularization methods for near-field acoustical holography." *The Journal of the Acoustical Society of America* 110(4): 1976-1988 (2001).
65. Semenova, T. "On the behavior of the Helmholtz equation least-squares method solutions for acoustic radiation and reconstruction." ETD Collection for Wayne State University. Paper AAI3152338 (2004).

66. Hansen, P. C. *Rank-Deficient and Discrete Ill-Posed Problems*. (SIAM, Philadelphia, PA, 1998).
67. Hagerdon, P. and Anirvan DasGupta. *Vibrations and Waves in Continuous Mechanical Systems*. (John Wiley and Sons Ltd. West Sussex, England, 2007).
68. Golub, G.H., M. T. Heath and G. Wahba. "Generalized cross-validation as a method for choosing a good ridge parameter." *Technometrics* (21) 215-223 (1979).
69. "High Pressure 156 Lee Chek product data sheet"
<http://www.theleeco.com/LEEweb2.nsf/PDS%2077.pdf>. n.d.. Web. 25 Mar. 2010.
70. "Refrigerator Compressor Relay Switch - WR07X10051"
<http://www.bizrate.com/refrigerator-compressor-relay/>. n.d.. Web. 25 Mar. 2010.
71. Weinreich, G. and E. B. Arnold. "Method for measuring acoustic radiation fields." *The Journal of the Acoustical Society of America* 68(2): 404-411 (1980).
72. Matsumoto, M. and Nishimura, T. "Mersenne Twister: A 623-Dimensionally Equidistributed Uniform Pseudorandom Number Generator," *ACM Transactions on Modeling and Computer Simulation*,(1998), 8(1):3-30.
73. Wu, S. F. "Hybrid near-field acoustic holography." *Journal of the Acoustical Society of America* 115(1): 207-217 (2004).
74. Hansen, P. C. "Regularization tools: a matlab package for analysis and solution of discrete ill-posed problems.." <http://www.netlib.org/numeralgo/na4> n.d. Web. 14 Mar. 2010.
75. Wahba, G. and Y. Wang. "Behavior near zero of the distribution of GCV smoothing parameter estimates." *Statistics & Probability Letters* 25(2): 105-111 (1995).

ABSTRACT**RECONSTRUCTION RESOLUTION OF COHERENT POINT SOURCES WITH
HELMHOLTZ EQUATION LEAST SQUARES**

by

RICHARD E. DZIKLINSKI III**MAY 2011****Advisor:** Dr. Sean F. Wu**Major:** Mechanical Engineering**Degree:** Doctor of Philosophy

The dissertation investigates the reconstruction of coherent point sources using Helmholtz Equation Least Squares (HELs) method based on measurements in violation of Nearfield Acoustical Holography (NAH) resolution guidelines. In HELs, the Helmholtz equation is solved by matching a series of localized spherical expansion functions to the measured pressures in the field. Expansion coefficients are solved for by least squares and used to reconstruct pressures at the source surface. By approximating the pressure radiation with expansion functions, field and surface pressures can be synthesized, resulting in the possibility of higher spatial resolution than previous generation NAH methods such as Fourier Acoustics and Inverse Boundary Element Methods. The NAH guidelines dictate that spatial resolution decreases with increasing stand-off distance and decreasing Signal to Noise Ratio (SNR). Also, in methods other than HELs, measurement spacing must exceed the spacing derived from the Nyquist rate to mitigate the risk of aliasing. HELs is not limited by the Nyquist rate due to its ability to synthesize field and surface points.

The resolution capability of HELS is tested through numerical simulation and experimental testing. Besides HELS, a weighted variant of HELS, termed “Modified HELS” is tested. For comparison, Fourier Acoustics is used as a baseline with measurement spacing equal to and finer than the measurement spacing used in the HELS simulations. Results show that both HELS and Fourier Acoustics reconstruct point sources at finer resolution than the NAH guidelines predict. The increased resolution is likely due to the use of point sources and its affect on the definition of SNR and the angular spectrum. However, HELS, and in particular Modified HELS, show a significant increase in accuracy in comparison to Fourier Acoustics for the parameters tested.

The main conclusion of this dissertation is that Standard and Modified HELS are better tools than traditional NAH methods when reconstructing coherent point sources in violation of the NAH spatial resolution guidelines.

AUTOBIOGRAPHICAL STATEMENT**RICHARD E. DZIKLINSKI III****EDUCATION**

Ph.D., Mechanical Engineering, Wayne State University, 2010
M.S., Mechanical Engineering, Wayne State University, 2004
B.S., Mechanical Engineering, Wayne State University, 2002

AFFILIATIONS

Member, Acoustical Society of America (ASA)

PROFFESIONAL CARREER

Product development engineer, TRW Automotive, 2000-present

PUBLICATIONS IN PROCESS

Richard Dziklinski and Sean F. Wu, "*Simulation of Reconstruction of coherent point sources in violation of NAH spatial resolution guidelines*"

Richard Dziklinski and Sean F. Wu, "*Experimental Validation of Reconstruction of coherent point sources in violation of NAH spatial resolution guidelines*"

CONFERENCE AWARDS

Second place in the Best Student Paper Award for the paper "Spatial resolution of Helmholtz, equation least squares based nearfield acoustical holography," by Richard E. Dziklinski III and Sean F. Wu, presented at the 153rd ASA meeting, May 2007

CONFERENCE PRESENTATIONS

Dziklinski III, R. E. and S. F. Wu "Spatial resolution of Helmholtz, equation least squares based nearfield acoustical holography." by Richard E. Dziklinski III and Sean F. Wu, presented at the 153rd ASA meeting, May 2007

Dziklinski III, R. E. and S. F. Wu "The Nyquist spatial sampling requirement in nearfield acoustical holography." by Richard E. Dziklinski III and Sean F. Wu, presented at the 158th ASA meeting, October 2009

Dziklinski III, R. E. and S. F. Wu "Experimental validation of Helmholtz equation least squares when the Nyquist spatial sampling requirement is violated." by Richard E. Dziklinski III and Sean F. Wu, presented at the 159th ASA meeting, March 2010